Elucidating the Role of Syntaxin-1A in Cardiac Excitation-Contraction Coupling and Hypertrophic Remodeling in the Adult Mouse Heart

Fahad Anser

A THESIS SUBMITTED TO
THE FACULTY OF GRADUATE STUDIES
IN PARTIAL FULFILLMENT OF THE REQUIREMENTS
FOR THE DEGREE OF
MASTER OF SCIENCE

GRADUATE PROGRAM IN BIOLOGY
YORK UNIVERSITY
TORONTO, ONTARIO

DECEMBER 2023

ABSTRACT

Syntaxin-1A (STX1A) is a member of the SNARE family which is recognized for its role in membrane exocytosis and ion-channel regulation. Although the physiological properties of STX1A has been assessed in many tissues, its role within the heart remains unelucidated. To address this, a cardiomyocyte specific STX1A knockout (KO) model was generated in adult C57BL/6J mice. Through utilization of both *in vivo* and *in vitro* approaches, STX1A haploinsufficiency was demonstrated to induce transient contractile dysfunction, a global electromechanical delay, and reduction in Ca^{2+} handling gene expression. The depressed cardiac function was supported by volumetric overload of the left-ventricle and cardiomyocyte/sarcomeric restructuring. Furthermore, pathological hypertrophy was observed as evident by the re-expression of fetal genes and left-ventricular fibrosis. Collectively, the results suggest an important role of STX1A in cardiac E-C coupling, whereby its KO impairs the heart's electromechanical function and induces ventricular remodelling to compensate for the elevated hemodynamic volume overload.

ACKNOWLEDGEMENTS

The last two years have been some of the greatest developmental years of my life. Exiting this chapter knowing that I have become a stronger and more independent individual leaves me with great gratitude and appreciation for such an opportunity. Thank you, Dr. Tsushima, for taking me on with such open arms since the first day – from BIOL 4200, to volunteering in your lab, and now having completed an entire thesis, your relentless support and encouragement is what has allowed me to excel both as a researcher and as a person. Thank you for believing in me and always lifting me up whenever I may have doubted myself Bobby!

I would also like to thank my co-supervisor Dr. Sweeney who has provided me great guidance throughout my Master's. If it weren't for our progress meetings, I would still be tweaking the Langendorff-perfusion system! Your advice and kind words have always benefited me and allowed me to think critically in every aspect of my project, and I will be forever grateful for that. Equally, I would like to than Dr. Paluzzi who has been of such sincere help ever since the beginning of my Masters study. With every conversation we had, I left learning more about my project than before. You kindly lent a helping hand throughout this process – whether it be with primer design/optimization or allowing me to use your qPCR machine 20 times a week – and made me feel like one of your lab. As such, I would also like to extend a further thank you to Marishia, Jinghan, Thomas, Zainab, and Brittany for creating such a warm and welcoming environment throughout the past two years – y'all rock!

To my family, your continued patience, guidance, love, and generosity throughout this process has meant the world to me. Mom and dad, your relentless support in my Masters journey to always prioritize my education before any other objective is what has allowed me to attain this degree, and I owe this achievement to you. Likewise, Talha, Waleed and Bilal, you brothers have been the greatest support system I could ever ask for. You have allowed me to rant, celebrate my achievements, discuss pitfalls while showing nothing but support and it is something I will cherish and remember forever. As engineers, even though you probably never understood a thing I said, you continuously showed me the same level of care and concern while giving me great life advice, and I thank you for being such supportive and encouraging siblings.

Dr. Farwa Sajadi and Dr. Nazar Polidovitch! I don't know where to start with you guys… Farwa, I have always said this but when it's all said and done, York better have a statue of you!! I have yet to meet someone as selfless and caring, and I sincerely thank you for being such an exceptional friend, support system, and role model throughout this journey. From the first day where I missed my class, to helping me practice for my defence, you have been there for every part of the journey, and I can never repay you for all your kindness (and sushi lol). Nizar, you always took time even if it was 5 minutes of your day to check-in on me and I am so grateful for you. As I always said, you have a heart of gold and I can't wait to see you become a successful doctor soon! A further thank you to Ryan, Parashar, Muhammad, and Rob who continuously provided excellent guidance – I hope nothing the best for you guys and your future!

Despite of all the moments of doubt, all those moments where you questioned your journey, your personal and mental ups and downs, you prevailed and made it… so lastly, I want to thank myself. Look back at what you overcame and be proud of this for no one but yourself :)!

TABLE OF CONTENTS

List of Tables

List of Figures

List of Abbreviations

ActB – beta-actin

α-MHC – alpha-myosin heavy chain

ANP – atrial natriuretic peptide

AP – action potential

ATP – adenosine triphosphate

β-MHC – beta-myosin heavy chain

BNP – brain natriuretic peptide

bp – base pair

BSA – bovine serum albumin

CaMKII – Ca^{2+}/calmodulin kinase-II

Cav1.2 – cardiac L-type calcium channel

cDNA – complementary DNA

cGMP – cyclic guanosine monophosphate

CICR – calcium-induced calcium release

CO – cardiac output

Cre – cyclic recombinase

CREB – cyclic-adenosine monophosphate response binding element

CSA – cross-sectional area

Cx43 – connexin-43

DAPI - 4′,6-diamidino-2-phenylindole

DCM – dilated cardiomyopathy

dP/dT – rate of pressure change

EC – excitation-contraction

EDTA - Ethylenediaminetetraacetic acid

EF – ejection fraction

FS – fractional shortening

GAPDH – glyceraldehyde 3-phosphatase dehydrogenase

HR – heart rate

kDa – kilo Dalton

KO – knockout

K_v – voltage-gated potassium channels

Kv4.2 – transient outward potassium channel

LA – left atria

LVEDs/LVEDd – left ventricular end systolic dimension/diastolic dimension

LTCC – L-type calcium channels

LV – left ventricle

LVEVs/LVEVd – left ventricular end systolic volume/diastolic volume

MAPK – mitogen-activated protein kinases

Mer – modified estrogen receptor

Munc-18 – mammalian uncoordinated-18

Na_v – voltage-gated sodium channels

NCX – sodium/calcium exchanger

NFAT – nuclear factor of activated T-cells

NPR – natriuretic peptide receptor

PBS – phosphate buffered saline

PFA – paraformaldehyde

PKG – cGMP-dependent protein kinase

Pk% - peak-radial strain percentage

Plb – phospholamban

RT-qPCR – reverse transcriptase quantitative-polymerase chain reaction

RyR – ryanodine receptor

SERCA – sarcoplasmic/endoplasmic reticulum calcium ATPase

SNAP – synaptosomal associated protein

SNARE – soluble N-ethylmaleimide-sensitive factor activating protein receptor

Sp1 – specificity protein 1

STX1A – syntaxin-1A

SV – stroke volume

TH – thyroid hormone

TPk – time-to-peak

TRE – thyroid response element

t-SNARE – target SNARE

VAMP – vesicle-associated membrane protein

VGCC – voltage-gated calcium channel

v-SNARE – vesicle SNARE

WGA – wheat-germ agglutinin

CHAPTER 1: INTRODUCTION

1.1 The Cardiovascular System

1.1.1 Background – The Cardiovascular System

The field of cardiovascular physiology has demonstrated immense interest over the past 3500 years, with studies of heart disease dating back to times of Egyptians and pharaohs (Hajar, 2017). Albeit major advancements have been made since, cardiovascular disease continues to prevail as the leading cause of death amongst both men and women (Roger et al., 2010). As reported by Tsao et al. (2022), approximately 19 million deaths were attributed to cardiovascular disease in 2020, amounting to an 18.7% increase from 2010. Moreover, since cardiovascular disease is not linked to one specific trigger (i.e., poor nutrition, tobacco use, genetics, diabetes, improper sleep, etc.), millions of lives are impacted yearly on a global scale (Tsao et al., 2022). Therefore, it is imperative to better understand the underlying mechanism of cardiovascular disease and heart failure in attempts to further pharmaceutical advancements against such a wide-spread disease which has no set cure to-date.

The cardiovascular system is critical amongst all organisms – from mammalians to some invertebrates – in ensuring continuous supply of blood and nutrient exchange throughout the body (Aird, 2011). Central to the mammalian cardiovascular system lies the four-chambered heart, divided into two atria and two ventricles which contract and relax in a bi-phasic manner. As demonstrated by William Harvey in his closed-loop system, the left and right sides of the heart carry opposing roles, with the right ventricle ejecting deoxygenated blood into the lungs for oxygenation, while the left ventricle ejects oxygenated blood into the rest of the body (Aird, 2011). Furthermore, the heart's unique physiological property to mediate blood circulation is accounted for *via* the cardiac tissue, comprised of cardiomyocytes (heart cells) which intercalate

together and contract in a fluid, pump-like manner (Sano et al., 1959). By functioning as a *syncytium*, cardiomyocytes are able to convert intrinsic electric stimuli to global contractile responses, thereby making the mechanism of the heart myogenic.

The coupling of electrical signalling to the mechanical contraction of the intact muscle dates to the work by Hill (1949), whereby electrical stimulation of an isolated soleus muscle generated a contractile response to the center in only 40 milliseconds. Sandow (1952) proposed an explanation for the observation, suggesting electrical stimuli may only be required to serve as an initial trigger and not throughout the course of the contraction. The hypothesis was supported by incubating the sartorius muscle in a sodium-free and potassium-deficient media, producing a decline in action potential (AP) strength with a linear increase in twitch tension (Sandow, 1952). Coupling with the results, Ringer's (1883) studies previously demonstrated the importance of calcium (Ca^{2+}) in mediating contraction, as coupling an induction shock with simultaneous addition of calcium to an isolated heart resulted in spontaneous return in contractility. Collectively, the findings allowed for the proposition of the concept of "excitation-contraction (E-C) coupling", highlighting the importance of an electrical stimulus in inducing mechanical contraction of the muscle when coupled with Ca^{2+}.

1.1.2 The Cardiac Conduction Pathway

As we know it today, the mechanism of electrical signal propagation – the "excitatory" role in E-C coupling – differs significantly between skeletal and cardiac muscle. Unlike skeletal muscle which relies on electrical stimulation *via* motor neurons at the neuromuscular junction, the myogenic nature of the heart allows for generation of intrinsic electric signals that are coupled to a mechanical response (Rich and Langer, 1975). Moreover, the autorhythmicity is

maintained through the cardiac conduction pathway, responsible for mediating AP propagation across the myocardium and eliciting coordinated contractions of the atrial and ventricular chambers; respectively (Aranega et al., 2012).

The cardiac conduction pathway functions through the activity of specialized ion-channels localized at different regions of the heart, responsible for delivering intracellular depolarizing signals which mediate cardiomyocyte contraction. Initiation of the pathway takes place at the border of the right atria and superior vena cava within a specialized region known as the "sinoatrial node" (also referred to as the pacemaker of the heart), where depolarizing currents through hyperpolarization-activated nucleotide-gated (HCN) channels raise the membrane potential above resting conditions (Christofells and Moorman, 2011). Since the heart is connected as a functional syncytium, the wave of depolarization generated at the pacemaker propagates towards the atrioventricular (AV) node *via* gap junctions, where signals are delayed ensuring complete contraction of the atria. From the AV node, electrical impulses travel through the septum of the heart prior to splitting into left and right bundle of His branches, and further into Purkinje fibers which innervate the entire ventricular endocardium and epicardium; respectively (Christoffels and Moorman, 2009).

In the ventricles, three primary channels modulate the rhythmicity of the heart: voltage-gated Na^+ (Na_v) channels, voltage-gated K^+ (K_v) channels, and voltage-gated Ca^{2+} (Ca_v) channels. Within resting states of the ventricle, the membrane potential is maintained at -90mV due to continuous efflux of K^+ ions *via* the inwardly-rectifying K^+ (K_{ir}) channels (Park and Fishman, 2011). Upon arrival of a depolarizing signal however, K_{ir} channels transition into a closed state, preventing outward efflux which thereby raises the membrane potential to -70 mV. A gradual rise in membrane potential triggers further opening of fast-acting Na_v channels,

depolarizing the cellular membrane prior to undergoing rapid inactivation (Park and Fishman, 2011). Upon generating a strong upstroke phase of the AP, the depolarizing signals travel down deep invaginations in cardiomyocytes known as transverse-tubules (T-tubules), where they cause activation of membrane-bound Ca_v channels which begins to couple the excitatory signal to the contractile response (Park and Fishman, 2011).

1.1.3 Cardiac Excitation-Contraction Coupling: Contraction

The discovery of the sarcomere – structural unit of a myofibril – was pivotal in today's understanding of cardiac E-C coupling. Through utilization of electron microscopy (EM), it was revealed that striated muscles are comprised of thick myosin filaments (A-bands) surrounded by thin actin filaments (I-bands), and electrical stimulation at the I-band was imperative in transducing an internal contractile response (Ruska and Kroll, 1931). Structural analysis of the I-band further revealed the presence of deep invaginations in cardiomyocytes known as T-tubules, which began externally and penetrated towards the cell's core (Draper and Hodge, 1949). Coupling with the initial proposition by Sandow (1952), it was suggested that T-tubules may partake a role in converting sub-surface level electrical stimuli into contractile responses at the center of the myocardium, hence coupling the excitation-contraction process.

T-tubules are long, hollow invaginations formed from the same phospholipid bilayer as the sarcolemma and are expressed within both skeletal and cardiac muscle (Hong and Shaw, 2017). By running perpendicular and parallel to the sarcomere, T-tubules carry two primary roles in the E-C coupling process: (1) allow for rapid AP propagation to the center of the cardiomyocytes, and (2) utilize the AP waveform to activate T-tubular studded "long-lasting" voltage-gated Ca^{2+} channels (L-type Ca^{2+} channels; LTCCs). Within the heart, the major LTCC

isoform expressed is $Ca_v1.2$, comprised of the primary α_1 pore-forming subunit alongside four auxiliary subunits which regulate the channel's function (Ahlijanian et al., 1990). Upon their activation, a small yet steady influx of Ca^{2+} raises the intracellular concentration which further activates specialized Ca^{2+}-release channels known as ryanodine receptors (RyR2). RyR2s are homotetrameric structures localized on the sarcoplasmic reticulum (SR), responsible for mediating large-scale increase in cytosolic Ca^{2+} levels to induce contraction. There are approximately 10,000 RyR2 clusters expressed within a single cardiomyocyte, with each cluster containing ~100 receptors (Cheng and Lederer, 2008). Due to their close proximity to the T-tubule, activation of a single $Ca_v1.2$ channel results in stimulation of four to six RyR2s, triggering SR Ca^{2+} release hence raising cytosolic Ca^{2+} levels from 50-100 nM to ~1 mM in the respective event termed "Ca^{2+}-induced-Ca^{2+}-release" (CICR) (Friel, 2004; Issa et al., 2012).

The global rise in free-intracellular Ca^{2+} *via* CICR is pivotal in inducing contractions of the heart and is mediated by the troponin-tropomyosin complex. The troponin-tropomyosin complex is composed of four polypeptides – tropomyosin, Troponin C (TnC), Troponin I (TnI), and Troponin T (TnT) – which interact with the actin-myosin filaments to regulate contractions of the myocardium. In a state of lower cytosolic Ca^{2+} (during relaxation of the heart), the double-stranded α-helical structure of tropomyosin lays along the actin filaments and sterically blocks myosin from binding (Moss, Razumova and Fitzsimons, 2004). Consequently, myosin ATPase is unable to hydrolyze adenosine triphosphate (ATP) and undergo cross-bridge cycling, thereby keeping the muscle in a relaxed state. In states of higher cytosolic Ca^{2+} load such as that during CICR, Ca^{2+} binds to TnC alleviating tropomyosin's interaction with the myosin-binding sites on actin, thereby allowing myosin ATPase to bind, hydrolyze ATP and pull the actin filament towards the center of the sarcomere (Moss, Razumova and Fitzsimons, 2004).

1.1.4 Cardiac Excitation-Contraction Coupling: Relaxation

At the end of systole or contraction, intracellular Ca^{2+} levels need to be reduced in the cytosol to initiate relaxation of the heart. The primary mechanism of lowering cytosolic Ca^{2+} levels is *via* the sarcoplasmic/endoplasmic reticulum Ca^{2+} ATPase (SERCA) pump, which demonstrates a dual function in cardiomyocytes: (1) reuptakes Ca^{2+} into the SR to lower free-Ca^{2+} levels, and (2) restores SR Ca^{2+} stores for the subsequent contraction cycle (Periasamy and Kalyanasundaram, 2007). In the process, the heart SERCA isoform, SERCA2a hydrolyzes a single ATP molecule to transport 2 Ca^{2+} ions against their concentration gradient into the SR. Since SERCA2a regulates Ca^{2+}-reuptake during relaxation, it is equally important to ensure its inhibition during contraction. Within its unphosphorylated form, phospholamban (Plb) functions as an allosteric inhibitor of SERCA2a by linking to SERCA2a and decreasing Ca^{2+} affinity at its two binding sites (Akin et al., 2013). During contraction or upon β-adrenergic stimulation, phosphorylation of Plb at serine-16 or Ca^{2+} binding alleviates its inhibition against SERCA2a, thereby re-establishing Ca^{2+} flux into the SR (Gustavsson et al., 2013).

Although SERCA2a functions as the primary mediator in reducing cytosolic Ca^{2+} levels (75% in humans and 90% in rodents), the sarcolemmal Na^+/Ca^{2+} Exchanger (NCX) also demonstrates a vital role in extruding Ca^{2+} from the cells (25% in humans and 10% in rodents) (Lipskaia et. al, 2011). Through utilization of the Na^+ gradient, NCX functions within a "forward" or "reverse mode" to dictate the flow of ions and thereby transportation of Ca^{2+}. During the resting membrane potential (or relaxation), NCX utilizes the extracellular gradient to transport 3 Na^+ ions into the cytosol in exchange for 1 Ca^{2+} ion (Bers, 2002). As a result, the intracellular Ca^{2+} levels decrease during relaxation of the myocardium, while Na^+ flux depolarizes the membrane for the subsequent cardiac cycle. Once the membrane is depolarized,

NCX operates in the reverse mode to bring 1 Ca^{2+} ion into the cell in extrusion for 3 Na^{+} ions, thereby increasing cytosolic Ca^{2+} levels for contraction (Bers, 2002). Collectively, NCX can operate to regulate both cytosolic Ca^{2+} levels and electrical repolarization of the myocardium, and abnormalities of the exchanger has been linked to cardiac arrhythmias, ischemia, and heart failure (Pott, Eckardt and Goldhaber, 2011). Therefore, tight regulation of NCX and all respective components of E-C coupling are imperative in preventing imbalances in intracellular Ca^{2+} handling, particularly LTCCs since they serve as the key mediator to the E-C process.

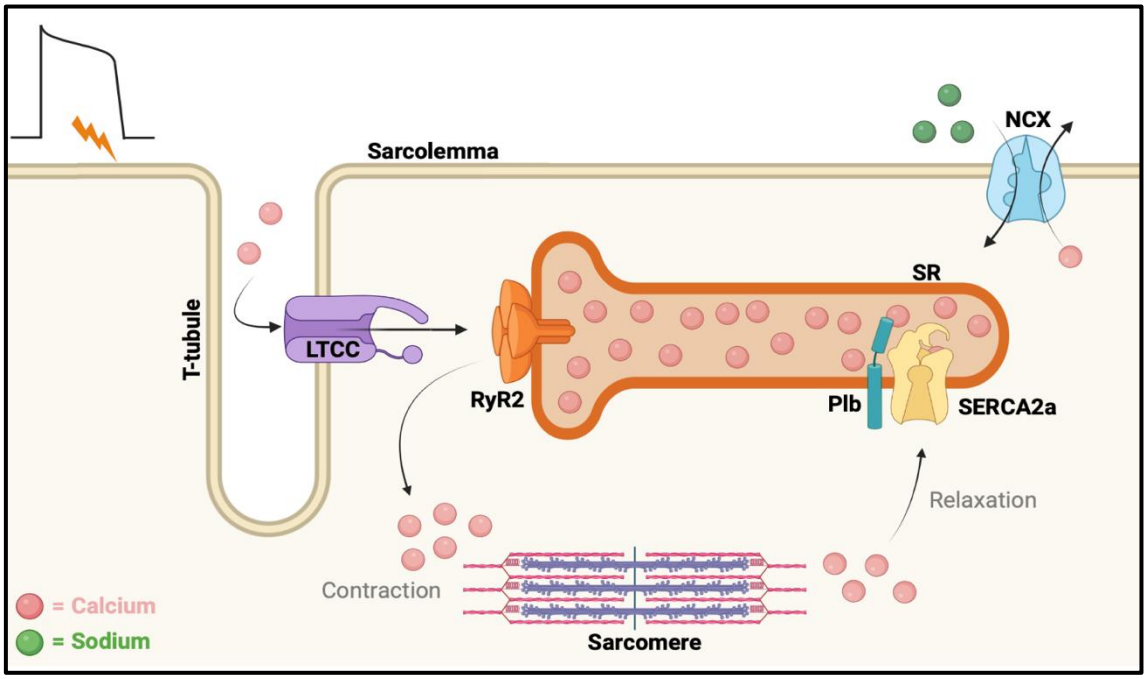

Figure 1: Excitation-contraction coupling in ventricular myocytes. Upon arrival of an electrical stimulus at the t-tubules, voltage-gated Ca^{2+} channels become activated and elicit an inward Ca^{2+} current which further activates SR localized RyRs. Opening of RyRs causes large-scale increase in cytosolic Ca^{2+} levels which interacts with the troponin-tropomyosin complex to induce contractions of the myocardium. During contraction, Plb tightly interacts with SERCA2a and inhibits its reuptake activity, while relaxation is mediated by loss of Plb-mediated inhibition of SERCA2a. A fraction of the free-cytosolic Ca^{2+} levels are also exchanged for three Na^{+} ions *via* the NCX. *LTCCs = L-type Ca^{2+} channels; RyRs = ryanodine receptors; Plb = phospholamban; SERCA2a = sarcoplasmic/endoplasmic reticulum Ca^{2+} ATPase; NCX = Na^{+}/Ca^{2+} exchanger.* Illustration was created on www.biorender.com.

1.1.5 LTCC Regulation as the Primary Mediator of Excitation-Contraction Coupling

The process of excitation-contraction coupling needs to be tightly regulated to ensure maintenance and handling of Ca^{2+} stores during CICR with each cardiac cycle. Since $Ca_v1.2$ serves as the voltage sensor and thereby trigger for SR-mediated Ca^{2+} release in myocytes, regulation of $Ca_v1.2$ becomes imperative when assessing and targeting numerous diseases such as ventricular hypertrophy, delayed after depolarizations, and arrhythmogenic heart failure (Chen et al., 2002; Goonasekara et al., 2011).

$Ca_v1.2$ is a multimeric protein, comprised of the primary α_1 pore-forming subunit, the α_2 and δ-subunits which collectively modulate α_1-surface-level expression, the β-subunit which mediates α_1-gating properties, and the γ-subunit shown to stabilize the α_1-subunit in the hydrophobic bilayer (Ahlijanian et al., 1990). Currents generated across the α_1-subunit of $Ca_v1.2$ (or any ion-channel localized on a multi-channel membrane) can thereby be demonstrated *via* the formula for macroscopic currents (*I*):

$$\boldsymbol{I = i * N * Po}$$

where *i* represents the single-channel current, *N* the number of channels expressed on the plasma membrane, and *Po* the open probability of the channel (Alvarez, Gonzalez and Latorre, 2002). Modulation of $Ca_v1.2$ currents can thereby occur through both primary and auxiliary subunits, such as the common pathway of α_1-subunit phosphorylation *via* $G_{\alpha s}$-signalling pathway. Through overactive sympathetic stimulation of the heart as recorded during the "fight-or-flight" response, or during heart failure (to compensate for abnormal responsiveness of the parasympathetic system), increased phosphorylation of the α_1-subunit allows for prolonged P_o, resulting in improved inward Ca^{2+} current and thereby CICR (Zhang and Anderson, 2018). The surface-level expression (*N*) of $Ca_v1.2$ channels can also be modulated through junctophilins – conserved

family of membrane tethering proteins – demonstrated to have a positive correlation between overexpression of junctophilin 2 (JPH2) and increased number of $Ca_v1.2$ channels embedded in the T-tubular membrane (Poulet et al., 2020). Though such mechanisms can regulate $Ca_v1.2$ macroscopic currents, chronic activation of G_s-signalling pathways for instance has been linked to cardiac hypertrophy, ventricular fibrosis, and even heart failure (Salazar, Chen, and Rockman, 2007). Even through utilization of catecholamine treatment in transgenic mice with G_s overexpression, an initial improvement in contractile function is supported by a linear increase in hypertrophic remodelling and necrosis of the myocardium (Iwase et al., 1996). At the same time, overexpression of JPH2 albeit increases $Ca_v1.2$ channel insertion at the tubular membrane and attenuates pressure-overload induced heart failure, it does not allow for improvement beyond the baseline function of the heart which is critical in cases of severe end-stage HF (Guo et al., 2014; Salazar, Chen, and Rockman, 2007). Therefore, the discovery of novel mechanisms involved in $Ca_v1.2$ regulation can allow for better understanding of E-C coupling linked-diseases which to-date have no set cure, and the soluble NEM sensitive factor attachment protein receptor (SNARE) superfamily of proteins continue to demonstrate major interest in regulating cardiac function.

1.2 The Soluble NEM Sensitive Factor Attachment Protein Receptor (SNARE) Family

1.2.1 Historical Overview of SNARE Proteins

The process of lipid bilayer fusion, such as that during exocytosis is pivotal in mediating neurotransmitter release, neurohormonal secretion, insulin release, and protein transportation between organelles (Bock and Sheller, 1999). The respective process requires trafficking of vesicles in a highly selective and energy consumptive manner, alongside specialized sets of proteins to mediate their docking and fusion at target membranes. Within the last few decades, considerable effort has been made to elucidate the underlying mechanism, with the SNARE family being recognized as a major contributor.

The SNARE superfamily consists of greater than sixty members which have been identified in yeast and mammalian cells to-date (Han et al., 2017). Collectively, members of the SNARE family reside on a transport vesicle (v-SNAREs) and the target membrane (t-SNAREs) to facilitate vesicular trafficking and docking, alongside fusion of synaptic contents (Bock and Sheller, 1999). The discovery and interest in the field of SNARE proteins developed in the early 1980s, with a major focus on understanding the mechanism pertaining vesicular budding and fusion. Initial work by Bock and colleagues (1988) was imperative in today's understanding, as their purification of *N*-ethylmaleimide (NEM) demonstrated its inhibitory role against protein transportation. Furthermore, the effects were shown to be reversed upon insertion of the NEM-sensitive factor (NSF), restoring transportation between the cis and medial Golgi compartments. Through further assessment of cytosolic fractions isolated from Chinese hamster ovarian cells, yeast, and bovine tissue homogenates, Weidman et al. (1989) demonstrated a one-to-one interaction between NSF and its receptor, the soluble-NSF attachment protein-25 (SNAP-25),

highlighting the importance of a high-affinity NSF/SNAP-25 complex in mediating vesicular docking at the target membrane.

Within the same year of discovering SNAP-25 as a t-SNARE protein and NSF as a cofactor, the work by Trimble et al. (1988) demonstrated the role of a vesicular-associated membrane protein (VAMP) in driving trafficking within the eel, *Torpedo californica*. The mammalian homologue of VAMP – synaptobrevin – was discovered in the following year in rat brain extracts, where the expression was recorded to be greatest in purified vesicles (Baumert et al., 1989). Furthermore, synaptobrevin was shown to be localized in the outer membrane of each purified vesicle, playing a role in vesicular trafficking towards an acceptor compartment which thereby allowed for the categorization of VAMP/synaptobrevin as v-SNARE proteins.

At the time, it was also uncovered that membrane fusion occurs within 200 milliseconds of Ca^{2+} influx, hence suggesting a possible role of Ca^{2+} in mediating exocytosis. In 1993, Popoli identified the v-SNARE protein synaptotagmin – a homologue of protein kinase C (PKC) – highlighting its role in functioning as an important Ca^{2+} sensor and signal transducer. Furthermore, synaptotagmin was demonstrated to sense rapid changes between intracellular Ca^{2+} levels and the lipid bilayer, followed by initiating the vesicular fusion process. Through immunoblotting of neuronal vesicles acquired from rat brains, the final work by Bennet and colleagues (1992) allowed for discovery of two 35 kD proteins – p35A and p35B (commonly known as syntaxin-1A and syntaxin-1B) – which only differed in their cDNA coding sequence by 16% at the carboxyl terminal. Though discovered last, syntaxins were shown to be pivotal in interacting with neuronal Ca^{2+} channels (NTCCs) on the synaptic membrane, alongside other SNARE complexes to mediate vesicular docking at presynaptic active zones (Bennet et al., 1992). Collectively, the combined classifications of synaptobrevin and synaptotagmin as v-

SNAREs, alongside SNAP-25 and syntaxins as t-SNAREs sparked further research to elucidate the mechanism of SNARE-mediated exocytosis.

1.2.2 The Process of SNARE-Mediated Exocytosis

The SNARE complex is appropriately referred to as the "docking and fusion mechanism", with v-SNAREs and t-SNAREs interacting in an inseparable and coordinated manner to mediate exocytosis (Goda, 1997). To achieve this, SNAREs work in close relation with the Sec1/Munc 18-like (SM) family to tightly regulate the activity of membrane-bound syntaxins, which are comprised of an N-terminal regulatory domain (Habc), a C-terminal transmembrane domain, and a SNARE domain (H3). In the absence of an exocytotic event, the N-terminal folds over the SNARE domain, preventing its interaction with other v-SNAREs and docking of synaptic vesicles. Moreover, the interaction is further stabilized by Munc-18 binding to the N-terminal, hence keeping syntaxin in a "closed" conformation (Dulubova et al., 2007). Opposingly, when a synaptic vesicle is targeted for fusion and in close proximity to an acceptor compartment, Munc-18 relieves its inhibition which thereby allows for formation of a heterotrimeric structure between the SNARE domain, the membrane bound SNAP-25, and vesicle-bound synaptobrevin (Goda, 1997). Consequently, a synaptic vesicle is docked on the inner leaflet of the target membrane in a *cis* conformation, and activation of membrane-bound voltage-gated Ca^{2+} channels takes place. To mediate fusion of contents at the synaptic terminal, up to five Ca^{2+} ions bind to the Ca^{2+} sensor synaptotagmin – specifically at the C2A and C2B binding domains (Lai et al., 2014). The binding of Ca^{2+} generates sufficient energy to lock the vesicles in a *trans* confirmation, followed by zippering of the lipid bilayers and fusion of vesicular contents (Lai et al., 2014).

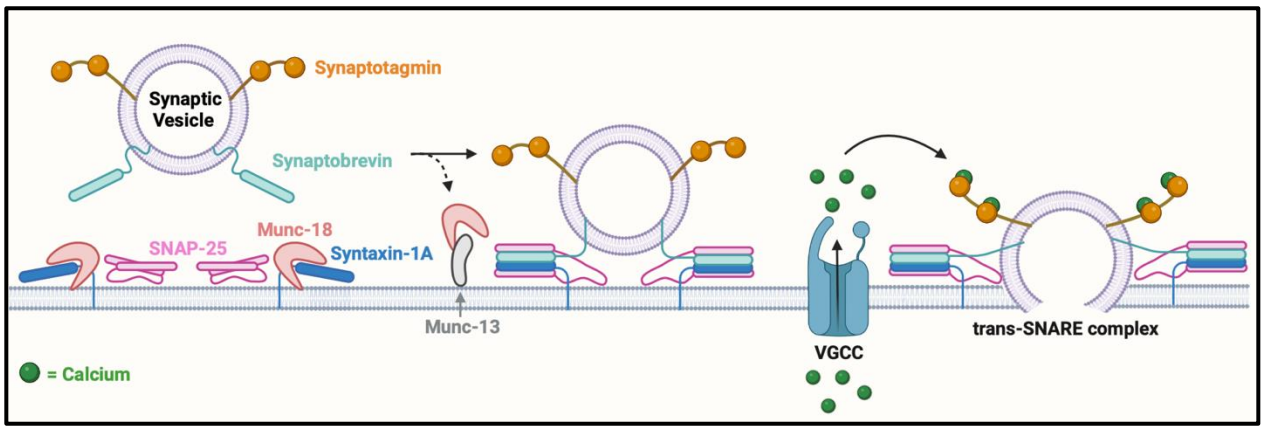

Figure 2: SNARE-mediated exocytosis of synaptic vesicles with a target membrane. In the absence of a proximal synaptic vesicle, Munc-18 tightly interacts with syntaxin-1A and maintains the t-SNARE in a closed confirmation. When a synaptic vesicle is in close proximity to the target membrane, Munc-13 interacts with Munc-18 and relieves its inhibition with syntaxin-1A, allowing for a *cis* heterotrimeric structure to form between syntaxin-1A, SNAP-25, synaptobrevin. Localized elevation in Ca^{2+} levels *via* VGCCs allows for Ca^{2+} binding to synaptotagmins C2A and C2B domains, causing the synaptic vesicle to lock on the target membrane in a *trans*-complex, and hence allowing for fusion of synaptic contents. *VGCCs = voltage-gated Ca^{2+} channels*. Illustration was created on www.biorender.com

1.2.3 Expression of SNAREs in the Heart

In the process of vesicular docking and fusion, syntaxin demonstrates a pivotal role in forming the highly stable SNARE complex, alongside regulating intracellular Ca^{2+} currents at the synaptic terminal. Consequently, abnormal expression of syntaxin-1A as assessed through *in vitro* neuronal knockout demonstrates a severe impairment in docking of competent vesicles, alongside a 40% decline in the percentage of surviving neurons (Vardar et al., 2016). Moreover, the knockout triggers impaired neurotransmission which can be recovered upon introduction of a syntaxin-1A mutant, thereby making its expression mandatory in signal transduction (Vardar et al., 2016). The functional role of syntaxin-1 has also been elucidated *in vivo* within fruit flies and worms, whereby the absence demonstrated complete lethality due to disruption in synaptic transmission, germinal cell division and viability, and neuronal maintenance (Burgess, Deitcher

and Schwarz, 1997; Schulze and Bellen, 1996). However, the functional role of syntaxins is not limited to the nervous system, as multiple isoforms have been localized across a broad range of tissues including the pancreas, lungs, and even the heart.

The initial discovery of syntaxin-1A and syntaxin-1B demonstrating an 84% homology in amino-acid sequencing led to the identification of other isoforms, particularly the localization of syntaxin-5 in the early secretory pathway, alongside subcloning of cell-surface syntaxins-2, 3 and 4 (Bennet et al., 1993). To-date, 18 isoforms of syntaxins have been identified, expressing wide cellular localization patterns from presynaptic plasma membranes in the neuronal network, to mediating insulin secretion in the pancreas, and skeletal muscle glucose-transporter trafficking (Teng, Wang and Tang, 2001). Moreover, the expression and role of syntaxins have also been revealed in the heart, particularly through the work by Peters et al. (2006) on isolated neonatal and adult mice hearts. Through their initial studies *via* Western blotting and co-immunoprecipitation, Peters and colleagues (2006) were able to highlight the expression of two highly-stable SNARE complexes: (1) the VAMP-1/VAMP-2, SNAP-23 and syntaxin-4 complex in neonatal cells which had been previously identified in glucose-transporter trafficking (Slot et al., 1997), and the novel (2) VAMP-1/VAMP-2, SNAP-25, and syntaxin-1A complex in the adult mouse heart. Moreover, the complexes were shown to co-immunoprecipitate with atrial natriuretic peptides (ANP) granules – a hormone which tightly regulates blood volume/pressure, cardiac myocyte growth, and is overexpressed in cases of diseased states such as hypertension and congestive heart failure (Woods, 2004).

The continued work by Ferlito et al. (2010) further pursued the process of SNARE-mediated ANP release in neonatal rat cardiomyocytes. Particularly, the roles of syntaxin-4, VAMP-1 and VAMP-2 were explored, since other syntaxin and VAMP isoforms are not detected

at the neonatal states (Peters et al., 2006). By ultracentrifuging cardiomyocytes and allowing for separation of granular, plasma membrane, and cytoplasmic fractions, ANP, VAMP-1 and VAMP-2 were shown to be expressed only within granules, whereas syntaxin-4 was expressed in both the granules and plasma membrane. Furthermore, utilization of silencing RNAs (siRNAs) to perform targeted knockdown of VAMP-1, VAMP-2 and syntaxin-4 revealed a significant decrease in ANP secretion upon endothelin-1 stimulation, thereby highlighting the importance of the neonatal SNARE complex in regulating ANP exocytosis. The collective efforts by Peters et al. (2006) and Ferlito et al. (2010) highlighted a novel role of SNARE proteins in regulating ANP release within neonatal myocytes. However, the role of SNARE proteins are not limited to exocytosis, as syntaxins are also able to interact with and regulate ion-channel activity.

1.2.4 Syntaxin-Mediated Regulation of Voltage-Gated Ca^{2+}-Channel Currents

SNARE-mediated exocytosis demands a rapid and reliable mechanism of Ca^{2+} current regulation at the synaptic terminal in order to mediate the process of vesicular fusion. Syntaxin-1A has demonstrated a major role, as co-expression with neuronal (N-type) Ca^{2+} channel in *Xenopus* oocytes triggers a significant decrease in the inward Ca^{2+} current (Bezprozvanny et al., 1995). Moreover, deletion of syntaxin-1A's C-terminal alleviates the inhibition, hence suggesting the importance of the transmembrane domain in maintaining NTCC in an inactive state (Bezprozvanny et al., 1995). The role of syntaxin-1A has also been explored in relation to other Ca^{2+} channels such as the T-type Ca^{2+} channels which are expressed within neurons, cardiac myocytes, fibroblasts, and pacemaker cells of the heart (Kopecky et al., 2015). Similar to the previous findings, Weiss et al. (2012) demonstrated a stable complex between T-type Ca^{2+} channel ($Ca_v3.2$) and syntaxin-1A in neuronal cells, whereby co-expression decreased channel

availability by shifting the steady-state inactivation towards hyperpolarized potentials. Moreover, utilization of botulinum toxin C1 to cleave the transmembrane domain abolished the inactivation, elucidating the importance of the membrane anchor in syntaxin-mediated regulation of Ca^{2+} currents (Weiss et al., 2012). Intriguingly, syntaxin-1A has also shown to regulate the activity of L-type Ca^{2+} channels (LTCC) in neuronal cells, mediating processes such as gene expression, synaptic efficiency, and cell survival (Lipscombe et al., 2004). However, the importance of the mechanism expands beyond neuronal cells, as L-type Ca^{2+} channels function as the primary mediator in cardiac E-C coupling, and thereby the relationship should be further explored.

1.2.5 Syntaxin-1A Regulates L-Type Ca^{2+} Channel Inward Currents

The direct coupling of syntaxin-1A with L-type Ca^{2+} channels was demonstrated by Wiser and colleagues in 1996, whereby co-injection of their complementary RNAs (cRNAs) in *Xenopus* oocytes resulted in a 60% decline in LTCC currents. To add, though syntaxin-1A and SNAP-25 are both t-SNARE proteins embedded within the plasma membrane and demonstrate interaction with LTCCs, the addition of cardiac α_1, α_2, and δ-subunit cRNA (forming the stabilized α_1 /α_2 / δ complex) with SNAP-25 resulted in no decline in inward currents (Trus et al., 2001). Opposingly, the co-expression of the stabilized complex with syntaxin-1A reduced the inward current by 95% which could not be rescued upon SNAP-25 addition, hence suggesting syntaxin-1A's unique role in regulating the α_1 pore-forming currents (Tus et al., 2001).

The site-specific interaction between syntaxin-1A and LTCC has also been elucidated by assessing structural differences between syntaxin-1A and syntaxin-2. Amongst the two isoforms, the primary differences arise at the C-terminal transmembrane domain, where STX1A contains two vicinal cysteine residues – Cys-271 and Cys-272 – as opposed to valines in STX2 (Wiser et

al., 1996). Upon a double mutation of Cys-271 and Cys-272 into valines, syntaxin-1A lost its inhibition against LTCC, yet the inhibition was maintained with a single cysteine mutation (Arien et al., 2003). Hence, it is suggested that unlike valines, syntaxin-1A's cysteines may be required to form disulfide bonds with $Ca_v1.2$, consequently stabilizing the channel in an inactive state due to a strong protein-protein intermolecular interaction (Arien et al., 2003). Furthermore, this interaction can be deemed extremely important in regulating LTCC function, as lack of disulfide bond formation has been linked to malfunctioning of membrane-localized receptors and proteins (Tarnow et al., 2003; Hänggi et al., 2006). Alongside the transmembrane anchor, the cytosolic domain of syntaxin-1A also interacts with the α_1 pore-forming subunit at domains II and II of LTCC. Moreover, recent findings by Sherman et al. (2017) have demonstrated co-localization of syntaxin-1A with the α_1 pore-forming in ~1:1 nanoclusters, highlighting a tight link between L-type Ca^{2+} channel activity and inward current generation.

Collectively, the interaction between syntaxin-1A and LTCC has been studied extensively within an *in vitro* setting (i.e., HEK293 cells, neuronal cells, *Xenopus* oocytes). However, the functional relationship has been assessed minimally within an *in vivo* setting – particularly within the heart, where the interaction could demonstrate major interest as abnormal LTCC regulation can disrupt electromechanical signalling, leading to decreased ventricular function and consequent pathological hypertrophic remodelling; the precursor to heart failure.

1.3 Cardiac Hypertrophy

1.3.1 Pathological vs. Physiological Hypertrophic Remodelling

The heart is required to continuously eject blood in an efficient manner to mediate oxygen and nutrient supplementation throughout the body. To achieve such homeostasis, a range of complex biological systems coordinate with the heart's contractile mechanism to continuously adapt to alterations in pressure and blood volume. The primary mechanism by which this takes place is cardiac hypertrophy, defined by an enlargement of cell size, elevation in protein synthesis, and heightened organization of sarcomeres (Samak et al., 2016). Moreover, the type of hypertrophic response is dependent on the initial stressor, such as physiological hypertrophy which takes place during normal myocardial growth while pathological hypertrophy is observed during cardiac dysfunction.

Physiological hypertrophy is a natural adaptive mechanism of the heart which occurs in response to elevated myocardial stretch. As noted during pregnancy, normal growth of children or during exercise, an increase in venous return triggers an enlargement of cardiomyocytes to ensure appropriate blood supply and thereby nourishment across the heart muscle (Shimizu and Minamino, 2016). Furthermore, physiological adaptation is often accompanied by normal or increased contractile function of the heart, with no abnormal changes to sarcomeric structure (Weeks and McMullen, 2011). Consequently, the global alterations are not considered to be precursors of heart failure as the effects are short-lived and do not impose any permanent structural or functional changes to the myocardium (Shimizu and Minamino, 2016).

Opposingly, pathological hypertrophy occurs due to abnormal blood flow to the myocardium in response to hypertension, myocardial infarction, and mitral valve regurgitation. As a result of hemodynamic overload, there is a reduction in the contractile mechanism of the

heart (decreased ability to eject blood efficiently), elevated cell infiltration, fibrotic remodelling, and ventricular stretch with impaired return which drives the heart towards a failing state (Shimizu and Minamino, 2016). Particularly in left-ventricular pathological hypertrophy, remodelling can impair the homeostatic mechanism for blood ejection which can lead to severe heart failure (Shimizu and Minamino, 2016). Moreover, cardiomyocyte shape is altered beyond the capabilities of the capillaries to provide the muscle with sufficient nutrient exchange, often resulting in myocardial remodelling, hypoxia, and cardiomyocyte death (Shimizu et al., 2010).

1.3.2 Eccentric vs. Concentric Hypertrophic Remodelling

Under physiological settings, cardiomyocytes are permanently terminated at the adult stage and do not undergo further proliferation within mammals. During hypertrophic remodelling however, the myocardium adjusts to the stress response by altering the cell size and sarcomeric structure to maintain cardiac function. As a result, cardiomyocytes can grow, shrink, and even undergo apoptosis at localized regions of elevated stress. Hence, based on the geometry of the heart alongside the stress response, the heart adapts by undergoing two different modes of hypertrophic remodelling; concentric and eccentric hypertrophy.

As observed during hypertension and valvular disease, an abnormal elevation in ventricular pressure can give rise to *concentric* remodelling, whereby cardiomyocytes become enlarged to attenuate the pressure-overload response. During this response mechanism, the cardiomyocyte width becomes greater than the length as sarcomeres are added in parallel, resulting in thickening of ventricular walls and septum (Lalande and Johnson, 2009). By doing so, concentric remodelling aims to counter the pressure generated at the ventricles by thickening the myocardium to push blood against the pressure gradient and into systemic circulation.

Concentric remodelling from hypertension generates significant risk towards cardiovascular death and mortality, primarily since elevated pressure can decrease LV compliance, impairing the heart's ability to fill blood effectively and trigger diastolic dysfunction (Lalande and Johnson, 2009).

Diseases including hypertension and aortic stenosis can also elevate the ventricular pressure beyond the capabilities of the chamber, with prolonged wall stress leading to a decompensatory response. A collapse in ventricular wall structure, as noted in diseases such as mitral valve regurgitation causes an overload of volume, resulting in thinning of the ventricular walls (Dos Santos et al., 2021). This form of remodelling, termed *eccentric* hypertrophy occurs during ventricular cavity dilation, and is characterized by elongation of cardiomyocytes due to addition of sarcomeres in series. Elongation of cardiomyocytes thereby attenuates the volume-overload response by increasing the surface area for blood in the ventricular cavity, but consequently impairing the contractile response of the heart. Moreover, eccentric remodelling is associated with elevated cardiomyocyte apoptosis and fibrotic remodelling which collectively decrease the compliance of the chamber and can culminate in both diastolic and systolic dysfunction (Dos Santos et al., 2021). Collectively, pathological eccentric hypertrophy can increase the risk of cardiovascular morbidity, and continuous to present as the primary reason for heart failure with reduced ejection fraction (HFrEF) (Nauta et al., 2020).

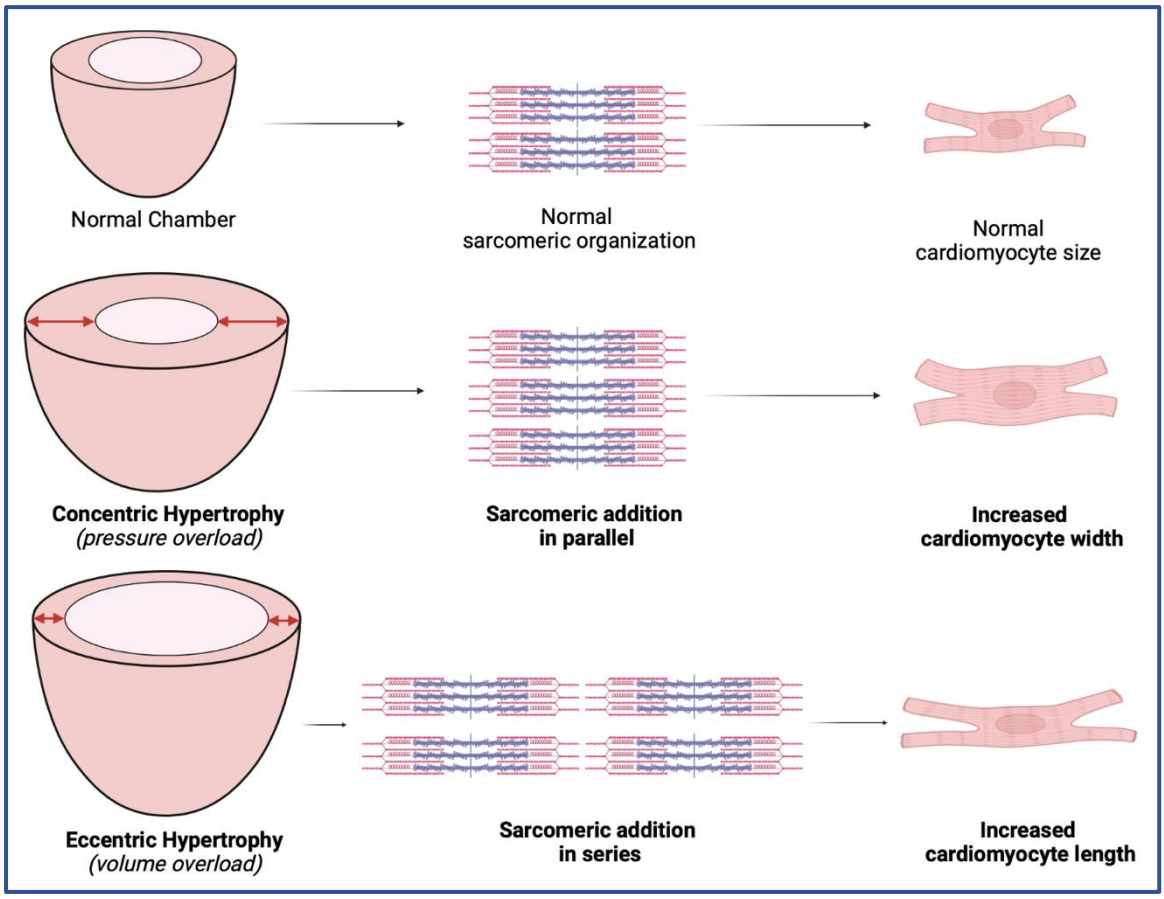

Figure 3: Hemodynamic overload results in alteration of sarcomeric structure. Concentric hypertrophy occurs in response to pressure overload, whereby sarcomeres are added in parallel resulting in increased myocyte width. Addition of sarcomeres in series occurs in volumetric eccentric hypertrophy, which causes an increase in cardiomyocyte length. Illustration was created on www.biorender.com

1.3.3 ANP Modulates the Hypertrophic Response Mechanism

ANP is a member of the natriuretic peptide family which plays a vital role in regulating blood fluid and pressure and homeostasis. The production of ANP occurs primarily within atrial myocytes, where it is stored in granules and triggered for release upon overdistention of the atria (Kessler-Icekson, 2002). ANP production also takes place in the ventricles during neonatal development, however only a minority of cells produce ANP in the adult ventricle (Benvenuti et

al., 1997). Therefore, the expression and thereby release of ANP is highly conserved to the atria in the adult heart, where ANP can be signalled for release upon mechanical stretch of the chamber or through a regulated pathway.

ANP and its structurally related hormone factor, brain natriuretic peptide (BNP) collectively demonstrate natriuretic and diuretic roles within the heart. Upon stretch of cardiac walls induced by pressure or volume overload, activation of baroreceptors lining the atrial and ventricular walls trigger the release of ANP and BNP into circulation. At the same time, baroreceptors signal the hypothalamus to inhibit the production of vasopressin, thereby inhibiting water retention and a rise in blood pressure. Release of ANP/BNP consequently activates a series of events to maintain fluid and pressure homeostasis by interacting with the renal system, causing: (1) vasodilation of the glomerulus which increases the filtration rate and thereby excretion of water and urine (diuresis), (2) supressing the reabsorption of sodium in the collecting duct which is hence excreted in urine (natriuresis) (Bowen, 2018). The collective effects of diuresis and natriuresis therefore reduce the circulating blood volume and pressure, resulting in diminishing of atrial stretch and decreased stimulation of ANP/BNP release. By tightly maintaining a homeostatic balance of fluid and pressure within the cardiovascular system, ANP/BNP also play a major role in functioning as anti-hypertensive hormones. For instance, ANP can inhibit the release of renin which functions as a vasoconstrictor to elevate blood pressure (Bowen, 2018). Moreover, ANP also inhibits hypertrophic gene signalling by preventing calcineurin-mediated nuclear factor of activated T-cells (NFAT) translocation into the nucleus, which under hypertrophic conditions activates the phenomenon of “fetal gene expression”.

Under pathological hypertrophic settings, the biomechanical stressed faced by cardiomyocytes can activate an intrinsic web of signalling pathways, leading to alterations in the cardiac gene expression. The molecular changes observed during hypertrophy mimic those observed during fetal development, with pathological remodelling often being accompanied by reactivation of the fetal genes (Dirkx et al., 2013). At the fetal state, the expression of ANP is elevated in the ventricle but the capacity declines and becomes exclusive to the atria soon after birth (Smith et al., 1989). When elevated workload is imposed on the heart such as that during chronic hypertension, myocardial infarction, or heart failure, the number of ANP-producing cells are significantly elevated in the left ventricle (Kessler-Icekson, 2002). A rise in ANP levels can thereby inhibit the NFAT signalling pathway and prevent re-activation of fetal genes, alongside inhibit the development of vascular smooth muscle cells, endothelial cells, and cardiac fibroblasts (Hayashi et al., 2004). Therefore, elevated levels of ventricular ANP serves as a major assessor for hypertrophic remodeling, alongside a switch in sarcomeric gene expression as well.

1.3.4 Fetal Gene Expression: α-Myosin Heavy Chain to β-Myosin Heavy Chain Switch

The contractile genes of the cardiac muscle are expressed in a tissue-specific and developmental stage-specific manner, with myosin being the primary protein responsible for inducing contractions. Myosin is a hexametric protein consisting of two myosin heavy chains (MHCs), four light chains and a myosin head which collectively induce contractions *via* ATP hydrolysis (Gupta, 2004). Within cardiomyocytes, MHCs are encoded by two separate genes – α-MHC and β-MHC – which can combine to produce three isoforms in the ventricles: V1 (αα homodimer), V2 (α/β heterodimer), and V3 (ββ homodimer). Amongst the isoforms, αα-MHC has the fastest ATPase activity allowing for the most rapid contractile velocity (Miller et al.,

1989). However, the fast ATPase activity makes αα-MHC the most energy inefficient isoform, whereas the ββ-MHC isoform demonstrates slower ATPase activity and filament velocity but the greatest cross-bridge force at the highest economy (Krenz and Robbins, 2004). To compensate for the differences in hemodynamic load between the atrial and ventricular chambers, a difference in MHC isoform expression is thereby noted in both rodents and larger mammals.

During late fetal states, rodents primarily express the β-MHC isoform in the atria however immediately upon birth, α-MHC elevates significantly in the ventricle as the dominant isoform (>90%) (Gupta, 2004). Due to smaller rodents such as mice, hamster and rats having high surface area to volume ratios, a fast ATPase activity constitutes to a rapidly contracting heart, thereby ensuring continuous production of energy and metabolism (Miyata et al., 2000). Opposingly, the adult atria primarily contains the β-MHC isoform due to the lower hemodynamic load, ensuring efficient ejection of blood into the ventricular chambers prior to rapid ejection. The co-expression of α-MHC and β-MHC is also observed in parts of the heart requiring peristaltic contractions, such as the atrioventricular junction which functions as a bridge between the two chambers (Lyons et al., 1990).

Under diseased settings such as heart failure and/or pathological hypertrophy, a significant change in the relative expression of myosin isoforms is recorded to maintain appropriate contractile force. During hemodynamic overload, sarcomeric gene expression is also adapted to the fetal state, whereby β-MHC elevates in the ventricle and becomes the dominant isoform. The switch is suggested to transition the heart into a more energy conservative mode, decreasing the contractile function which may outweigh the benefits of rapid contraction (Krenz and Robbins, 2004). Consequently, a rise in ventricular β-MHC and β-MHC/α-MHC ratio has

been recorded in patients with cardiomyopathy, with subsequent repression of the α-MHC gene (Taegtmeyer, Sen and Vela, 2013).

1.4 Previous Work and Hypotheses

1.4.1 Objective and Previous work by Tsushima Lab

The SNARE superfamily comprises of a broad range of vesicular- and target-bound proteins which interact in a coordinated manner to induce synaptic fusion. More specifically, t-SNARE syntaxin-1A has demonstrated the ability to negatively regulate L-type Ca^{2+} channel currents *via* the transmembrane and cytosolic domains, which demonstrates major interest in heart research as LTCC is the primary mediator in cardiac E-C coupling. Since studies demonstrating the relationship have been limited to *in vitro* analyses, the research conducted by Tsushima lab aims to elucidate the importance of syntaxin-1A-LTCC interaction and thereby E-C coupling *in vivo* within the mouse heart. Due to abnormal LTCC regulation being linked to failure of human ventricular myocytes, contractile deficits, and heart failure, further understanding syntaxin-1A mediated LTCC activity can branch a novel pathway for better assessment of E-C coupling-linked diseases (Chen et al., 2002; Shaw and Colecraft, 2013).

Since STX1A demonstrates negative regulation against LTCC currents, previous members hypothesized that cardiomyocyte-specific syntaxin-1A knockout (KO) would alleviate LTCC inhibition, resulting in increased Ca^{2+} flux. Consequently, an elevation in cytosolic Ca^{2+} levels would induce a stronger CICR event, improving the contractile force generated by the heart. As demonstrated by Virdi (2020, 2022), cardiomyocyte-specific KO of STX1A did not improve the contractile function as hypothesized. Rather, through utilization of *in vivo* 2-D echocardiography, a significant decline in the ejection fraction was recorded (percentage of

blood leaving the ventricle per contraction cycle), alongside volume-overload within the left-ventricle. Moreover, the left-ventricle demonstrated contractile dysfunction which persisted for three-weeks prior to recovery, thereby making the effects of STX1A KO transient.

1.4.2 Hypotheses

The pilot study conducted by Virdi (2020) elucidated a novel mechanism of STX1A in the heart, whereby KO worsened the heart function as opposed to improving the contractile force as proposed. Building onto the previous study, it is my hypothesis that STX1A may demonstrate a major role in regulating LTCC function and stabilization to the t-tubular membrane, as such that knockout of STX1A will disrupt its cysteine-cysteine bond formation with LTCC and result in an event such as channel internalization, reducing the surface-level expression (*N)* and eliciting a weaker CICR event. To initially confirm that KO of STX1A worsens the heart function, findings by Virdi (2020) will be repeated in both male and female counterparts through conventional echocardiographic analysis and speckle-tracking analysis. It is suggested that female mice will demonstrate quicker recovery in contractile function due to contractile proteins demonstrating a lower threshold and greater sensitivity to Ca^{2+} in female hearts (Parks and Howlett, 2013; Schwertz et al., 2004).

Findings by Virdi (2020, 2022) also demonstrated a return in cardiac function by week 3, whereby the heart demonstrated a recovery in contractile function hence making the effects of STX1A KO transient. Therefore, it is hypothesized that hypertrophic remodeling of the myocardium – i.e., alteration in cardiomyocyte and sarcomeric structure – is pivotal in adapting to the stress-response induced by STX1A KO. Particularly, an elevation in E-C coupling gene transcripts and alteration in cardiomyocyte cell length/width will be assessed *via* RT-qPCR and histological analysis respectively to confirm the hypothesis of myocardial remodelling induced

post-KO. Moreover, it is suggested that severe stress – such as volumetric overload observed by Virdi (2020, 2022) – can also induce pathological remodelling of the heart, causing localized fibrotic deposition of the myocardium. To assess for collagen deposition, the ventricular chambers will be stained with Masson's trichrome post-KO. Lastly, since hypertrophic remodelling is associated with fetal gene reprogramming, whereby the myocardium re-expresses fetal genes to regulate hemodynamic overload while preventing energy consumption, it is hypothesized that an elevation in ANP mRNA transcript levels will be observed to reduce the blood volume, and β-MHC expression will be greater than α-MHC in the left-ventricle to reduce ATP expenditure of the dysfunctional myocardium.

1.5 Emphasis on female-mice in research

According to a meta-analysis conducted on 28,000 articles published amongst *Circulation Research, Hypertension, Stroke* and many more, it was reported that 71.6% of the studies exclusively utilized male subjects in their research (Ramirez et al., 2017). The reasoning for the lack of female utilization in studies is flawed, arising due to the misassumption that their oestrous cycle causes hormonal variations every 4-5 days which can impact the reliability of the results (Ramirez et al., 2017). However, it has been repeatedly recorded that female rodents do not demonstrate any more variability than their male counterparts, particularly in blood pressure, heart rate, basic cardiac parameters, organ weight, body weight/fat, behavioural, neurological and histological analyses (Becker, Prendergast and Liang, 2016). Not only is there a lack of differences in the key traits, but no variability arises throughout the different phases of the oestrous cycle (Becker, Prendergast and Liang, 2016). Conclusively, it is imperative to include female mice in all research studies as differences do develop in certain biological processes such as pain processing, and lack of pre-clinical research on female mice has yielded poor treatment outcomes for women, and even unfortunate fatalities (Beery, 2018). Consequently, throughout the course of my thesis, a major attempt will be made to ensure participation of female subjects in each experimental analysis, as the impact of STX1A KO has been well-established in the male counterparts (Virdi, 2020; Virdi, 2022).

CHAPTER 2: METHODS

2.1 Cre-mediated STX1A KO Model

The Cre-loxP mechanism was utilized to conduct *in vivo* cardiomyocyte-specific knockout of STX1A in the C57Bl/6 murine model. To achieve this, mice expressing Cre-recombinase under the cardiac-specific α-myosin heavy chain promoter were received from Dr. Jeffery Molkentin (Cincinnati Children's Hospital Medical Centre, Cincinnati, OH) and cross-bred with C57BL/6 mice expressing loxP sites between exons 2 and 3 of STX1A (Dr. Herbert Gaisano – University of Toronto, Toronto, ON). The F2 generation were further cross-bred to produce mice that were wild-type ($STX1A^{-/-}$ Cre^{+}), heterozygous ($STX1A^{flox/-}$ Cre^{+}) and/or homozygous ($STX1A^{flox/flox}$ Cre^{+}) at both loci, with all three groups being studied throughout the course of the thesis. All mice were housed within a ventilated, 12:12 hour light-dark cycle room maintained at 22-24°C and supplied with a normal chow diet alongside water *ad libitum*. Both male and female mice (ages 2-5 months) were utilized throughout the study, and all procedures conducted were approved by the York University Animal Care Committee in accordance to the Canadian Council of Animal Care.

2.2 Tamoxifen-induced Cre activation

Tamoxifen – an estrogen receptor antagonist – was administered intraperitoneally to activate the Cre-recombinase mechanism and induce site-specific excision of the STX1A gene. Initially, tamoxifen citrate (Cayman, Cay11629-5) powder was dissolved in peanut oil (Sigma Aldrich, 8002-03-7) until a final concentration of 10mg/mL was achieved. Following, the

solution was gently vortexed three times (3x) in 30 second pulses until the citrate powder dissolved – as apparent by a yellow-milky solution. To ensure complete homogeneity, the Eppendorf tube was sonicated over ice using an electrical sonicator 3x in 30-40 second pulses, and cycles were repeated as needed to ensure complete dissolving of tamoxifen. The solution was then stored on ice for immediate use or wrapped in aluminum foil and kept at 4°C for long-term storage. To perform tamoxifen treatment, mice were initially sedated with 1.5% isoflurane until a lack of toe-pinch reflex was noted. Mice were then scruffed gently, and the peritoneal region was sprayed with 75% ethanol followed by tamoxifen injection. Both male and female wild-type, heterozygous and homozygous mice were injected with a concentration of 40 mg/kg body weight over a course of four-days, which has shown to be sufficient in inducing Cre-activation without secondary effects (Bersell et. al, 2013).

2.3 Tail Sample Acquisition and Polymerase Chain Reaction (PCR) Genotyping

Genotyping was conducted *via* acquisition of tail samples followed by DNA isolation and Real-Time (RT) PCR analysis. Prior to tail collection, all mice were aged to 21 days or until weaned from the mother. Upon being weaned, mice were individually placed within a clear plastic container supplied with 1.5% isoflurane. The anesthetic was continuously administered until a lack of toe-pinch reflex was noted, alongside a decrease in breathing rate to 1-2 breaths per second. Upon sedation, mice were removed from the container, and small tail clippings were acquired (~0.5cm) followed by application of Kwik stop styptic powder to limit bleeding and infections. The tail clippings were collected in 1.5 mL Eppendorf tubes and incubated in 300µL of 0.05N NaOH for 1 hour in a dry bath at 90°C. Once digestion was complete, the DNA was

neutralized with 100µL 0.5M Tris-HCl (pH 8.0), samples were vortexed gently 3x for 10 seconds and placed on ice for immediate PCR amplification or stored at -30°C for later use.

RT-PCR was conducted to amplify and assess the expression of two genomic sequences: STX1A loxP sequences and the MerCreMer complex (MCM). To begin, 18µL PCR reaction tubes were made, consisting of 10µL 2X HS-Red Taq PCR Mastermix (Wisent Biocenter, 801-200-DM), 4µL DNAse/RNAse free water, 1µM of forward and reverse primer each, and 2µL of neutralized tail clippings. Forward and reverse primer sequences are noted below, with protocol of STX1A amplification consisting of polymerase activation at 95 °C for 5 min, 34 cycles of 95 °C for 30 sec, 60°C for 30 sec, and 72 °C for 30 sec, and MCM amplification beginning with polymerase activation at 95 °C for 5 min, followed by 39 cycles of 95 °C for 30 sec, 50°C for 30 sec, and 72°C for 30 sec (Virdi, 2020). Samples acquired from PCR amplification were resolved on a 1.5% agarose gel and imaged using the Alpha Innotech Alpha Imager Hp System.

Gene	Forward Primer Sequence	Reverse Primer Sequence
STX1A	5’ GCT GCA GAA GCA AGA GAA CC’3	5’CAG CCA TAC AAA AAC CAC CA’3
MCM	5’ CGT CCT CCT GCT GGT ATA G’ 3	5’GTC TGA CTA GGT GTC CTT CT’3

2.4 Heart Tissue Isolation and Digestion

Heart tissue isolation was performed by initially placing mice within an enclosed container supplied with 1.5% isoflurane until no toe-pinch reflex was noted, followed by an intraperitoneal injection of 1000 USP heparin (hepalean, Organon Teknika, Toronto, ON). Mice were then placed in their initial cages to allow for acclimation and circulation of heparin for 10

minutes. Upon acclimation, mice were sedated and continuously supplied with 1.5% isoflurane through a nose-cone, with all four limbs being secured onto a surgical blanket. Once a breathing rate of 1-2 breaths/second was recorded, the chest and abdominal regions were sprayed with 75% ethanol and a deep incision was performed below the diaphragm. The skin was lifted, and incisions were followed cranially along the left and right abdominal regions until contact was made with the ribs. Quick lateral cuts were performed to the left and right rib, followed by utilization of a haemostat to roll back the ribs allowing for exposure of the heart. Upon removal of excess fat and the pericardial sac, the heart was lifted from the base using curved forceps, and an incision was made to the aorta freeing the heart from the chest cavity. The heart was then immediately placed in ice-cold 1X Phosphate-Buffered Saline (PBS) and washed generously to remove excess blood, followed by two consecutive washes in fresh 1X PBS. Lastly, the left-ventricular wall was isolated under the microscope while immersed in ice-cold 1X PBS, cut into small pieces, and stored in a tissue collection tube over ice for immediate use or at -30°C for long-term storage.

To digest heart samples, ~0.5g of heart tissue was weighed out and transferred to a 1.5mL Eppendorf tube along with 200µL of NP-40 Lysis Buffer (50mM Tris-HCl pH 8.0, 150mM NaCl, 1% NP-40, 1 Complete Mini-EDTA free protease inhibitor tablet). The sample was then sonicated over ice 3x in 30 second intervals using an electric sonicator, followed by incubation at 95°C for 5 minutes. Samples were then centrifuged at 4°C for 15 minutes at 12,000 g, followed by transfer of supernatant to a new Eppendorf tube which was stored on ice till use or at -30°C for long-term storage.

2.5 Bradford-Lowry Assay for Protein Concentration

Total protein concentration from the left-ventricular free wall was determined utilizing the Bradford-Lowry protein assay. Initially, a standard of 1 μg/μL Bovine Serum Albumin (BSA) was freshly prepared and stored on ice, from which serial dilutions of 1, 0.5, 0.25, 0.125, 0.0625 μg/μL BSA were prepared. Next, a light-sensitive cuvette box was gathered followed by placement of seven cuvettes, with 20μL of each serial dilution being added to five cuvettes, while the remaining two cuvettes consisting of a blank (20μL MilliQ-water) and the sample (18μL MilliQ-water with 2μL of heart supernatant). Within a 1.5mL Eppendorf tube, Bradford Reagent A and S (Bio-Rad Protein Assay Kit 1, #5000001) were combined in a 50:1 ratio to make a working volume of 1mL, and the tube was vortexed briefly. To each cuvette, 100μL of the Bradford Reagent A was added followed by 800μL Bradford Reagent B in a light-sensitive manner. Upon addition, the cuvette box was incubated on an orbital plate shaker for 20 minutes with gentle agitation, and following incubation, the absorbance was measured using an Eppendorf photometer at 660nm. Absorbance values were plotted against the relative BSA concentrations to produce a standard curve, and sample protein concentrations were extrapolated.

2.6 Western Blotting

Samples were prepared for Western blotting by diluting the appropriate lysate volume with 17μL 6X SDS loading buffer (0.28M of 1M Tris-HCL pH 6.8, 30% v/v glycerol, 10% w/v SDS, 0.5M dithiothreitol, and 0.0012% w/v bromophenol blue) and MiliQ-water until a final volume of 100μL was attained. The samples were briefly vortexed, and equal amounts of protein (30μg) alongside 3μL pre-stained ladder (FroggaBio, PM008-0500) were resolved onto a

polyacrylamide gel, comprising of 15% running gel (ultrapure water, 30% acrylamide mix, 1.5M Tris-HCl pH 6.8, 10% SDS, 10% ammonium persulfate, and TEMED) and 5% stacking gel (ultrapure water, 30% acrylamide mix, 1M Tris-HCl pH 6.8, 10% SDS, 10% ammonium persulfate, and TEMED). A voltage of 100V was applied for 30 minutes to initially stack the protein samples, followed by 150V for 1.5 hours until the proteins reached the bottom of the running gel.

The running gel was safely separated and transferred onto a 0.45µM nitrocellulose membrane (BioRad, #1620115) pre-soaked in 1X Transfer Buffer solution (25mM Tris base, 192 mM glycine, and 10% methanol) under slow electrophoretic conditions (30V, 24 hours over ice). On the following day, the nitrocellulose membrane was separated from the transfer apparatus and washed in 1X Tris-buffered saline (TBS-T) (2mM Tris base, 13.7mM NaCl, pH 7.6) supplemented with 0.1% tween. Following three sets of washes for five minutes each (3 x 5 mins), the membrane was blocked for 1-hour at room temperature on an orbital shaker with 5%w/v skim milk powder dissolved in 20mL 1X TBS-T. Upon blocking, the membrane was washed (3 x 5 mins) followed by primary antibody incubation for one hour in a 1:1000 dilution (1µg antibody dissolved in: 1% w/v of BSA in TBS-T and 0.02% v/v of 10% NaN_3). The primary antibody was stored at 4ºC after use, and the membrane was washed again with 1X TBS-T (3 x 5 mins). Lastly, the membrane was incubated in secondary antibody diluted to a concentration of 1:10,000 (1µg antibody dissolved in equal parts 1% BSA and 1X PBS), followed by a 15-minute wash period and imaging using a LI-COR odyssey infrared imaging system. The entire Western blotting protocol took place under room temperature conditions, aside from protein transfer which was conducted over ice.

2.7 2-D Echocardiography: M-Mode Analysis

VisualSonics Vevo 2011 high-resolution ultrasound imaging system (FUJIFILM VisualSonics, Toronto, ON) was utilized to perform transthoracic 2-D echocardiography on C57BL/6 mice. Mice were carefully transferred to a clear rectangular container connected to a charcoal filter and isoflurane vaporizer, carrying isoflurane *via* oxygen. Isoflurane levels of 2-2.5% were used to initially anesthetize the mice until no toe-pinch reflex was noted, followed by carefully placing the mice on a heat pad in the supine position. The snout of the mice was then inserted into a snout cone which constantly supplied isoflurane at 1-1.5%. Upon application of electrode gel to the gold electrodes, the front and hind paws were taped down twice on all four electrodes to ensure strong connection. The tip of a rectal thermometer was then covered in a lubricant (Vaseline™) prior to slow insertion, further taped down, and the temperature on the heat pad was adjusted until the internal body temperature stabilized to 36.9-37.2°C. At the same time, isoflurane rates were adjusted to maintain respiratory rate of 90-110 breaths per min.

Upon stabilization of the internal body temperature, respiratory rate, and isoflurane levels, the fur on the thorax was removed *via* application of a depilatory cream (Nair™) for 30 seconds. Hair was removed by gentle strokes with Kimwipes, while ensuring the snout does not exit the cone. Upon reveal of skin, the thorax was gently sprayed with 75% ethanol and cleaned with a Kimwipe™. Acoustic gel was then applied in a small quantity to the thorax, and the ultrasound probe was lowered to view the midsagittal plane of the left ventricle. B-Mode imaging was used to locate and adjust the outflow tract until it was in-line with the focal point. Once the outflow tract was aligned in the long-axis (LAX) view, the probe was rotated 90° clockwise to observe the papillary muscles in the short-axis (SAX) view. Upon detection of

papillary muscles, the stage was adjusted to align them vertically to each other. Lastly, the heart was once again observed in LAX view and the outflow tract was re-aligned with the focal point. Images in B-Mode view were saved, and the diastolic dimension, systolic dimension and LV wall thickness was measured. Once the values were recorded, M-Mode analysis was conducted by placing a marker between the two widest points of the left ventricle to assess key cardiac parameters including ejection fraction, fractional shortening, cardiac output, and stroke volume. After the initial measurements were taken, M-Mode analysis was repeated five minutes later, and values attained from B-mode (systolic and diastolic dimension) were compared to M-Mode, ensuring the values coincided to the nearest 1/100 of a millimeter.

2.8 2-D Echocardiography: Strain Analysis

Images attained in B-Mode at a frame rate of 200 frames/second were stored and accessed for strain analysis. Briefly, the wall motion of the left-ventricle was synchronized with the peak QRS complex on the echocardiogram to notify the system of the precise timepoint of ventricular depolarization. Next, the LV trace software was utilized to trace out both endocardial and epicardial borders of the left ventricle. Once ~10 points were traced, computer-generated strain analysis was conducted along two separate axes of the heart: radial axes (center to outside of ventricle cavity) and longitudinal axes (apex to base) of the ventricle. Analysis was performed in a global manner, whereby the ventricle was divided into six separate segments consisting of anterior and posterior apex, mid, and base. Strain analysis was also utilized to assess time-to-peak (T2P) ratios, identifying the duration required for each segment to induce maximal strain.

2.9 Immunohistochemistry

2.9.1 Paraformaldehyde Heart Fixation

For immunohistochemistry, a 4% PFA solution was initially prepared in 1X PBS (w/v) and adjusted to a pH of 7.4 *via* addition of 1N NaOH and 10 N HCl in a drop-wise manner. Once the solutions were sterile filtered, a 50mL syringe was filled with 30 mL 4% PFA, while another syringe was filled with 10 mL of 1% KCl solution. Once the syringes were prepared and stored on ice, mice were safely transported to a closed container and anesthetized under 1.5-2% isoflurane, followed by an intraperitoneal injection of 1000 USP Heparin dissolved in 1X PBS. After a five-minute incubation, mice were continuously anesthetized with 1.5% isoflurane, and a deep incision was made below the diaphragm to reveal the heart as previously described *(Methods 2.4)*. The inferior cava was localized, carefully cut, and the left-ventricular apex of the heart was perfused continuously with 10 mL of 1% KCl until the heart was present in a state of permanent diastole. Next, 20-30 mL of 4% PFA solution was injected into the same opening at the left-ventricular apex and perfused until the lung cavity and liver were clear. Utilizing curved forceps, the heart was then carefully lifted and excised from the base prior to placement in a weighing boat with 1X PBS. Following two more sets of washes with 1X PBS, the heart was placed in a falcon tube with 15 mL 4% PFA, and rocked overnight at room temperature then transferred into a tube with 1X PBS for long-term storage at 4°C.

2.9.2 Paraffin Fixation, Four-Chamber Slicing, and Fibrotic Assessment

Hearts fixed with 4% PFA were sent to the Toronto Centre of Phenogenomics, where they were embedded in paraffin wax, sliced along the four-chamber view, sectioned into 5µm sections, and adhered onto microscope slides. Hematoxylin and eosin (HE) and Masson's trichrome (MT) staining was also conducted by the Toronto Centre of Phenogenomics, and unstained slides were returned for immunohistochemistry.

Fibrotic assessment was conducted *via* MT staining, whereby collagen was stained green, and muscle was stained red. Images of the heart chambers were taken in brightfield using the ZEISS 700 LSM microscope at the apex, base, left and right ventricular walls, and the mitral valve. Regions of interest (as demonstrated in the thesis) were recognized where greatest variation in MT staining was observable between the wild-type, heterozygous, and homozygous STX1A KO mice. Total area occupied by collagen was therefore subtracted from muscle and background regions lacking stain to determine total fibrotic area in a given visual field.

2.9.3 Immunohistochemistry and Wheat-Germ Agglutinin (WGA) Staining

Unstained slides received from the Toronto Centre of Phenogenomics were initially placed in a slide rack and subjected to three cycles of xylene washes for five minutes per wash. Next, slides were incubated in a 1:1 solution comprised xyele:100% ethanol for five minutes, followed by gradient washes of two 100% ethanol washes, a 95% ethanol wash, a 70% ethanol wash, and a 50% ethanol wash. Next, the slide rack was placed in a glass dish and carefully ran under ultrapure tap water for 10 minutes, preventing direct contact between the water and tissue sections. During the incubation, a pressure cooker was filled with water to ~1cm, and a plastic

container with 300 mL of 1X Antigen Retrieval Solution (10mM sodium citrate with 0.05% Tween 20 in MiliQ water, pH 6.0 with 10N HCl) was placed inside the pressure cooker and onto a hot plate. Once the antigen retrieval solution came to a rolling boil, the pressure cooker was opened, and the slide holder was carefully placed in the solution. After the samples were boiled for three-minutes, the slides were removed, placed in a glass dish and rinsed under ultrapure water for 10 minutes. The slides were then subjected to three 1X-TBST washes (2mM Tris base, 13.7 mM NaCl, 0.025% Triton X-100, pH 7.6 with 1N HCl) and blocked overnight in 1% BSA dissolved in 1X TBS-T (w/v) at 4°C. The following day, samples were once again washed in 1X TBS-T (3 x 5 minutes) and dried using Kimwipes^{TM}. Next, a PAP pen was utilized to draw a boundary around each heart section, followed by incubating the samples overnight at 4°C with primary-WGA antibody (1:200 dilution in 1% w/v of BSA in TBS-T). On the final day, the antibody was carefully pipetted off, slides were subjected to final set of 1X TBS-T washes (3 x 5 mins) and mounted with Fluoroshield mounting medium with DAPI with 1 mm cover slips. The samples were left to dry overnight and visualized the following day using the ZEISS LSM 700 confocal microscope.

2.10 Reverse Transcriptase-quantitative PCR (RT-qPCR)

2.10.1 RNA Isolation and Quantification

RT-qPCR was performed to assess for alterations in mRNA transcript levels of E-C coupling and hypertrophic genes, alongside confirm successful knockout of STX1A. Briefly, mice were injected with heparin and the heart was revealed under 2% isoflurane as previously demonstrated *(2.4)*. Next, curved forceps were utilized to lift the heart and excise it, followed by

placement in a petri-dish with ice-cold DNase/RNase free water. Upon three-cycles of washes, the left-ventricular free wall was carefully isolated, placed in a new dish with DNase/RNase free water, and cut into small pieces. All tissue homogenate was carefully transported into a 1.5mL Eppendorf tube, and 1mL of ice-cold TRIzol Reagent (Invitrogen, 15596026) was added. Next, samples were sonicated over ice in thirty-second intervals until the tissue was completely homogenized, and the samples were incubated at room temperature prior to addition of chloroform in a 1:5 ratio of total TRIzol volume. Next, the samples were shaken vigorously and incubated at room temperature for another five minutes, followed by centrifugation at 12'000 g for 15 minutes at 4°C. Upon centrifugation, the clear aqueous top layer was transported into a new Eppendorf tube, and 0.5mL of isopropanol was added. The samples were next incubated for 10 minutes at room temperature prior to centrifugation at 4°C (12'000 g for 10 minutes), and the supernatant was decanted revealing a white RNA pellet at the bottom of the tube. The RNA pellet was resuspended and dissolved in 0.5mL of 75% ethanol and centrifuged again at 7500 g for 5 minutes. Following centrifugation, the ethanol was decanted, the RNA pellet was air dried for 5 minutes and dissolved in 20µL of DNAse/RNAse free water heated. The RNA was quantified in duplicates utilizing the Nanodrop Spectrophotometer, with an A260/A280 of ~2 being considered pure for cDNA synthesis.

2.10.2 Complementary DNA (cDNA) Synthesis

cDNA synthesis was conducted in 20 µL reaction tubes, consisting of 2 µg of RNA, 1X reverse transcriptase (RT) buffer, 10x RT enzyme, and nuclease-free water using the High-Capacity RNA-to-cDNA kit (AppliedBiosystems, Cat# 4387406). Samples were placed in a

thermocycler for 60 minutes at 37°C, followed by a 5-minute incubation period at 95°C prior to long-term storage at 20°C.

2.10.3 Primer Efficiency and Quantitative RT-qPCR

All primers utilized in the study were designed using the Geneious™ software on exon-exon boundaries in order to prevent genomic DNA amplification. Primers were designed to have a length of ~17-28 base pairs with a 3' overhang, ~50% G-C content to ensure appropriate annealing of DNA polymerase to the primer sequence, alongside a similar melting-temperature of 50-55°C. Furthermore, primers were assessed for efficiency by ensuring a single melt-cure peak, no presence of genomic product on an agarose gel, and only primers optimized at an efficiency of ~90-110% were utilized in the current study.

To conduct primer optimization, template cDNA was initially diluted in UltraPure™ DNase/RNase-free water (Invitrogen, 10977015) at ratios 1:2, 1:4, 1:8, and 1:16, and primer efficiency was tested at concentrations of 0.2 μM, 0.5 μM, and 1 μM. For each respective dilution and concentration, a qPCR reaction was conducted using the StepOne Plus PCR System (Applied Biosystems, CA, USA) with SsoAdvanced Universal SYBR Green Supermix (Bio-Rad, Cat# 1725271). Thermocycler conditions were adjusted to have a standard cycling phase, where samples were ran at 95°C for 10 mins, 40 cycles of 95°C for 15s, and 60°C for 60s. Samples were next cycled through the melt-curve stage, where the temperature was raised from 60°C to 95°C in 0.3°C increments. qPCR reactions were ran in triplicates and plotted against a logarithmic cDNA standard, and the slope was used to calculate the primer efficiency. Only primer sets demonstrating an efficiency of ~90-110% were used in the current thesis. Quantitative RT-qPCR was next conducted at the same cyclic conditions using the StepOne Plus

PCR System (Applied Biosystems, CA, USA) with SsoAdvanced Universal SYBR Green Supermix (Bio-Rad, Cat# 1725271), and transcript levels were normalized to housekeeping *Gapdh* and *Actb* using the $2^{-\Delta\Delta Ct}$ method (Rao et. al, 2013).

2.11 Densitometry and Statistical Analysis

Densitometry analysis was conducted utilizing the ImageJ Software, and GraphPad Prism 7 was used to generate all respective figures. GraphPad Prism was also utilized for statistical analyses conducted for this thesis, including row-statistics, non-parametric one-way and two-way ANOVAs, and Tukey-comparison tests. A p value < 0.05 was determined to be significant.

Table 1: Primary and secondary antibodies utilizing in Western blotting, alongside their host species and respective dilutions.

	Host Species	Source, Catalog #	Dilution
Primary Antibodies			
Syntaxin-1A	Mouse monoclonal	Synaptic Systems, 110 011	1:1000
GAPDH	Mouse monoclonal	Abcam, ab8245	1:1000
Secondary Antibodies			
Goat-Anti Mouse	Goat polyclonal	LI-COR, 926-32210	1:10,000
Goat-Anti Rabbit	Goat polyclonal	LI-COR, 926-68071	1:10,000

Table 2: Genes studied in RT-qPCR alongside their forward and reverse primer sequences.

Gene	Forward Primer Sequence	Reverse Primer Sequence
Stx1a	ATGCGGGACTTACTCGGTT	TGTCCTTGGCCGTGCG
Stx4	TCAAGTGTGAGAGAGGTGCA	ATGTTATCCCCCTGCCTCAA
Cacna1c	CCTGGCCATGCAGCACTAT	GCTCCCAATGACGATGAGGA
Ryr2	CTGCTGAGAACTGACGATGTC	AAGCGAACCTTTATTCCTGCA
Slc8a1	AGTTGATGAGAGGGACCAAGAT	AGGACCTGGTAGTTGGCTAATT
Plb	AACAGAAAACTGCCCAGCTAA	ACCTGCTTCTGTCTTGGCT
Atp2a2	AGAGGATAGCAGAGATGGGCA	ATCCACCGTGTTCTTAAAGTCATAA
Myh6	GACCAGATTATCCAGGCTAACC	CCTGATGAATTTCCCAAAGCGG
Myh7	GAGAATGGCAAGACGGTGACT	TGGCCATGTCCTCGATCTT
ANP	GCTTCTTCCTCGTCTTGGCC	GGTGGTCTAGCAGGTTCTTGA
GAPDH	CGGTGTGAACGGATTTGGC	TGCCGTGAGTGGAGTCATACT
Actβ	CAGCCACTGTCGAGTCG	CCATGGCGAACTGGTGG

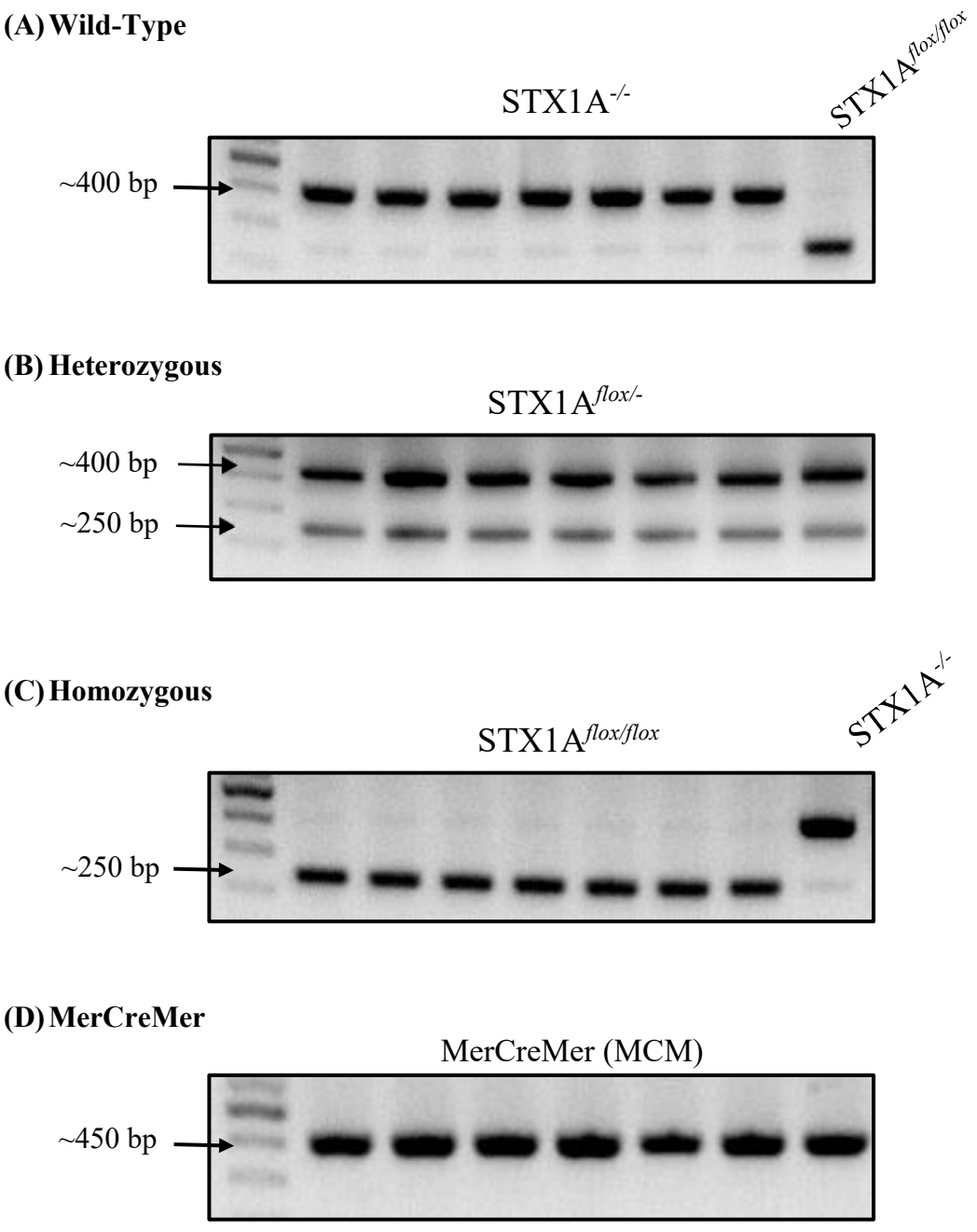

Figure 4: Mouse tail PCR genotyping confirming the generation of transgenic αMHC-MCM-STX1A$^{flox/flox}$ mice. **(A)** Wild-type mice lacking loxP sites demonstrated a single band at ~400bp**, (B)** heterozygous mice expressing loxP inserts on a single allele demonstrated two PCR products of ~400 base pairs and ~250 base pairs, and **(C)** homozygous mice expressing loxP sites on both alleles demonstrated a single band at ~250 base pairs. **(D)** The presence of MerCreMer under the MHC promoter was confirmed by a single PCR product at ~450 base pairs.

3.1 Confirming generation of transgenic STX1A$^{flox/flox}$ and MerCreMer mice

To specifically ablate STX1A in cardiomyocytes, two loxP sites were serially inserted into the STX1A locus at exons 2 and 3 *via* homologous recombination and provided by Dr. Molkentin (Methods, 2.1). To thereby confirm the presence of loxP in the transgenic mice, PCR genotyping was conducted on mouse tail samples acquired at 21 days using primers which spanned exons 2 and 3. Genotyping was also conducted for the tamoxifen-inducible Cre-recombinase gene (MerCreMer), responsible for inducing cardiomyocyte-specific excision of STX1A.

As predicted, wild-type mice lacking STX1A flox sites (STX1A$^{-/-}$) demonstrated a single PCR product at ~406 bp (Figure 4A), while mice expressing loxP sites on both alleles (STX1A$^{flox/flox}$) displayed a single product at ~250 bp (Figure 4B). Crossbreeding STX1A$^{-/-}$ and STX1A$^{flox/flox}$ mice yielded an F1 generation of heterozygous mice expressing loxP sites on a single allele (STX1A$^{flox/-}$), which was demonstrated by two PCR products; ~406 bp and ~250 bp (Figure 4C). All mice utilized in the study also expressed the MerCreMer gene, which is represented by a single product of ~450bp (Figure 4D). All results acquired from PCR genotyping were also consistent with previous findings from the Tsushima lab (Virdi , 2020; Virdi, 2022).

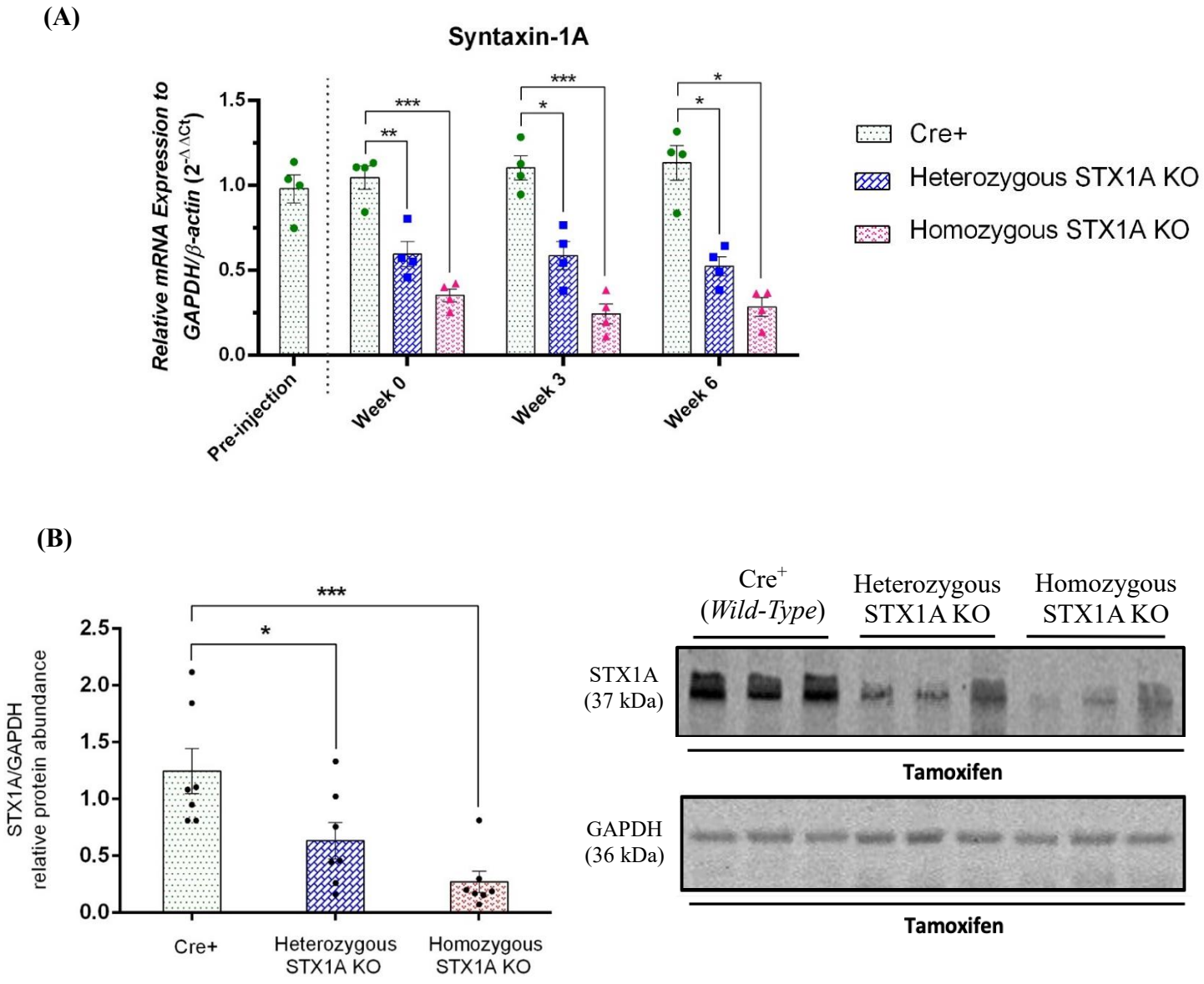

Figure 5: Confirming STX1A knockout in left-ventricular free-wall samples *via* RT-qPCR and Western blot analysis. **(A)** RT-qPCR demonstrated significant reduction in STX1A mRNA transcripts within both heterozygous and homozygous KO mice at week 0, week 3 and week 6, while mRNA levels continued to remain unchanged in Cre^+ control mice. Results were analyzed utilizing the $2^{-\Delta\Delta Ct}$ method, and mRNA levels were normalized to GAPDH and β-actin. **(B)** Western blotting of week 0 samples revealed significant reduction in STX1A protein expression within both heterozygous (-48%) and homozygous KO mice (-77%) when normalized to housekeeping GAPDH. All values are presented as mean ± SEM, with four replicates assessed for RT-qPCR analysis, and seven replicates for Western blot analysis. A two-way ANOVA and one-way ANOVA was performed for RT-qPCR and Western blot respectively, and $p < 0.05$ was deemed significant ($p<0.05$ = *; $p<0.005$ = **; $p<0.0005$ = ***; $p < 0.0001$ = ****).

3.2 Cre-mediated STX1A transcriptional and protein downregulation

Upon generation of STX1A$^{flox/flox}$ MerCreMer transgenic mice, tamoxifen was administered at 2-months of age to induce Cre-activation and drive cardiomyocyte-specific STX1A KO. Confirmation of STX1A KO was thereby assessed from a transcriptional and protein level approach *via* RT-qPCR and Western blotting; respectively (Figure 5).

Utilizing left-ventricular free-wall samples, mRNA transcript levels were initially assessed in Cre^{+} mice pre-injection (0.98 ± 0.08), with the results being comparable to that of post-injection treatment (1.05 ± 0.07), 3-weeks post-injection (1.10 ± 0.07) and 6-weeks post-injection (1.13 ± 0.1). As predicted, Cre^{+} mice lacking loxP sites demonstrated no significant changes in STX1A mRNA transcript levels, while heterozygous KO mice displayed a significant decline across week 0 (0.60 ± 0.07), week 3 (0.60 ± 0.08) and week 6 (0.53 ± 0.06) relative to Cre^{+}. Furthermore, RT-qPCR data also demonstrated a significant reduction in STX1A transcript levels in homozygous KO mice, displaying a 66% reduction at week 0 which further persisted into week 3 (78%) and week 6 (75%) relative to Cre^{+}. Western blot analysis of free-wall samples was also conducted to determine if downregulation in mRNA levels can be further reflective of STX1A protein expression. Post-tamoxifen treatment (week 0), both heterozygous KO mice (0.58 ± 0.05) and homozygous KO mice (0.26 ± 0.05) displayed a significant reduction in STX1A protein expression when compared to the Cre^{+} group (1.12 ± 0.09). Collectively, the results demonstrated efficient Cre-targeted KO of STX1A within LV free-wall cardiomyocytes which also coincided with previous laboratory immunohistological, RT-qPCR and Western blot analyses (Virdi, 2020; Virdi, 2022).

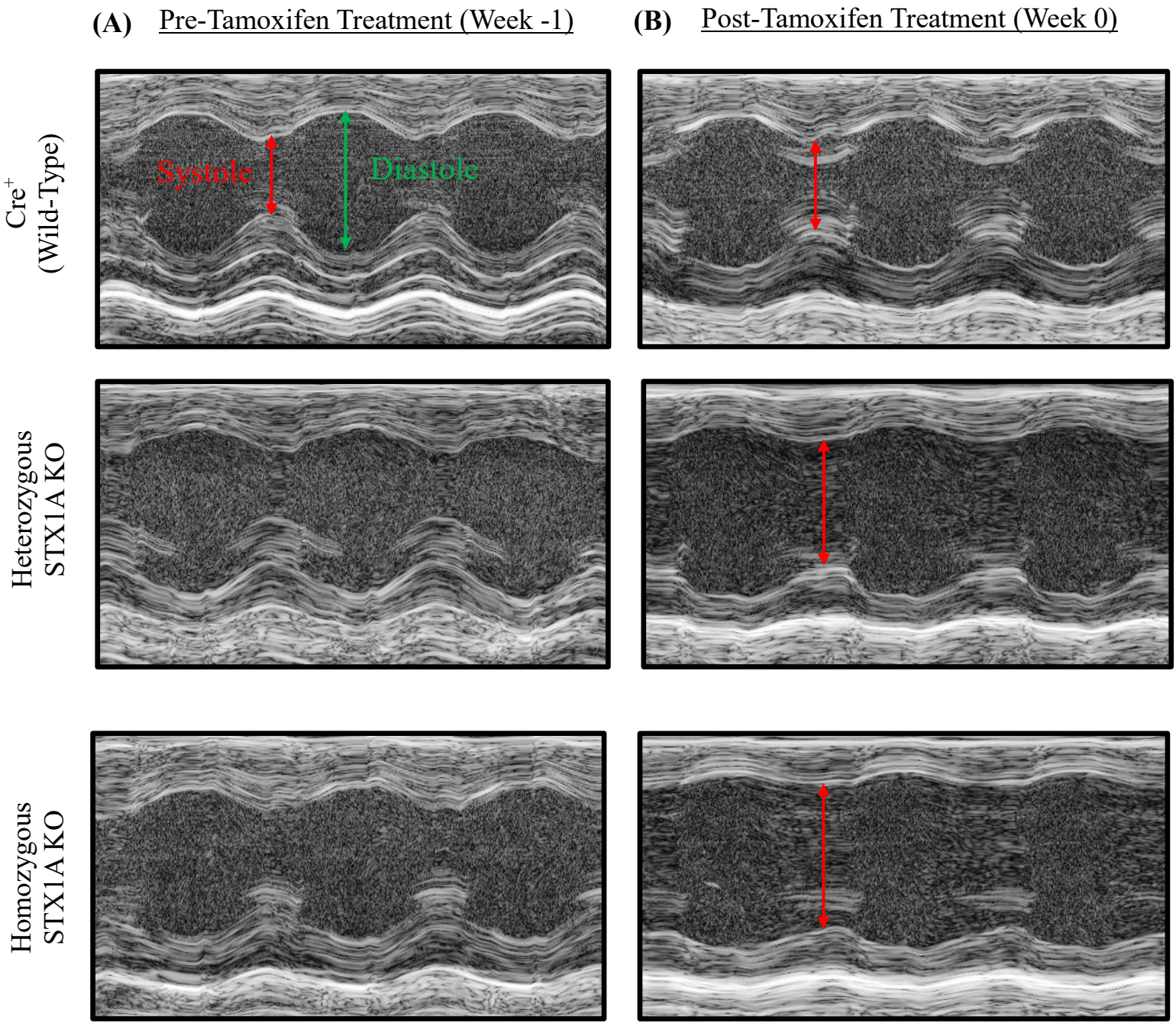

Figure 6: Effects of STX1A KO on ventricular wall motion as assessed through 2-D echocardiographic M-mode analysis. (A) Pre-tamoxifen treatment, the male Cre^{+}, heterozygous STX1A KO mice, and homozygous STX1A KO mice demonstrate basal systolic (red arrows) and diastolic function (green arrows). **(B)** Post-tamoxifen treatment, heterozygous and homozygous KO of STX1A elicits impaired systolic motion as represented by lengthening of red arrows. All echocardiographic analyses were performed utilizing the VisualSonics 2011 ultrasound imaging system across the mid-sagittal plane of the left ventricle.

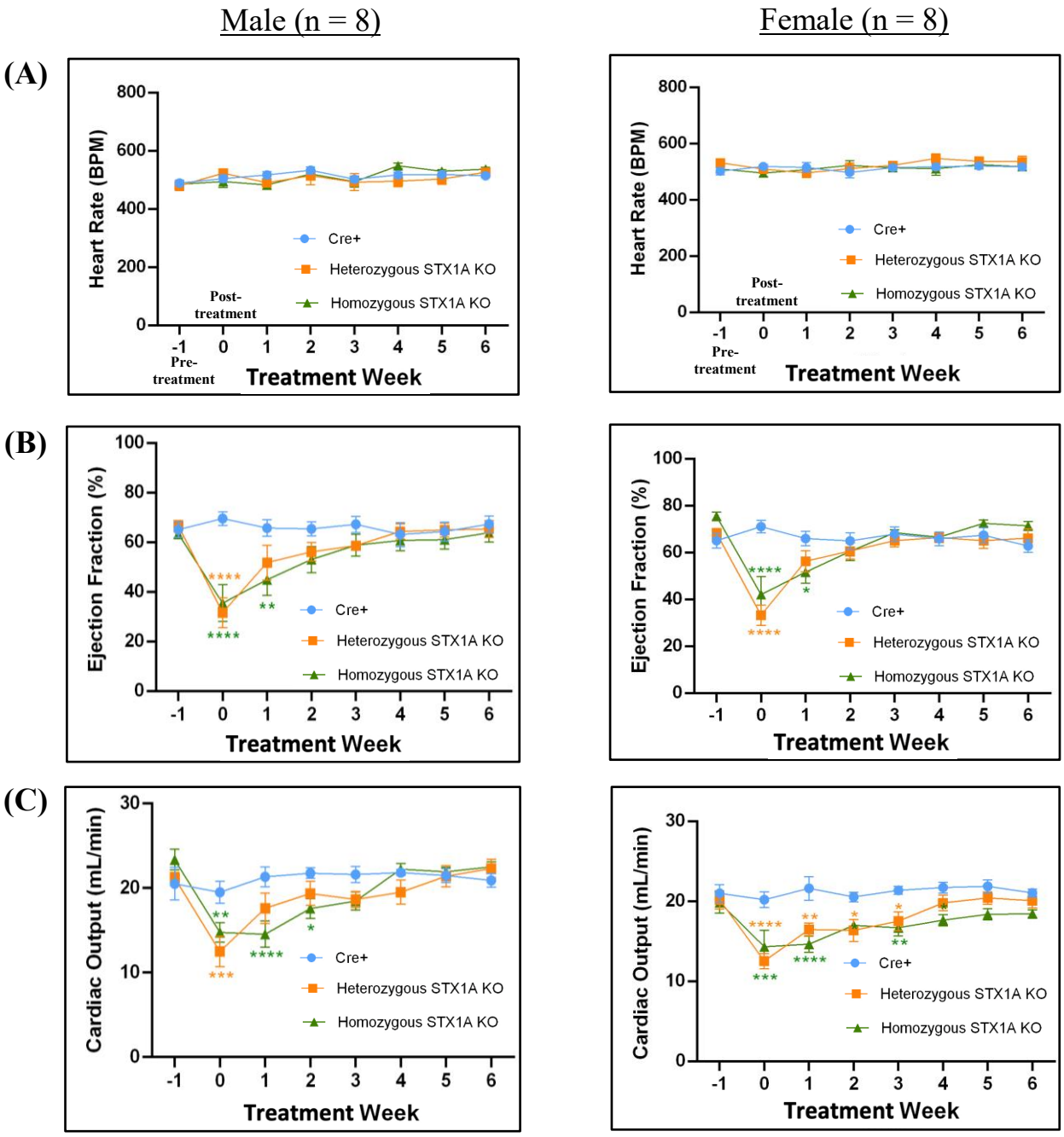

Figure 7: Functional analysis of left-ventricular wall motion assessed over eight-weeks within male and female Cre$^+$ and STX1A KO mice. (A) No alterations in heart rate (BPM) was recorded throughout the course of the study amongst control and experimental groups, while **(B)** ejection fraction (%) and **(C)** cardiac output (mL/min) was significantly reduced in heterozygous and homozygous KO mice post-tamoxifen treatment. Transient decline in contractile function was observed amongst both male and female mice, while no significant alterations were reported in the Cre$^+$ group. All values are presented as mean ± SEM, with eight replicates per group, and a two-way ANOVA was performed for statistical analysis with $p < 0.05$ being deemed significant ($p<0.05$ = *; $p<0.005$ = **; $p<0.0005$ = ***; $p < 0.0001$ = ****).

Table 3: Summary of cardiac parameters assessed *via* ventricular M-mode analysis on Cre$^+$ and STX1A KO male mice at week -1, week 0, and week 3. Results demonstrate baseline function amongst Cre$^+$ and KO mice pre-injection, while a significant reduction in contractile function is observed post-treatment in heterozygous and homozygous KO mice (green = increase in cardiac parameter relative to Cre$^+$, red = decrease). By week 3, an overall return in function is observed, while decreased stroke volume persists in homozygous KO mice. All values are presented as mean ± SEM, with eight replicates per group. A two-way ANOVA was performed for statistical analysis, and $p < 0.05$ was deemed significant ($p<0.05$ = *; $p<0.005$ = **; $p<0.0005$ = ***; $p < 0.0001$ = #). *HR = heart rate; LVEDs and LVEDd = LV end-systolic and diastolic dimensions; LVEVs and LVEVd = LV-end systolic and diastolic dimensions), SV = stroke volume; EF = ejection fraction; FS = fractional shortening; CO = cardiac output*.

MALE	Pre-injection (Week -1)			Post-injection (Week 0)			Post-injection (Week 3)		
	Cre$^+$	Heterozygous STX1A KO	Homozygous STX1A KO	Cre$^+$	Heterozygous STX1A KO	Homozygous STX1A KO	Cre$^+$	Heterozygous STX1A KO	Homozygous STX1A KO
HR (BPM)	489 ± 10	480 ± 16	485 ± 10	504 ± 14	523 ± 11	494 ± 20	502 ± 12	493 ± 26	494 ± 18
LVED$_s$ (mm)	2.5 ± 0.1	2.6 ± 0.2	2.6 ± 0.1	2.4 ± 0.1	3.7 ± 0.2$^{\#}$	3.9 ± 0.3$^{\#}$	2.5 ± 0.2	2.8 ± 0.1	2.8 ± 0.2
LVED$_d$ (mm)	3.9 ± 0.1	3.9 ± 0.1	4.1 ± 0.1	3.8 ± 0.1	4.3 ± 0.1*	4.6 ± 0.2$^{\#}$	3.9 ± 0.1	3.8 ± 0.1	3.8 ± 0.1
LVEV$_s$ (µL)	25.6 ± 3.8	22.9 ± 2.6	27.0 ± 2.8	21.2 ± 3.4	57.9 ± 7.1$^{\#}$	70.8 ± 13.3$^{\#}$	23.0 ± 3.2	26.7 ± 2.2	26.9 ± 3.9
LVEV$_d$ (µL)	71.5 ± 5.6	67.3 ± 3.7	76.9 ± 4.6	61.5 ± 13	85.7 ± 6.2**	98.2 ± 12.6$^{\#}$	68.3 ± 3.4	63.9 ± 3.4	64.5 ± 3.4
SV (uL)	45.9 ± 2.8	44.4 ± 1.5	49.9 ± 2.7	40.3 ± 2.0	27.8 ± 5.1$^{\#}$	27.4 ± 4.1$^{\#}$	45.3 ± 1.9	37.2 ± 1.9	37.6 ± 0.7*
EF (%)	64.2 ± 3.0	66.0 ± 2.0	64.9 ± 1.8	65.5 ± 2.8	32..4 ± 5.5$^{\#}$	27.9 ± 7.4$^{\#}$	66.3 ± 3.3	58.2 ± 1.5	58.3 ± 3.7
FS (%)	35.6 ± 2.2	33.3 ± 1.8	36.6 ± 1.8	36.8 ± 2.2	14.0 ± 3.0$^{\#}$	15.2 ± 33$^{\#}$	35.9 ± 2.2	26.3 ± 1.1	26.3 ± 2.4
CO (mL/min)	22.4 ± 1.9	21.3 ± 0.6	24.2 ± 1.0	20.3 ± 1.3	14.5 ± 2.9***	13.5 ± 1.2***	22.7 ± 0.9	18.3 ± 0.6	18.6 ± 1.0

Table 4: Summary of cardiac parameters assessed *via* ventricular M-mode analysis on Cre$^+$ and STX1A KO female mice at week -1, week 0, and week 3. Cardiac function is maintained between Cre$^+$ and KO mice pre-tamoxifen treatment, while significantly reduced post-treatment in heterozygous and homozygous KO mice only. Female KO mice began to demonstrate recovery by week 1, and showed full recovery in systolic function by week 3.
All values are presented as mean ± SEM, with eight replicates per group. A two-way ANOVA was performed for statistical analysis, and $p < 0.05$ was deemed significant ($p<0.05$ = *; $p<0.005$ = **; $p<0.0005$ = ***; $p < 0.0001$ = #). *HR = heart rate; LVEDs and LVEDd = LV end-systolic and diastolic dimensions; LVEVs and LVEVd = LV-end systolic and diastolic dimensions), SV = stroke volume; EF = ejection fraction; FS = fractional shortening; CO = cardiac output*.

FEMALE	Pre-injection (Week -1)			Post-injection (Week 0)			Post-injection (Week 3)		
	Cre$^+$	Heterozygous STX1A KO	Homozygous STX1A KO	Cre$^+$	Heterozygous STX1A KO	Homozygous STX1A KO	Cre$^+$	Heterozygous STX1A KO	Homozygous STX1A KO
HR (BPM)	501 ± 13	532 ± 13	509 ± 7	518 ± 8	509 ± 4	495 ± 13	514 ± 10	523 ± 14	514 ± 14
LVED$_s$ (mm)	2.6 ± 0.1	2.2 ± 0.2	2.2 ± 0.1	2.4 ± 0.2	3.6 ± 0.2$^{\#}$	3.3 ± 0.3$^{\#}$	2.4 ± 0.1	2.3 ± 0.1	2.2 ± 0.1
LVED$_d$ (mm)	3.9 ± 0.1	3.6 ± 0.2	3.5 ± 0.1	3.8 ± 0.2	4.2 ± 0.1**	4.1 ± 0.1*	3.9 ± 0.1	3.5 ± 0.1	3.4 ± 0.1
LVEV$_s$ (µL)	24.5 ± 2.9	25.0 ± 2.2	25.5 ± 1.5	17.8 ± 2.7	46.1 ± 8.5$^{\#}$	44.1 ± 8.7$^{\#}$	21.1 ± 2.9	18.1 ± 2.0	15.4 ± 1.4
LVEV$_d$ (µL)	68.2 ± 3.8	62.9 ± 6	60.5 ± 3.6	59.4 ± 4.9	80.7 ± 4.5**	76.2 ± 5.9**	66.5 ± 3.8	59.3 ± 4.5	59.5 ± 2.6
SV (uL)	43.7 ± 3	37.9 ± 3.2	35.0 ± 2.1	41.6 ± 2.4	34.6 ± 2.3$^{\#}$	32.1 ± 3.8$^{\#}$	44.1 ± 2.1	41.2 ± 3.1	44.1 ± 1.7
EF (%)	64.1 ± 3.1	60.3 ± 2.1	57.9 ± 1.9	70.0 ± 2.7	42.9 ± 4.3$^{\#}$	42.1 ± 6.8$^{\#}$	68.1 ± 3	69.5 ± 2.6	74.1± 1.4
FS (%)	33.3 ± 2.3	38.9 ± 1.6	37.1 ± 1.6	36.8 ± 4.5	14.3 ± 2.3$^{\#}$	19.5 ± 4.2$^{\#}$	38.5 ± 2.4	34.3 ± 1.9	35.3 ± 1.1
CO (mL/min)	21.9 ± 1.1	19.8 ± 1.1	17.8 ± 1.3	21.5 ± 1.1	17.6 ± 1.1$^{\#}$	15.9 ± 2***	23.3 ± 1.4	21.5 ± 1.3	22.7 ± 1.0

3.3 Cardiomyocyte-specific STX1A KO causes transient systolic dysfunction

The effects of STX1A KO were assessed through *in vivo* 2-D echocardiography in Cre^+, heterozygous and homozygous male and female STX1A KO mice over a course of eight-weeks; from pre-tamoxifen treatment (week -1) to six weeks post-tamoxifen (week 6). Upon treatment at 40 mg/kg intraperitoneally over four-days, the fifth day marked completion and is considered as the timepoint "week 0". Throughout the course of eight-weeks, all three male groups demonstrated a consistent heart rate (beats per minute – BPM) with no significant alteration across any time point (Figure 7A). Furthermore, baseline recordings acquired at week -1 (Cre^+ = 490 ± 10 BPM; Heterozygous KO = 480 ± 16 BPM; Homozygous KO = 485 ± 10 BPM) correlated with the findings by Virdi (2020) who demonstrated a mean HR of 481 ± 31 BPM in tamoxifen-treated male mice, and 445 ± 10 BPM in Cre^+ male mice. Similar results were acquired in female mice as well, whereby no significant alteration in the basal heart rate was observed in the heterozygous (530 ± 13 BPM) and homozygous KO groups (510 ± 7 BPM) relative to Cre^+ mice (501 ± 13 BPM). The findings are also comparable to published studies utilizing 1.5-2% isoflurane anesthetic for murine echocardiographic analyses, with HR being recorded between 400 – 530 BPM (Schnelle et al., 2018; Low et al., 2015; Wu et al., 2010).

Consistency in mean HR recordings allowed for assessment of secondary parameters including the ejection fraction (EF – %), defined by the percentage of blood leaving the heart per cardiac cycle. The baseline EF recorded pre-tamoxifen treatment within Cre^+ males (65 ± 3%) correlated with heterozygous (68 ± 2%) and homozygous KO mice (77 ± 9%) with no statistical difference (Figure 7B). Moreover, female Cre^+ mice (64 ± 3%), heterozygous (67 ± 2%) and homozygous (65 ± 2%) KO groups demonstrated no significant differences at week -1, and all baseline EF values fell into range of normal systolic function (67 ± 1%; Russo et al., 2019)

(60 ± 8%; Vinhas et al., 2013). Post-tamoxifen treatment however, a significant reduction in EF was noted, with a decline of 53% recorded within both male and female heterozygous STX1A KO groups. At the same time, homozygous KO of STX1A elicited a 48% reduction within male mice, while female mice demonstrated a 43% decrease (Figure 7B; Table 3, 4). Reduced EF induced by STX1A-KO is consistent with findings of previous laboratory studies (Virdi, 2020), where a decrease from 68 ± 2% to 42 ± 6% was noted within homozygous KO male mice. Moreover, both heterozygous and homozygous KO of STX1A induced phenotypical changes to the left ventricle as well, eliciting decreased contractility which was accompanied by an elevation in end-systolic diameter (Figure 7; Table 3, 4). Concurrent preservation of ejection fraction and LV wall function within Cre^+ mice is consistent with the findings by Virdi (2020, 2022), thereby suggesting the effects to be STX1A KO specific (Table 3, 4).

Alongside a reduction in EF, echocardiographic analyses revealed a significant decline in the stroke volume (SV), fractional shortening (FS), and cardiac output (CO) within heterozygous and homozygous STX1A KO mice at week 0 (Figure 7C; Table 3, 4). A reduction in contractile function of the left ventricle persisted for three weeks, with homozygous males continuingly demonstrating significant decline in SV (36.03 ± 0.7μL) relative to Cre^+ mice (45.3 ± 1.9μL). Similar results were also observed for homozygous female KO mice at week 3, displaying a significant reduction (32.8 ± 1.7μL) when compared to Cre^+ mice (44.1 ± 2.1μL). Intriguingly, the left-ventricle demonstrated recovery in contractile function by week 4, with no significant differences recorded in the contractile parameters (SV, EF, FS, CO), alongside a return in end-systolic and diastolic dimensions and volumes (Figure 7). More specifically, EF improved to 64 ± 3% and 66 ± 2% within male and female heterozygous KO mice respectively, and 61 ± 4% and 67 ± 2% in homozygous male and female STX1A KO mice respectively by week 4.

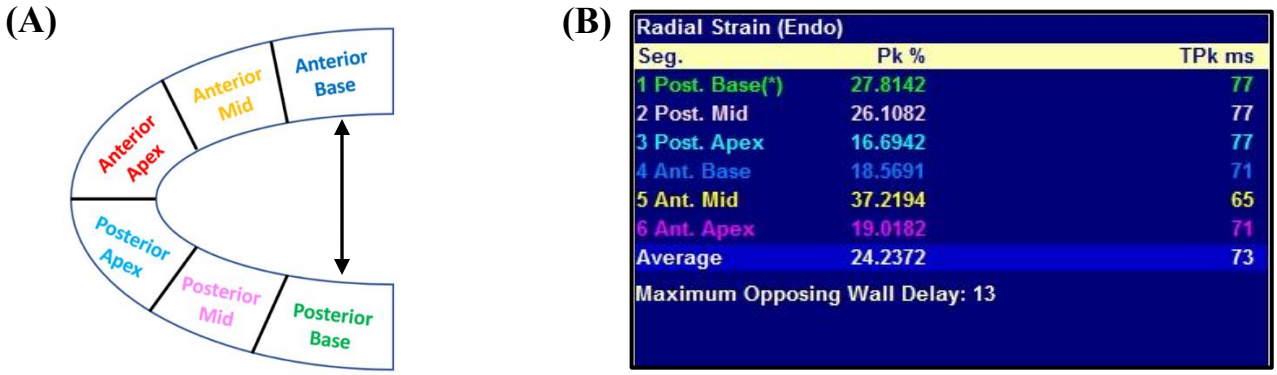

Figure 8: Schematic representation of speckle-tracking strain-analysis performed along the parasternal long-axis. (A) By utilizing the LV trace tool, speckle-tracking divides the ventricular chamber into six-separate segments – anterior and posterior apex, mid, and base – and individually monitors the change in ventricular wall motion across each segment. Black arrow represents the radial axis along which strain recordings were conducted. **(B)** Representative image of radial strain acquired across each LV segment, demonstrating peak-radial strain (Pk%) and time required to reach the peak strain value (TPk ms).

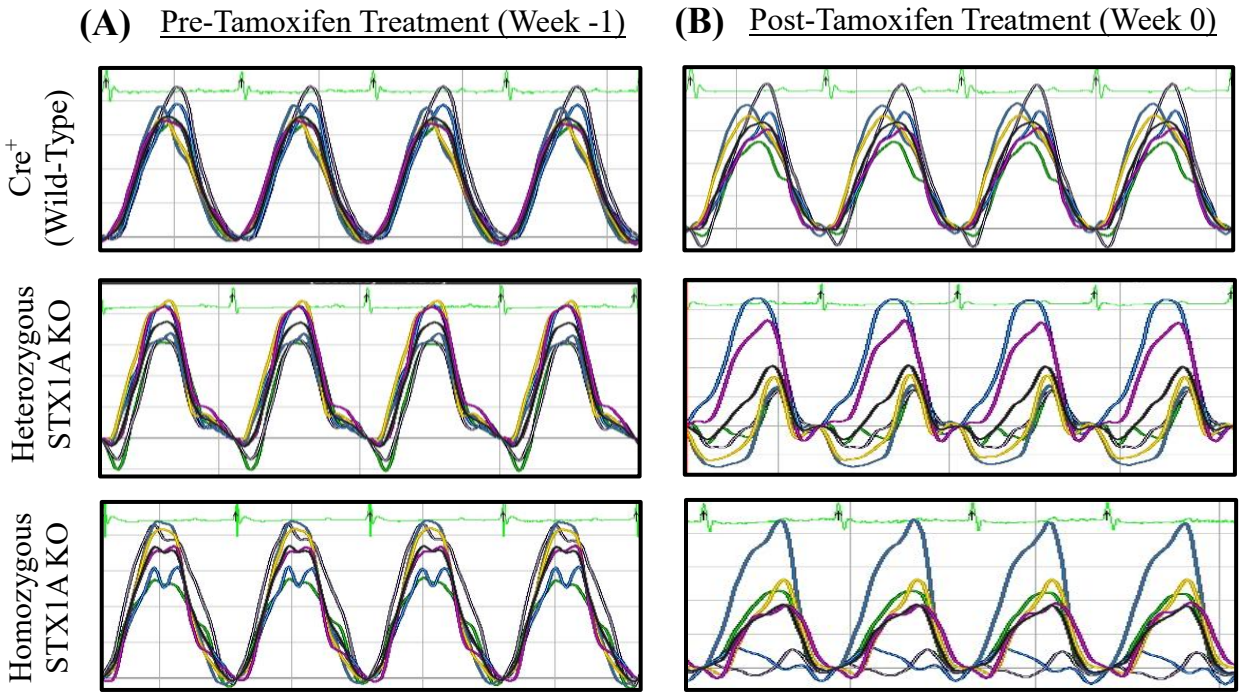

Figure 9: Representative images of strain-analysis conducted on pre-tamoxifen and post-tamoxifen treated Cre$^+$, heterozygous, and homozygous STX1A KO mice. X-axis represents the time required to reach peak strain, while y-axis represents the Pk% across each segment. **(A)** Pre-tamoxifen treatment, Cre$^+$ and STX1A KO mice demonstrate synchronicity in electrical (TPk) and mechanical strain across each segment. **(B)** Post-tamoxifen administration, segmental dyssynchrony is observed in both TPk and Pk% within heterozygous and homozygous STX1A KO mice, while radial strain is maintained in Cre$^+$ mice (n = 6).

(A) Mechanical Function (Pk %)

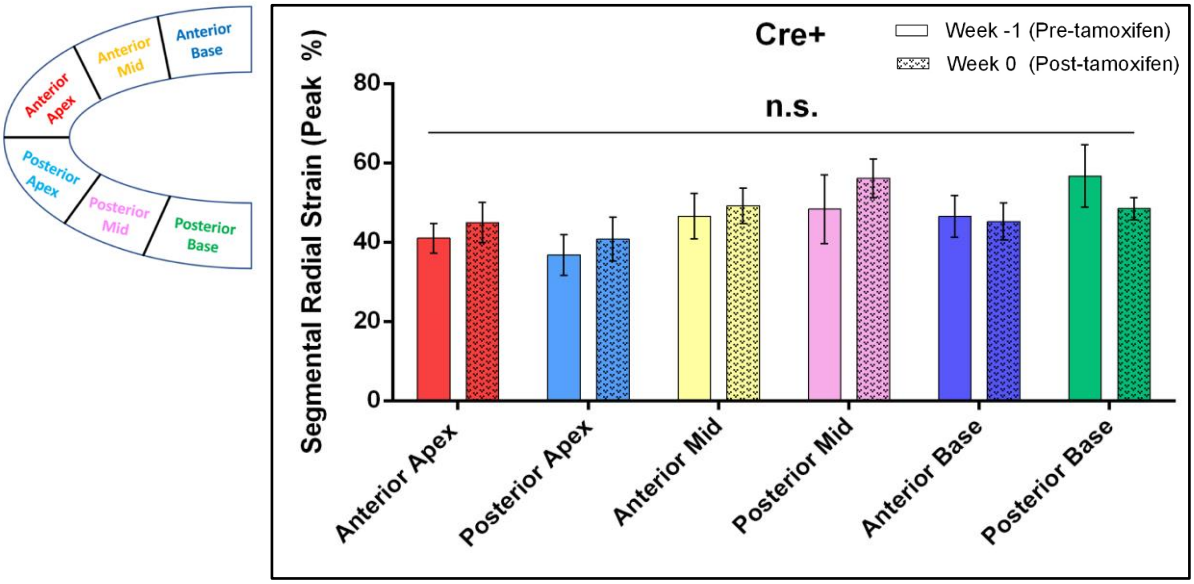

(B) Electrical Function (TPk ms)

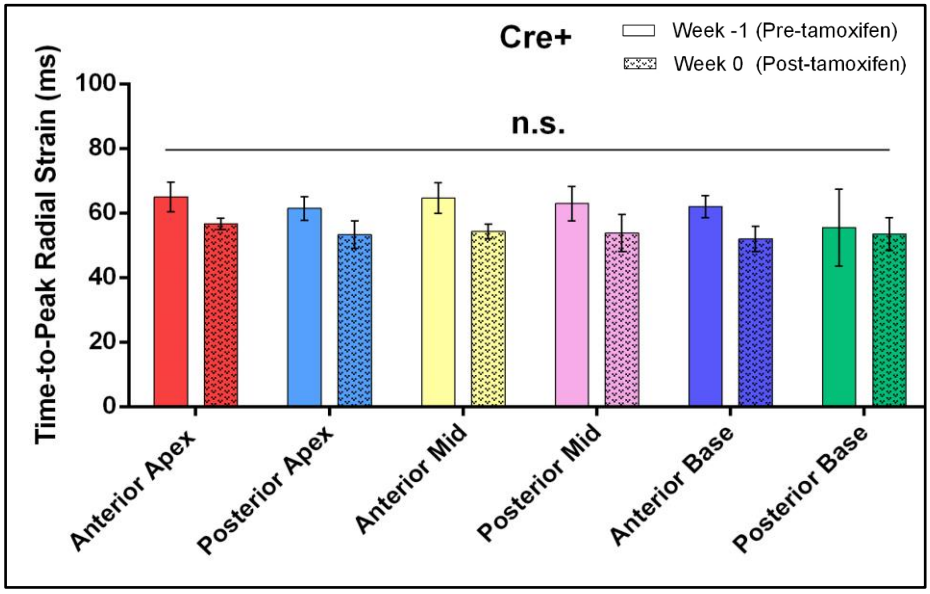

Figure 10: Assessment of peak-radial strain (Pk %) and time-to-peak (TPk ms) along the radial axis in Cre$^+$ mice along the apical, mid and basal regions. Pre-tamoxifen results are represented as solid bars, while post-tamoxifen results are demonstrated as patterned bars. **(A)** Administration of tamoxifen demonstrated no significant alteration in peak-radial strain generated across the left-ventricular myocardium. **(B)** No significant alteration in time-to-peak analysis is also observed in the anterior and posterior apical, mid and basal regions of the LV in Cre$^+$ mice. All values are plotted as mean ± SEM, with a sample size of n = 6. GraphPad Prism was utilized to perform a one-way ANOVA test for statistical analysis, and a p-value > 0.05 was considered as not significant (n.s.).

(A) Mechanical Function (Pk %)

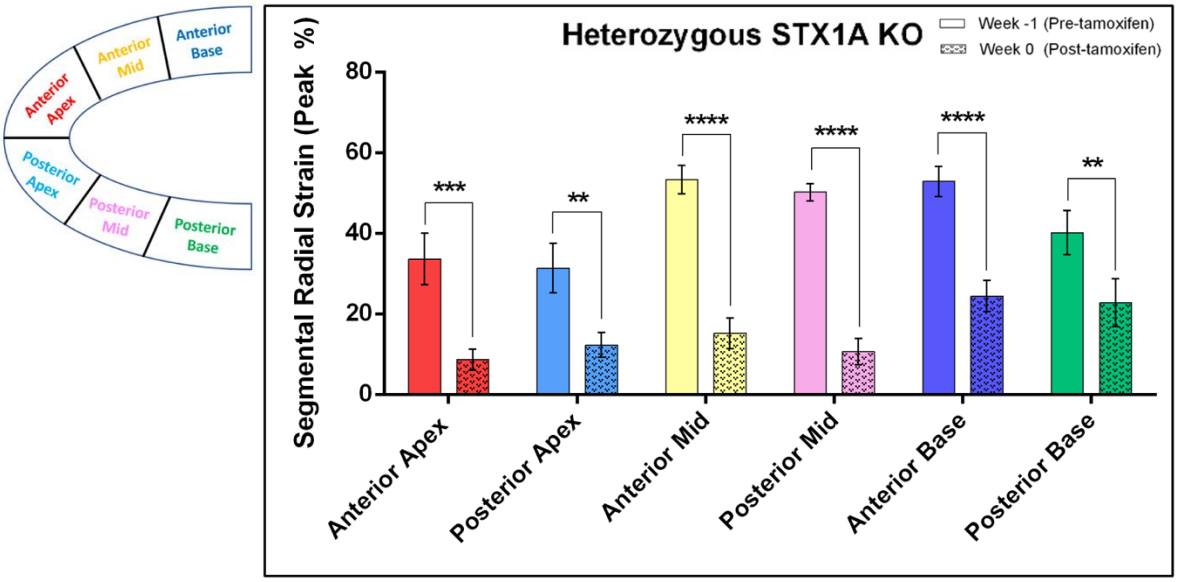

(B) Electrical Function (TPk ms)

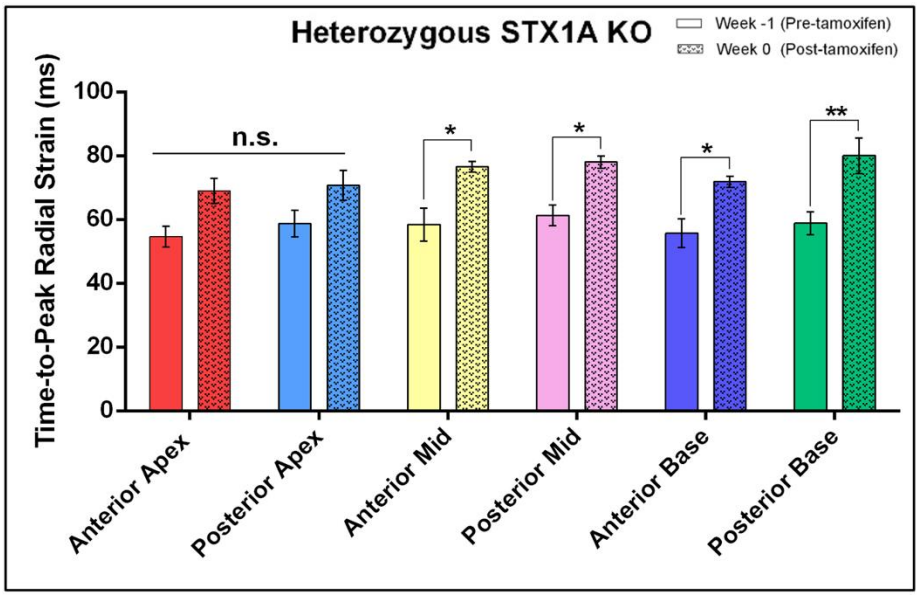

Figure 11: Assessment of peak-radial strain (Pk %) and time-to-peak (TPk ms) analysis along the radial axis in heterozygous STX1A KO mice along the apical, mid and basal regions. (A) Heterozygous KO of STX1A elicited significant reduction in Pk% across the left-ventricular myocardium. **(B)** Significant delays in electrical signal propagation are also observed at the mid and basal regions, while no significant delays in TPk are recorded at the apical segments. All values are plotted as mean ± SEM, with a sample size of n = 6. GraphPad Prism was utilized to perform a one-way ANOVA test for statistical analysis ($p<0.05$ = *; $p<0.005$ = **; $p<0.0005$ = ***; $p < 0.0001$ = ****).

(A) Mechanical Function (Pk %)

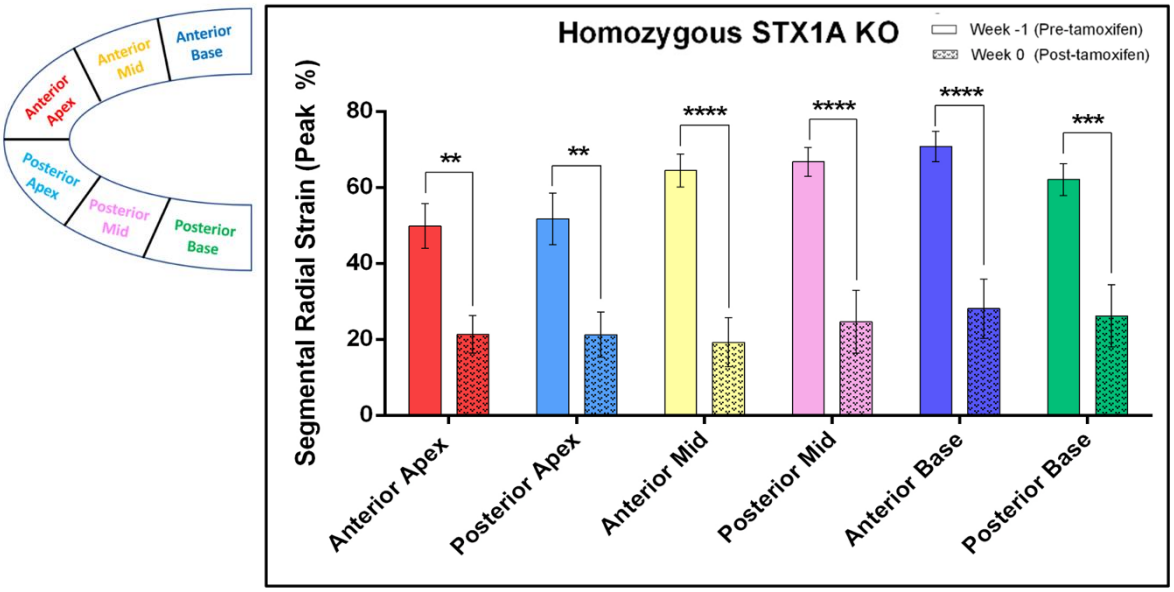

(B) Electrical Function (TPk ms)

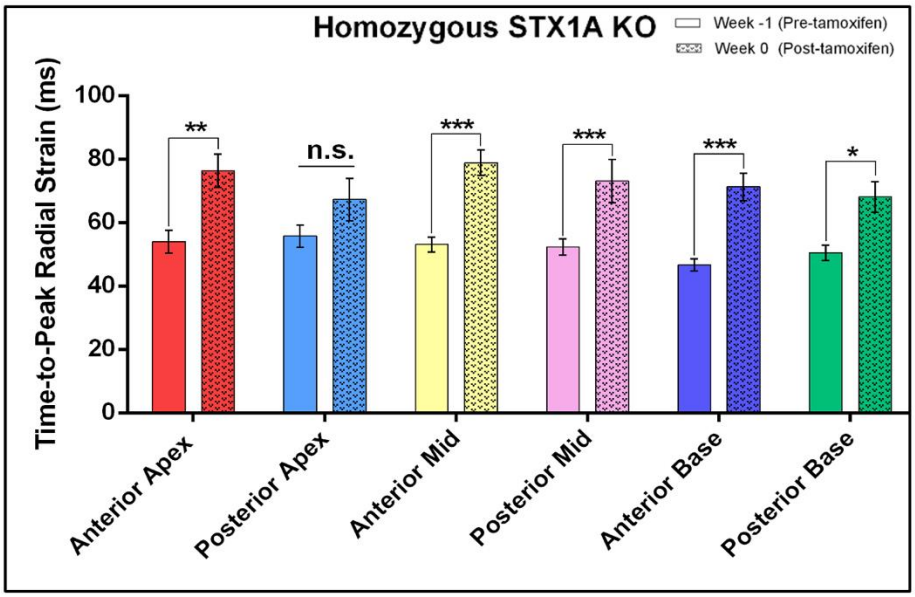

Figure 12: Assessment of peak-radial strain (Pk %) and time-to-peak (TPk ms) analysis along the radial axis in homozygous STX1A KO mice along the apical, mid and basal regions. (A) Post-tamoxifen treatment, homozygous KO of STX1A elicited global mechanical dysfunction of the ventricle along the radial axis. **(B)** Homozygous KO of STX1A also triggers electrical delays at the mid and basal regions of the LV, and a significant delay in electrical propagation at the anterior apex. All values are plotted as mean ± SEM, with a sample size of n = 6. GraphPad Prism was utilized to perform a one-way ANOVA test for statistical analysis ($p<0.05$ = *; $p<0.005$ = **; $p<0.0005$ = ***; $p < 0.0001$ = ****).

3.4 Speckle-tracking reveals global electromechanical dysfunction of the LV

Conventional 2-D M-mode analysis demonstrated transient dysfunction of the left ventricle *via* reduction in EF, SV, FS and CO which persisted for three weeks prior to recovery. To further validify a decrease in LV function induced by STX1A KO, speckle-tracking was performed along the parasternal long-axis view to determine temporal or global LV dysfunction, alongside assess for electromechanical disruptions induced by STX1A KO.

Speckle-tracking allowed for successful division of the LV chamber into six separate segments: anterior and posterior apex, mid, and basal regions which were assessed individually for electromechanical function (Figure 8). Pre-tamoxifen treatment, Cre^+, heterozygous and homozygous KO demonstrated both electrical and mechanical synchronicity, as represented by coordinated depolarization and sustained peak contractile strain of the ventricle (Figure 9). Amongst the three segments, the apical region demonstrated the lowest strain within Cre^+ (39 ± 4%), heterozygous (33 ± 6%) and homozygous KO mice (51 ± 6%) which coincided with published findings (39 ± 5%, Rea et al., 2016; 50 ± 1%, Ram et al., 2011). To add, the ventricular base demonstrated greater strain than the apex (Cre^+ = 48 ± 7%; heterozygous KO = 47 ± 5%; homozygous KO = 65 ± 4%), and mid-region demonstrated the highest strain (Cre^+ = 52 ± 7%; heterozygous KO = 52 ± 3%; homozygous KO = 66 ± 4%). The baseline studies thereby elucidate the apical region of the LV chamber to have the lowest radial strain followed by basal and mid-region of the ventricle. These findings coincide with the global contractile pattern of the ventricle along the radial axis, and are supported by previously established strain analysis results in response to isoproterenol administration (Andrews et al., 2014; Walsh-Wilkinson, Arsenault and Couet, 2021).

Consistent with M-mode analysis post-tamoxifen treatment, Cre^{+} mice did not demonstrate any significant changes in contractile function across the apical, mid, and basal regions of the left-ventricle (Figure 9, 10A). Opposingly, heterozygous STX1A KO elicited significant decline in radial strain throughout the ventricular chamber, reducing apical strain by 68 ± 5%, basal strain by 50 ± 5%, and mid-regional strain by 75 ± 3% (Figure 11A*)*. Moreover, homozygous KO of STX1A also demonstrated global dysfunction of the LV, causing a 58 ± 6% decline in apical strain, 59 ± 6% decline in basal strain, and 67 ± 6% decline in mid-regional strain (Figure 12A*)*. The results demonstrate an equal or greater than 50% reduction in radial contractile function induced by STX1A KO, and such severe reduction in ventricular strain has been reported 20-days post-transaortic banding (Peng et al., 2009). Collectively, the reduction in ventricular strain coincides with the impaired EF and CO recorded *via* M-mode echocardiography, confirming global dysfunction of the LV induced by STX1A haploinsufficiency. Moreover, STX1A KO significantly reduced the peak contractile strain throughout the anterior and posterior ventricular wall as well, thereby not demonstrating regional bias in reduced functionality (Figure 11A, 12A).

Alongside mechanical dysfunction of the ventricle, time-to-peak (T2P) analysis of the LV revealed evident dyssynchrony in segmental shortening induced by heterozygous and homozygous STX1A KO. Amongst both groups, segmental dyssynchrony was significant at the mid and basal regions of the LV, as heterozygous KO elicited a 17 ± 3ms delay in the mid-segmental region, while homozygous KO caused a 23 ± 4ms electrical delay. Moreover, abnormality in electrical signal propagation is also observed at the basal regions of the ventricle, with an 19 ± 3ms delay in heterozygous KO mice and 21 ± 3ms delay in homozygous KO mice. Intriguingly, heterozygous KO did not induce significant electrical delays at the apical chambers

of the LV chamber (Figure 11B), while homozygous KO induced dyssynchrony of the anterior apex specifically (Figure 12B) No alteration in T2P measurements within Cre^{+} mice elucidates electrical synchronicity of the ventricle, and thereby maintained electromechanical function post-tamoxifen treatment (Figure 10).

(A) Male (n = 6)

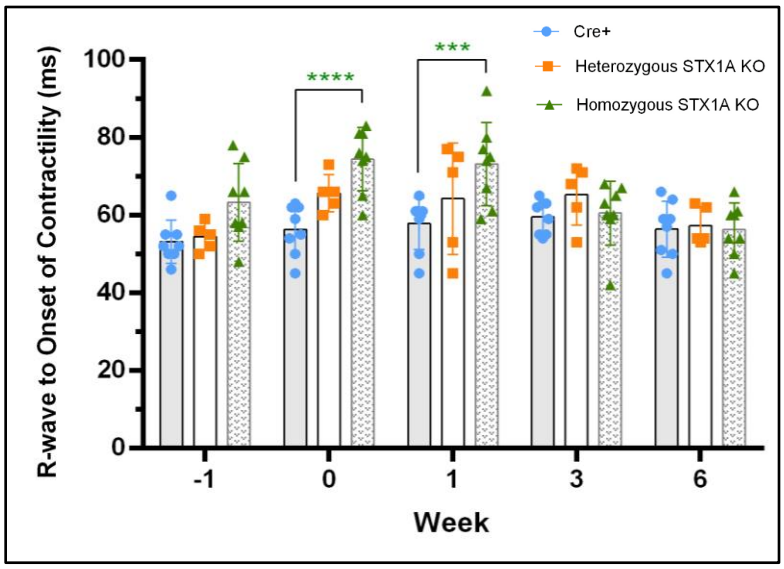

(B) Female (n = 6)

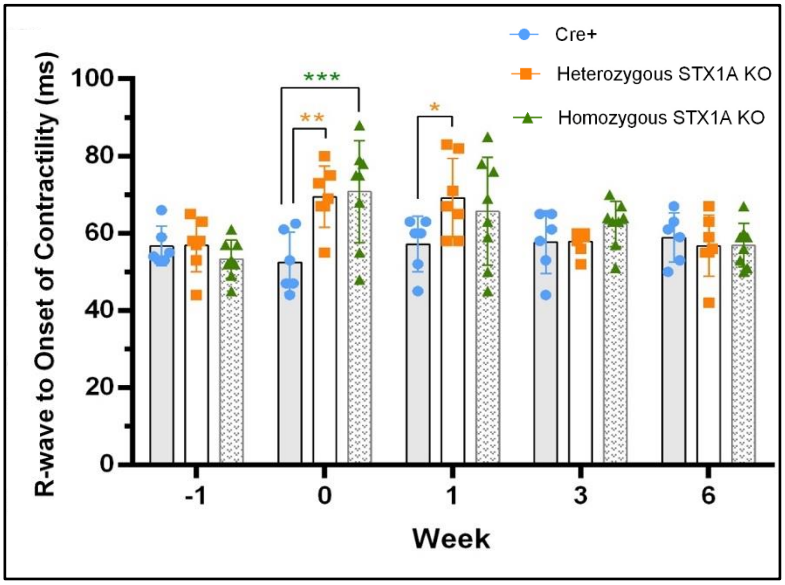

Figure 13: Global delay between the period of ventricular depolarization (R-wave) and onset of contraction recorded through strain-analysis. (A) Heterozygous and homozygous KO of STX1A elicited a significant delay in R-wave and contractility at week 0 and 1, while no significant changes were observed in Cre^{+} male mice. **(B)** Female mice also demonstrated significant electrochemical delays in heterozygous and homozygous KO mice at week 0, which was only persistent in homozygous KO mice at week 1. The values are graphed are represented as mean ± SEM, and a two-way ANOVA test was performed for statistical analysis ($p<0.05$ = *; $p<0.005$ = **; $p<0.0005$ = ***; $p < 0.0001$ = #).

3.5 Delay between R-wave and onset of contraction in male and female mice

Segmental analyses of the LV revealed desynchronized electrical stimulation at the mid and basal regions of the heart post-KO, alongside anterior apical dyssynchrony in homozygous KO mice (Figure 11, 12). To determine if segmental dyssynchrony induced a global electrical delay across the myocardium, time duration between the peak R-wave (period of ventricular depolarization, represented as the largest portion of the QRS complex) and ventricular contraction was assessed. As reported, the QRS complex within the electrocardiogram (ECG) occupies a relatively short period to ensure complete and rapid depolarization of the ventricle, with the normal R-wave timing being <50ms in a twelve-lead ECG (Klabunde, 2002; Pérez-Riera et.al, 2016). Based on T2P strain analysis conducted on Cre^+ mice, the mean duration from peak R-wave to ventricular contractility was 53 ± 3 ms within male mice, and 57 ± 2 ms in female mice pre-injection. Moreover, no significant alterations were recorded in male (54 ± 3 ms) or female Cre^+ mice (52 ± 3 ms) at week 0, which persisted into week 1, and three- and six-weeks post-tamoxifen treatment (Figure 13). Similarly, baseline values recorded in male and female heterozygous and homozygous STX1A KO mice also coincided with normal R-wave durations (Pérez-Riera et.al, 2016)

Upon tamoxifen-treatment, a significant delay in R-wave to onset of contractility is observed within both male heterozygous (13 ± 0.4 ms) and homozygous STX1A KO mice (21 ± 1 ms) relative to Cre^+. The results coincide with findings by Virdi (2020) who utilized standard M-mode analysis and observed an electromechanical delay of 16 ± 2 ms in homozygous STX1A KO mice. Similar to males, female mice also demonstrated significant electromechanical disruption at week 0, with a 15 ± 1 ms delay recorded upon heterozygous KO, and 19 ± 1 ms delay upon homozygous STX1A KO (Figure 13). The electromechanical dyssynchrony persisted

into week 1, where significant delays between ventricular depolarization and contraction were recorded within both heterozygous KO males (12 ± 2 ms) and females (13 ± 1 ms) relative to Cre^+ mice. To add, time duration between R-wave and ventricular contraction was also prolonged in homozygous male (19 ± 1ms) and female mice (14 ± 1 ms) at week 1, which coincided with the 18.7 ± 2 ms delay recorded by Virdi (2020).

The effects of STX1A-KO induced electromechanical disruption were reduced to baseline function by week 3, with no statistical difference being observed amongst both male and female mice when compared to Cre^+ (Figure 13). Although a return in basal electromechanical function is consistent with the findings by previous laboratory members, Virdi (2020) reported a return in synchronicity by week 3, followed by a significant delay at weeks 4 and 6 which does not coincide with the current T2P analyses. By week 6, a complete recovery in R-wave to onset of contractility is observed amongst Cre^+, heterozygous and homozygous KO male and female mice (Figure 13), and the findings correlate with the return in systolic function noted *via* speckle-tracking and parasternal M-mode analyses (Figure 7).

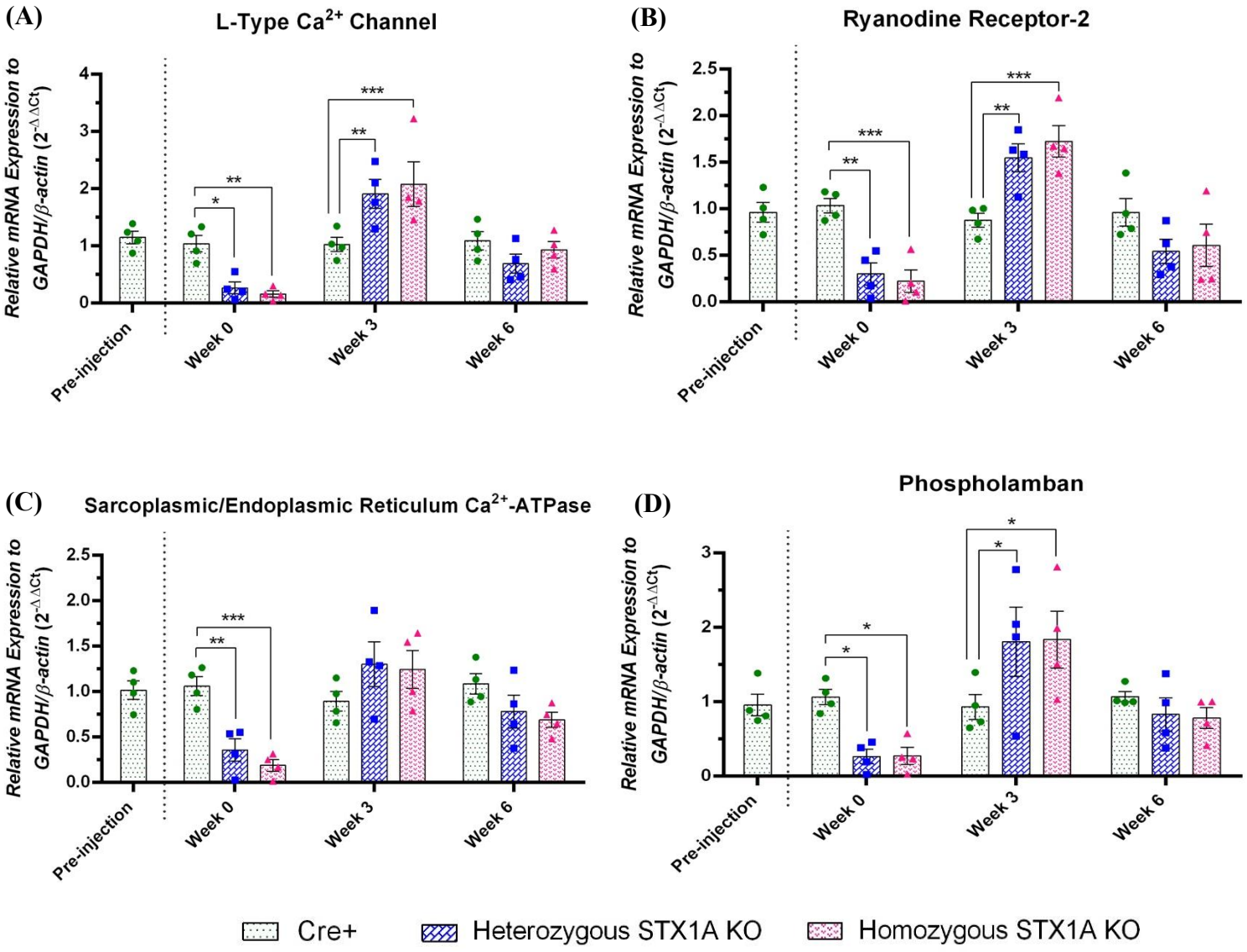

Figure 14: Assessment of Ca^{2+}-handling gene expression in LV free-wall samples within female Cre^{+}, heterozygous, and homozygous STX1A KO mice pre-injection, post-injection, and 3- and 6-weeks post-injection. Heterozygous and homozygous KO of STX1A elicited a significant reduction in **(A)** LTCC **(B)** RyR2, **(C)** SERCA2a and **(D)** Plb mRNA transcripts at week 0. By week 3, a significant upregulation in LTCC, RyR2 and Plb levels were reported, while increase in SERCA2a expression was not deemed significant (**C**). At end-stage (week 6), a return to baseline mRNA levels were observed for all four Ca^{2+}-handling genes, demonstrating no statistical significance when compared to Cre^{+} mice. All results were analyzed utilizing the $2^{-\Delta\Delta Ct}$ with a sample size of n = 4 per group, and mRNA levels were normalized to housekeeping GAPDH and β-actin. Graphed valued are represented as mean ± SEM, and a two-way ANOVA test was performed for statistical analysis ($p<0.05$ = *; $p<0.005$ = **; $p<0.0005$ = ***; $p < 0.0001$ = #).

3.6 STX1A KO induces transient downregulation of E-C coupling gene expression

Through conventional echocardiography and speckle-tracking, it was revealed that STX1A KO elicits temporary electromechanical dysfunction of the LV as demonstrated through global systolic dysfunction (Pk%) and segmental dyssynchrony (TPk). Since the process of E-C coupling tightly links electrical signalling to the contractile response of the myocardium, it was hypothesized that delays in electrical signalling may also disrupt normal Ca^{2+} handling which further gives rise to the phenotype of systolic dysfunction. To investigate this, the gene expression of L-type Ca^{2+} channel (LTCC, *Cacna1c*), ryanodine receptor-2 (RyR2, *Ryr2*), sarcoplasmic-endoplasmic reticulum Ca^{2+} ATPase (SERCA2a, *Atp2a2*) and phospholamban (Plb, *Plb*) were assessed pre- and post-tamoxifen treatment, three-weeks post-KO, and six-weeks post-KO in female mice.

Upon assessment, the Cre^{+} group did not demonstrate any significant alterations in *Cacna1c* gene expression across all studied time-points (week -1 = 1.2 ± 0.1; week 0 = 1.04 ± 0.1; week 3 = 1.02 ± 0.1; week 6 = 1.1 ± 0.2). However, heterozygous KO of STX1A induced a 75% reduction ($p = 0.0114$) in mRNA levels at week 0, while homozygous KO elicited an 85% reduction ($p = 0.0037$) when compared to Cre^{+} mice (Figure 9A). Furthermore, the downregulation in LTCC transcript levels were limited to week 0, as a significant increase in gene expression was recorded by week 3 within both heterozygous (1.87*x fold-increase*; $p = 0.0034$) and homozygous KO mice (2.03*x*, $p = 0.0005$) in relation to Cre^{+} mice. Furthermore, no significant difference in mRNA levels were recorded by week 6 within heterozygous (0.70 ± 0.2; $p = 0.3186$) and homozygous KO mice (0.93 ± 0.1; $p = 0.9008$) in relation to Cre^{+} (1.10 ± 0.2) (Figure 14A).

Similar to *Cacna1c* gene transcript levels, the expression of *Ryr2* remained unchanged pre- and post-treatment in Cre^+ female mice (Figure 9B). However, a 71% reduction in mRNA transcript levels were recorded in heterozygous STX1A KO mice ($p = 0.014$), while homozygous KO demonstrated a 79% decrease ($p = 0.0004$) post-treatment. Furthermore, similar expression patterns to LTCC were also observed by week 3, with mRNA levels being significantly elevated in heterozygous (1.54 ± 0.2; $p = 0.0036$) and homozygous KO mice (1.72 ± 0.2; $p = 0.0002$) while Cre^+ mice remained unchanged (0.96 ± 0.1). The increase was not sustained past week 3, as *Ryr2* expression returned to baseline by week 6 and demonstrated no significant difference when compared to the Cre^+ mice (Figure 14B).

The mRNA expression of *Cacna1c* and *Ryr2* coincides with results acquired from echocardiographic and strain analysis, demonstrating significant downregulation at week 0 and improved function by week 3, prior to a return in baseline by week 6. Downregulation of *Cacna1c* and *Ryr2* can directly impair the cytosolic Ca^{2+} flux, which can in turn effect the Ca^{2+}-handling dynamics of *Atp2a2* as well. Upon observation, *Atp2a2* levels were also significantly downregulated at week 0, from a relative expression of 1.06 ± 0.1 in Cre^+ mice to 0.36 ± 0.1 ($p = 0.0029$) in heterozygous KO mice, and 0.19 ± 0.1 ($p = 0.0002$) in homozygous KO mice. Furthermore, although an increase in *Atp2a2* levels were recorded at week 3, the improvement is not statistically significant when compared to the Cre^+ across both heterozygous ($1.46x$; $p = 0.1241$) and homozygous KO mice ($1.4x$; $p = 0.2192$).

Alongside SERCA2a, its allosteric inhibitor phospholamban also demonstrated a similar expression profile post-tamoxifen treatment. By week 0, *Plb* levels had reduced by ~80% within both heterozygous ($p = 0.028$) and homozygous STX1A KO mice ($p = 0.0298$), while being sustained within Cre^+ mice (Figure 9D). However, unlike SERCA2a, a significant improvement

in *Plb* expression was recorded by week 3, with an observed 88% increase in heterozygous KO mice ($p = 0.0278$) and 90% increase in homozygous KO mice ($p = 0.0229$) when compared to Cre^+. Similar to all Ca^{2+}-handling genes assessed, a reduction back to baseline levels was observed by week 6, with no statistical significance observed in the heterozygous and homozygous KO groups (Figure 14D).

Male (n = 8)

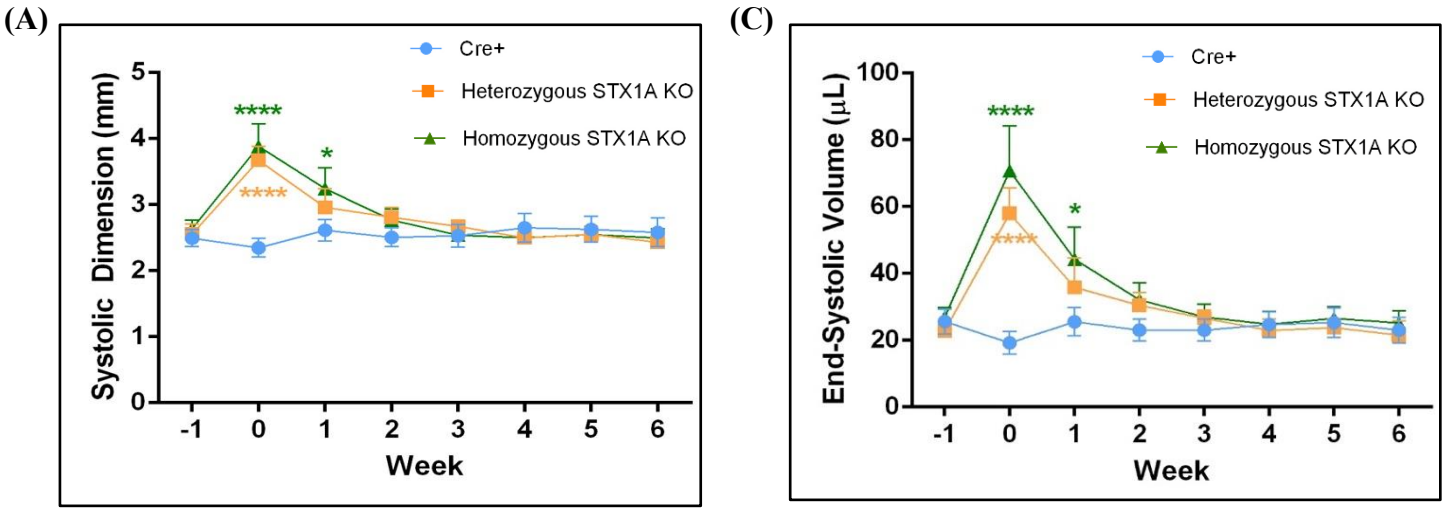

Female (n = 8)

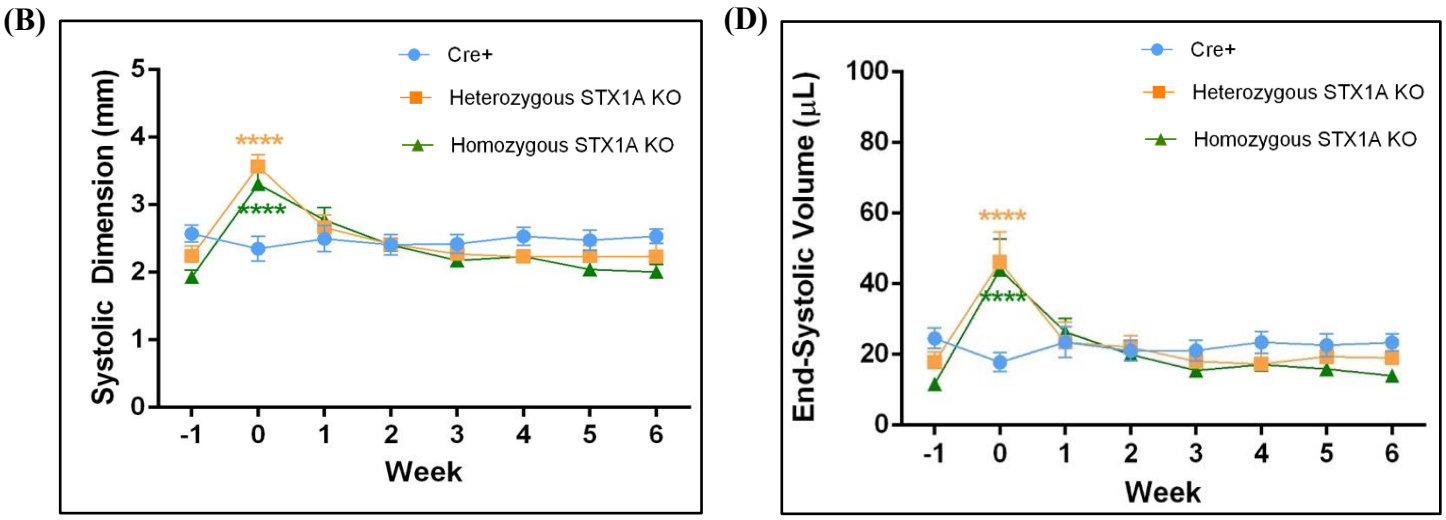

Figure 15: Transthoracic M-mode analysis of left-ventricular end-systolic dimension (LVEDs) and volume (LVEVs) in Cre^{+}, heterozygous, and homozygous STX1A KO mice. **(A)** Post-tamoxifen treatment, a significant increase in LVEDs is observed within heterozygous and homozygous KO male mice which persists into week 1 prior to recovery. **(B)** Female STX1A KO mice also demonstrate an elevation in LVEDs at week 0, but a return in systolic dimension is reported by week 3. Along with increased LVEDs, heterozygous and homozygous KO of STX1A elicits a significant increase in end-systolic volume within **(C)** male and **(D)** female KO mice. A return to baseline LVEVs is reported in male and female heterozygous KO mice by week 1, whereas male mice continue to demonstrate significant elevation until week 1. All values are represented as mean ± SEM with a sample size of n = 8 utilized per group. A two-way ANOVA was performed for statistical analysis ($p<0.05$ = *; $p<0.0005$ = ***; $p < 0.0001$ = ****).

3.7 Systolic dysfunction is associated with LV volume-overload

The reduction in contractile function was further reflected in the left-ventricular end-systolic dimension (LVEDs), whereby a 35% increase in LVEDs ($p < 0.0001$) was recorded upon heterozygous KO in males, and a 38% increase ($p < 0.0001$) in homozygous KO. Similarly, female mice demonstrated a significant increase in LVEDs within both heterozygous (33%; $p < 0.0001$) and homozygous KO mice (27%; $p < 0.0001$) when compared to Cre^+ at week 0 (Figure 15A, B). An elevation in LVEDs can occur as a consequence of increased hemodynamic stress on the ventricular chamber which can lead to cardiac remodelling, and the cause of such stress can be due to sustained pressure- or volume-overload.

To assess if pressure-overload within the LV induced a decline in cardiac function, invasive hemodynamic assessments by Virdi (2020) revealed a significant decline in the peak rate of pressure change (dP/dt) within the LV post-homozygous STX1A KO. The reduction in dP/dt measurements were observed throughout systole and diastole, with an increase in ventricular pressure only observed by week 3 (Virdi, 2020). To add, elevation in ventricular pressure is often coordinated with thickening of the ventricular wall to compensate the pressure-overload and maintain normal cardiac output. As demonstrated, no significant increase in posterior-wall thickness was recorded within Cre^+ or homozygous STX1A KO mice, suggesting the phenotype of systolic dysfunction not to be linked to pressure-overload (Virdi, 2020).

Opposingly, as demonstrated through M-mode analysis, a significant elevation in LV end-systolic and diastolic volumes (LVEVs and LVEVd) are observed post-heterozygous and homozygous KO of STX1A (Table 3, 4). By week 0, heterozygous KO of STX1A induced a significant increase in LVEVs by 57.9 ± 7.1 µL in males ($p < 0.0001$), and 46.1 ± 9.0 µL in female mice relative to Cre^+ ($p < 0.0001$) (Figure 10A). Moreover, homozygous KO of STX1A

also elevated the LVEVs by 49.6 μL ($p < 0.0001$) and 29.5 μL ($p < 0.0001$) in male and female mice respectively (Figure 15C, D). The significant increase in end-systolic volume correlates with the findings by Virdi (2020), who recorded an elevation from 18.1 ± 1.5 μL to 51.7 ± 8.9 μL upon homozygous KO of STX1A at week 0.

The elevation in LVEVs was sustained into week 1 within male mice, which continued to demonstrate a significant increase of 42.2% ($p = 0.0377$) under homozygous KO conditions. Although a 28.8% ($p = 0.4476$) increase was also recorded in heterozygous KO mice, the change was not deemed significant relative to Cre^+ (Figure 15C). A return in basal LVEVs was observed by week 2 which differs from the findings by Virdi (2020), who observed a continued significant increase into week 3. Moreover, STX1A KO did not elicit any significant changes in the LVEVs within female mice past week 0, demonstrating a return to baseline levels within both heterozygous (23.5 ± 5.7 μL; $p > 0.9999$) and homozygous groups (26.3 ± 3.8 μL; $p = 0.8669$) by week 1.

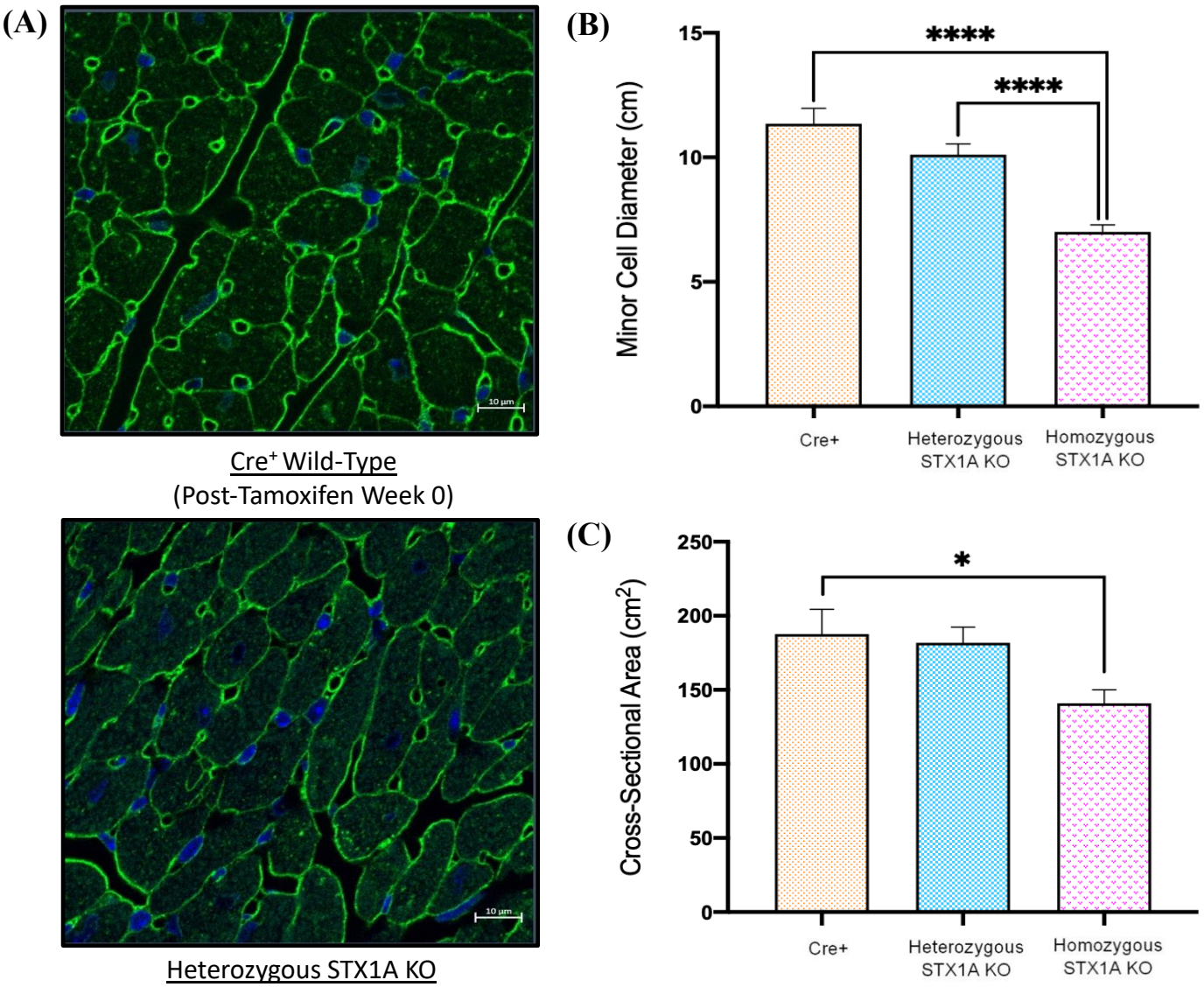

Figure 16: Alterations in cardiomyocyte diameter (cm) and cross-sectional area (CSA; cm^2) assessed on wheat-germ agglutinin stained left-ventricular myocytes at week 0. Histological slides with four-chamber heart sections were stained with WGA (1:500; green) and DAPI (blue) in mounting medium. **(A)** WGA staining of LV wall reveals altered cardiomyocyte shape along the short axis, with homozygous KO inducing significant decrease in **(B)** minor-cell diameter, and **(C)** total-CSA. Cell-diameter and CSAs were assessed in 10 cardiomyocytes (n = 2 hearts) across two visual fields, and results demonstrate the mean ± SEM. Images were acquired utilizing the ZEISS LSM 700 confocal microscope using a 63x oil immersion lens, and analysis was performed utilizing the ImageJ software. A one-way ANOVA test was performed for statistical analysis ($p > 0.05$ = ns; $p < 0.05$ = *; $p < 0.0001$ = ****).

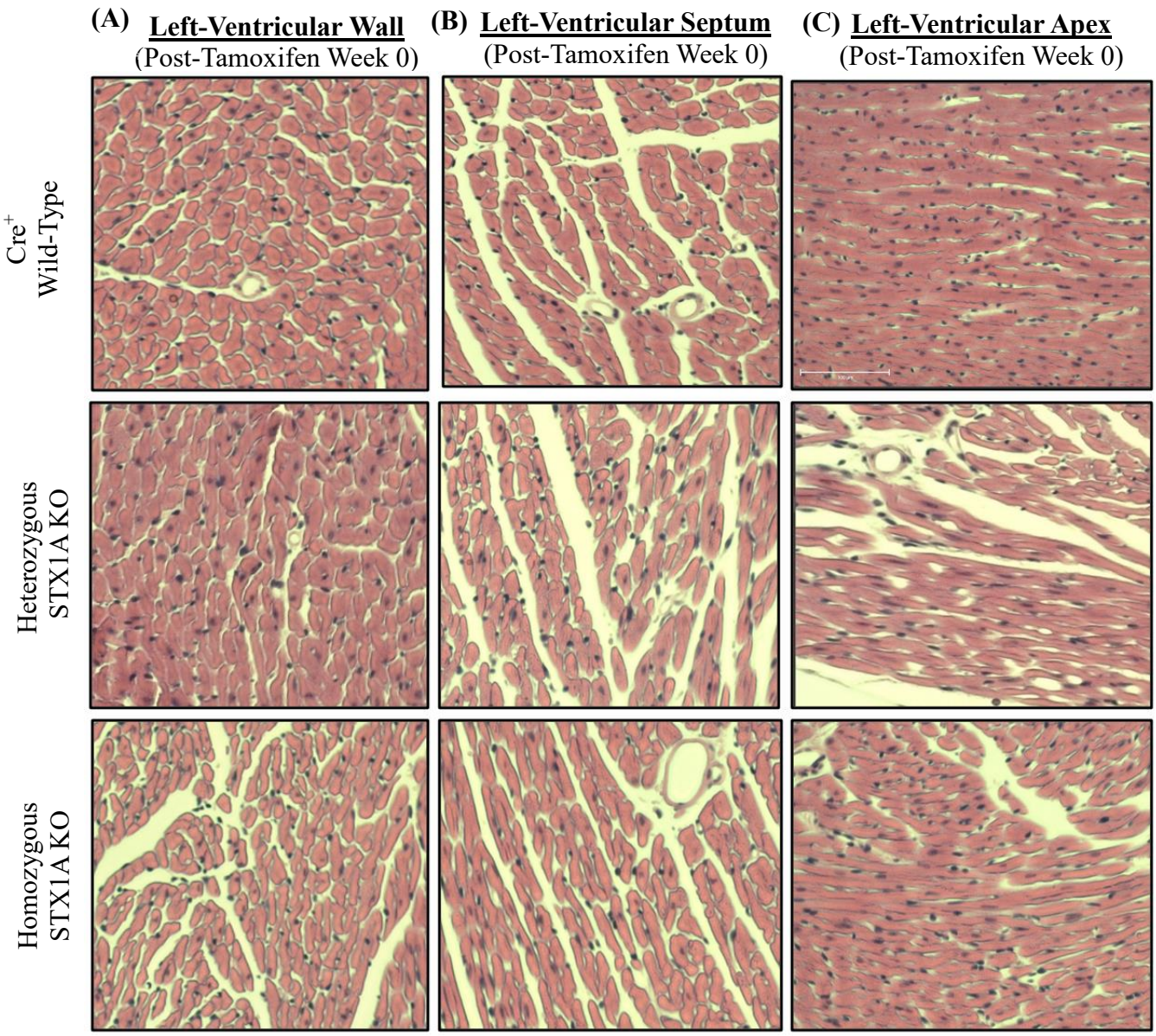

Figure 17. Hematoxylin and eosin (HE) stained sections of left-ventricle post-tamoxifen treatment in female Cre^{+}, heterozygous, and homozygous STX1A KO mice. Left-ventricular brightfield imaging was conducted utilizing the ZEISS Optical Imaging microscope at 20X magnification. Results demonstrate alteration in cardiomyocyte shape (elongation) at the **(A)** left-ventricular wall and **(B)** left-ventricular septum, while **(C)** cardiomyocytes at the left-ventricular apex demonstrate reduced cellular width (n = 2 per group).

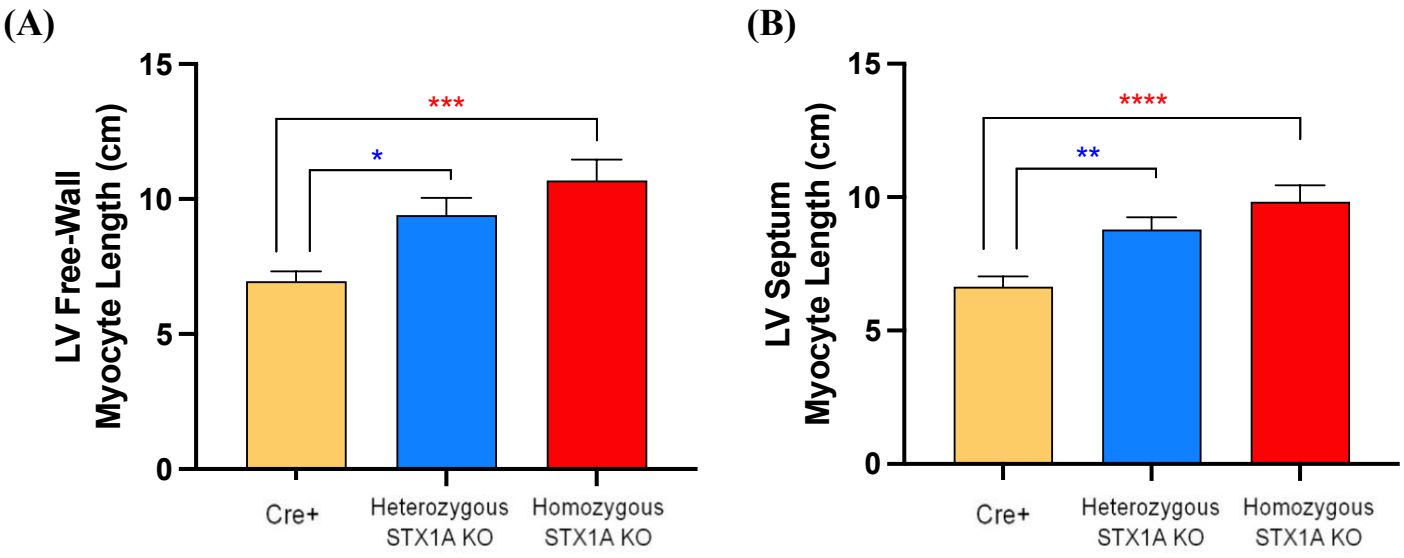

Figure 18. Assessment of myocyte length and width post tamoxifen-treatment in Cre^{+}, heterozygous, and homozygous STX1A KO left-ventricular samples. ImageJ was utilized to measure cardiomyocyte length of thirty cardiomyocytes (n = 2) at the LV free-wall. Haploinsufficiency in STX1A was shown to induce significant increase in myocyte length at the **(A)** LV free-wall and (**B)** LV septum. Results demonstrate the mean ± SEM, and a one-way ANOVA test was performed for statistical analysis ($p < 0.05$ = *, $p < 0.005$ = **, $p < 0.0005$ = ***, $p < 0.0001$ = ****).

3.8 STX1A haploinsufficiency induces cardiomyocyte elongation

A hallmark of volume overload induced cardiac remodelling is *eccentric* hypertrophy, whereby the myocardium adjusts to the hemodynamic load by adding sarcomeres in series. Consequently, the cardiomyocyte length becomes greater than its width as the heart dilates due to elevated preload (Samak et al., 2016). To assess if KO of STX1A induces eccentric remodelling, the cell diameter (width) was initially assessed on wheat-agglutinin-stained sections as described previously (Coelho-Filho et al., 2013). Upon analysis, the minor cell diameter of homozygous STX1A KO cardiomyocytes (7.3 ± 0.5 μm) was determined to be significantly shorter than heterozygous KO mice (9.8 ± 0.5 μm) and Cre^+ mice (11.4 ± 1.2 μm). The findings of reduced myocyte width in response to hemodynamic overload has been identified in studies pertaining tachycardia-induced ventricular failure, revealing a significant elevation in end-systolic and diastolic volumes, alongside a reduction in cardiomyocyte width from 23 ± 2 μm to 16 ± 1 μm (Spinale et al., 1991). Reduced myocyte width is also observed during reverse hypertrophic modelling within LVAD patients, who similarly displayed a reduction in myocyte diameter from 23.9 ± 3.6 μm to 15.7 ± 2.2 μm (Rivello et al., 2001).

Accompanying a reduction in cardiomyocyte diameter within homozygous KO mice, a significant decrease in the total CSA was also recorded (133.4 ± 15.5 μm^2) relative to Cre^+ mice (182.3 ± 26.3 μm^2). At the same time, heterozygous KO did not induce significant changes in total CSA when compared to Cre^+ mice (168.8 ± 18.4 μm^2) (Figure 16C). Although the significant reduction in cardiomyocyte diameter mice can be further reflective of decreased CSA within homozygous STX1A mice, a general reduction in the total CSA is not always observed during eccentric remodelling. Rather, generation of ventricular volume-overload *via* mitral regurgitation (MR) surgery has demonstrated comparable CSAs between sham and MR-treated

mice (Li et al., 2020), while studies employing the aortic regurgitation (AR) model revealed significant elevation in the total CSA two weeks post-surgery (Wu et al., 2020).

To further assess the possibility of eccentric remodelling, ventricular sections were also stained with hematoxylin and eosin (HE) to allow for clear observation of cardiomyocyte boundaries and thereby assessment of cell length. Upon analyses, a significant increase in cardiomyocyte length was observed at the left-ventricular free wall and septum in the KO mice (Figure 17A and B, 18A and B). More specifically, Cre^+ mice demonstrated a mean myocyte length of 6.9 ± 0.4 μm at the LV free-wall, while heterozygous and homozygous KO showed a significantly greater length of 9.4 ± 0.6 μm and 10.7 ± 0.8 μm; respectively. Cardiomyocyte length was also recorded to be greater at the LV septum of the heart, with heterozygous KO (8.8 ± 0.5 μm) and homozygous KO (9.8 ± 0.6 μm) eliciting a significantly greater length relative to Cre^+ (6.6 ± 0.4 μm). The findings are concurrent with the results reported by Li et al. (2020), who demonstrated a significant increase in the length of mono- and binucleated cardiomyocytes upon MR surgery-induced eccentric hypertrophy. To add, the work by Ohler et al. (2009) directly correlates with the current results, demonstrating an increase in the length and perpendicular decline in width of heart failure cardiomyocytes undergone eccentric hypertrophy. Analysis of myocyte length at the LV apex presented difficulty in identification of cardiomyocyte boundaries and was therefore not quantified. However, a visible decrease in myocyte width is apparent within both heterozygous and homozygous KO groups (Figure 17C).

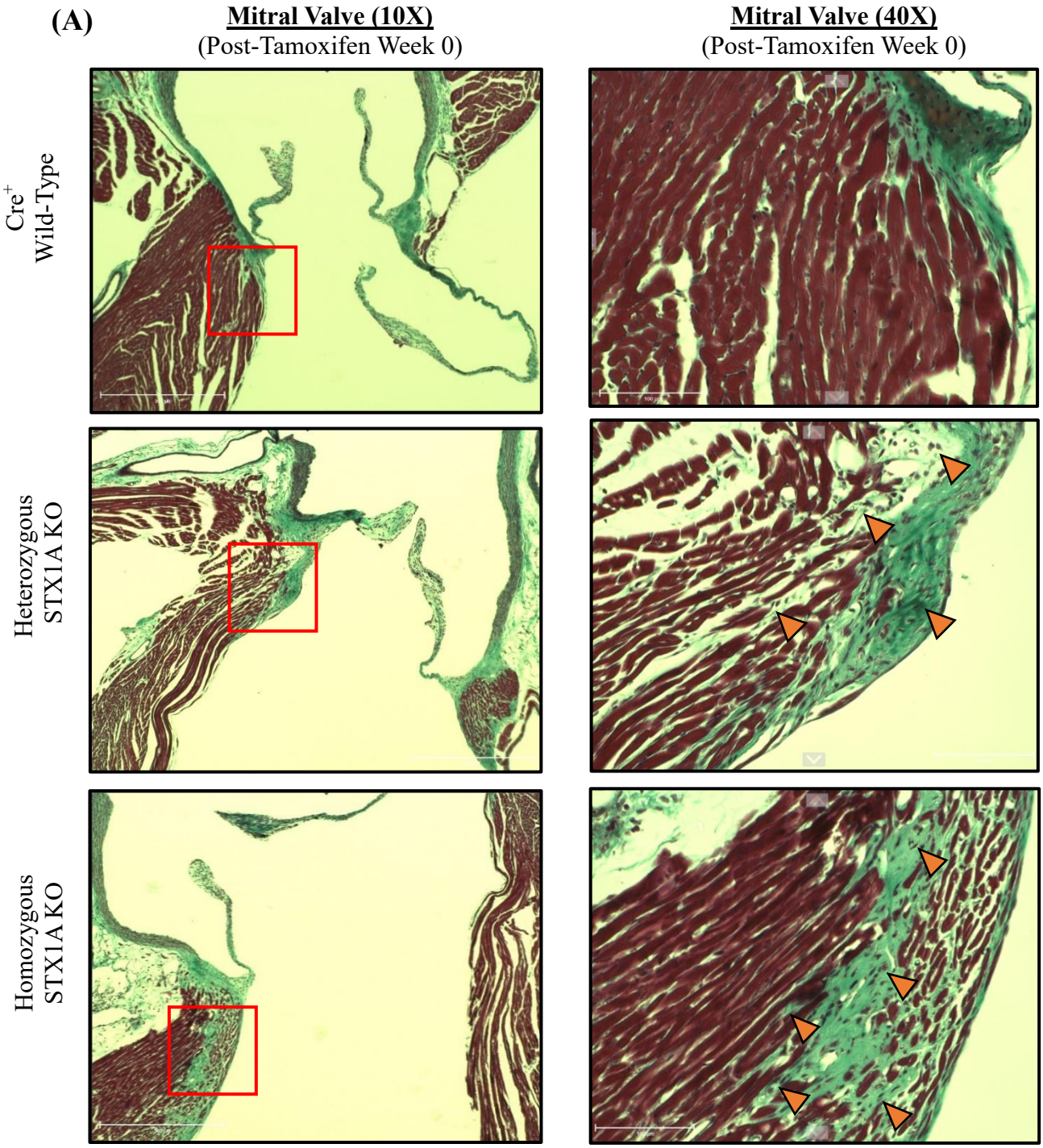
(A)
Mitral Valve (10X)
(Post-Tamoxifen Week 0)
Mitral Valve (40X)
(Post-Tamoxifen Week 0)
Cre+ Wild-Type
Heterozygous STX1A KO
Homozygous STX1A KO

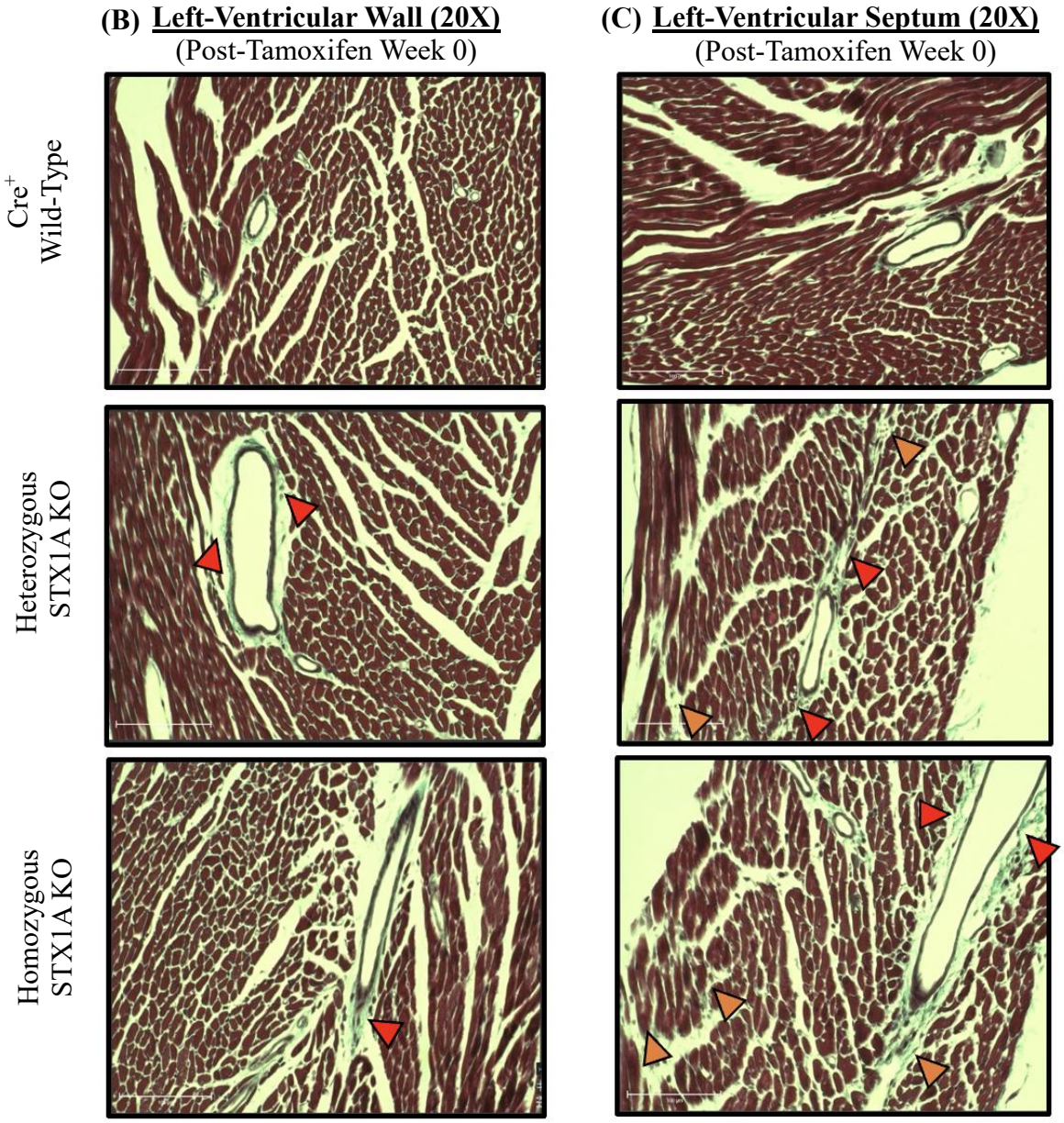

Figure 19: Masson's trichrome stained sections of left-ventricle post-tamoxifen treatment in female Cre^{+}, heterozygous and homozygous STX1A KO mice. Masson's trichrome stains for cardiomyocytes in red, and collagen deposition in green. **(A)** Post-tamoxifen treatment, development of interstitial fibrosis (orange arrows) is noted at the mitral valve in STX1A KO mice which is absent in Cre^{+} mice. Minimal perivascular fibrosis (red arrows) is also observed at the left-ventricular wall **(B)**, while LV septum demonstrates the presence of both interstitial and perivascular fibrosis post-STX1A KO **(C)** (n = 2 per group).

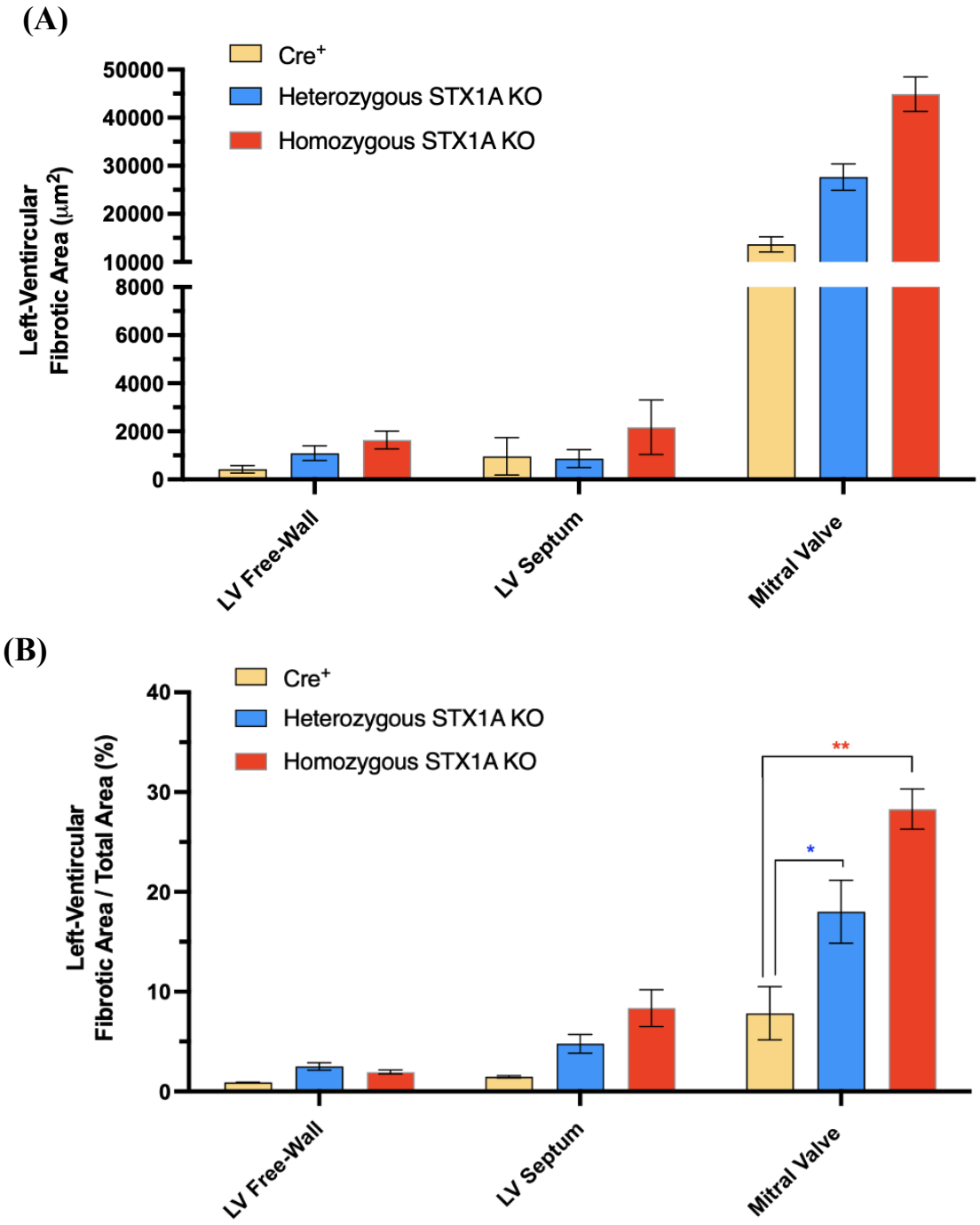

Figure 20: Assessment of fibrosis at the left-ventricular free-wall, septum and mitral valve *via* Masson's trichrome staining in Cre$^+$ and STX1A KO mice. ImageJ was utilized to calculate the **(A)** total fibrotic area (μm^2) and normalized to total area occupied by cardiomyocytes **(B).** Although an increase in collagen deposition is observed at the left-ventricular septum, significant elevation is only recorded at the mitral valve when compared to Cre$^+$ mice. Graphs demonstrate the mean ± SEM fibrotic area with a sample size of n = 2, and a two-way ANOVA test was performed for statistical analysis ($p < 0.05$ = ns).

3.9 STX1A-KO causes localized fibrosis of the LV

Alongside an alteration in cardiomyocyte length with maintained wall thickness, pathological eccentric remodelling is correlated with mild or complete absence of LV fibrosis, while concentric remodelling is linked with severe fibrotic remodelling of the ventricle (Kehat and Molkentin, 2010). To assess for collagen deposition induced by STX1A KO, heart sections were stained with Masson's trichrome post-tamoxifen treatment and fibrotic area was quantified.

Upon analysis, no significant difference in collagen deposition was observed at the LV free-wall post-KO. Within the free-wall, heterozygous KO of STX1A only elicited a 1.6% ($p = 0.2010$) increase in fibrotic area, while homozygous KO caused a 1.1% increase ($p = 0.1526$) when compared to Cre^+ mice (Figure 19A, 20). Elevated levels of fibrosis were recorded at the left-ventricular septum however, where cardiac fibrosis and collagen deposition was raised by a factor of 3.2-fold ($p = 0.2269$) within heterozygous KO mice, and 5.7-fold ($p = 0.2337$) within homozygous KO mice (Figure 20). The collagen deposition was primarily localized around existing blood vessels and is hence classified as perivascular fibrosis, which has been tightly linked to cardiovascular dysfunction (Ytrehus et al., 2018) (Figure 19C; red arrows). More specifically, similar reports of elevated perivascular fibrosis have been observed in mice with dilated cardiomyopathy, with Chu et al. (2019) demonstrating a $12.3 \pm 0.3\%$ increase upon stress-induced cardiomyopathy. Furthermore, a 3.83-fold increase in perivascular fibrosis has been elucidated in diabetic mice demonstrating significantly reduced EF, which coincides with the current findings (Tu et al., 2019).

To add, perivascular fibrosis of the blood vessels was also accompanied by minimal interstitial fibrosis, as marked by yellow arrows (Figure 19C). However, greatest levels of interstitial fibrosis was observed near the mitral valve leaflet, where heterozygous KO mice

demonstrated a significant increase of 10.2% ($p = 0.0422$), while homozygous KO displayed a 20.5% increase ($p = 0.19$) in net fibrotic area (Figure 19A, 20). Unlike Cre^+ mice, the collagen deposition of the mitral valve is not limited to the extracellular boundary of the LV septum. Rather, fibrosis was significantly spread interstitially into the myocardium, penetrating in-between cardiomyocytes, and spreading apically down the septum which was absent in Cre^+ mice.

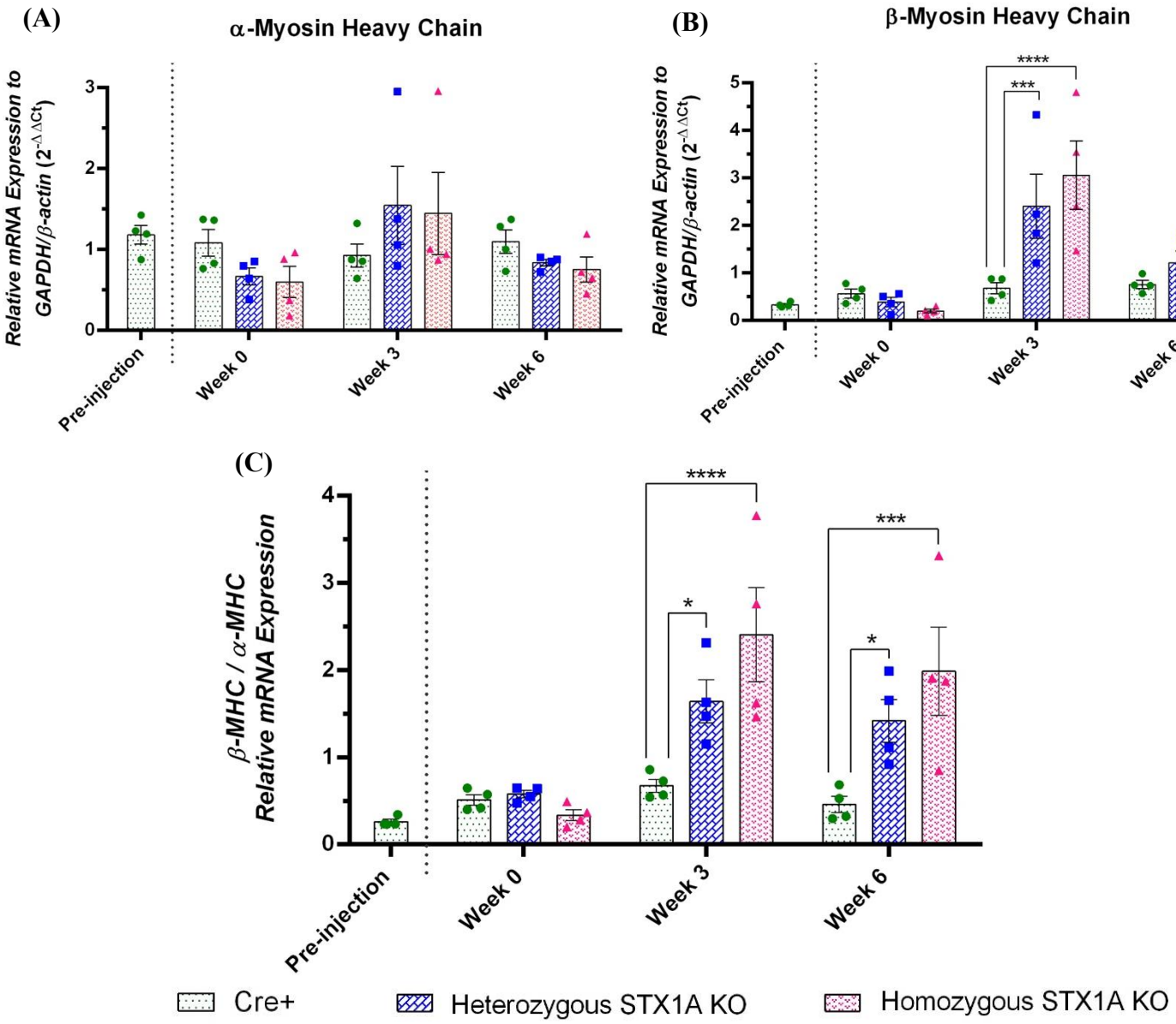

Figure 21: RT-qPCR conducted at pre-injection, post-injection, and 3- and 6-weeks post-injection for alterations in cardiac α-MHC and β-MHC gene expression in Cre^{+} and STX1A KO mice. STX1A haploinsufficiency demonstrates a decrease in **(A)** α-MHC and (**B)** β-MHC mRNA levels at week 0. By week 3, a significant increase in β-MHC levels are recorded and is further demonstrated in β-MHC/α-MHC mRNA ratios **(C).** α-MHC and β-MHC demonstrate return in baseline expression by week 6, with β-MHC expression being significantly greater in STX1A heterozygous and homozygous KO mice. All results were analyzed utilizing the $2^{-\Delta\Delta Ct}$ with a sample size of n = 4 per group, and mRNA levels were normalized to housekeeping GAPDH and β-actin. Graphed valued are represented as mean ± SEM, and a two-way ANOVA test was performed for statistical analysis ($p<0.05$ = *; $p<0.005$ = **; $p<0.0005$ = ***; $p < 0.0001$ = #).

3.10 STX1A-KO induces fetal gene re-expression at the LV free-wall

Under stress-induced pathological remodelling, a shift in the myosin-heavy chain isoform also occurs in attempts to reduce energy expenditure while countering hemodynamic overload. Specifically, expression of the predominant fast-contracting α-MHC isoform is reduced in the left ventricle of the mouse heart, while transcription of the slow-contracting, energy efficient β-MHC isoform is elevated (Taegtmeyer, Sen and Vela, 2013). Therefore, to assess if sarcomeric remodeling takes place as a result of STX1A KO, RT-qPCR for α-MHC and β-MHC was performed on LV free-wall samples pre-injection, alongside week 0, week 3 and week 6

The transcript levels of α-MHC and β-MHC were sustained across all four time points in Cre^+ mice, with no significant variation observed throughout the course of the study (Figure 21A, B). At week 0, a reduction in α-MHC mRNA was recorded in heterozygous (32.5%, $p = 0.5307$) and homozygous KO mice (44.8%, $p = 0.3997$), although the decrease was not significant when compared to Cre^+. A similar reduction in β-MHC transcript levels were reported, whereby heterozygous KO elicited a 31.6% reduction ($p = 0.9668$) while homozygous KO induced a 64.7% decline ($p = 0.7794$), with the results lacking statistical significance. To assess if a switch in the net transcription of β-MHC takes place however, a ratio of β-MHC to α-MHC (β/α) was taken, revealing comparable values amongst Cre^+ mice (0.51 ± 0.1), heterozygous KO mice (0.58 ± 0.1, $p = 0.9963$) and homozygous KO mice (0.34 ± 0.1, $p = 0.9403$). The results collectively suggest no significant improvement in β-MHC transcript levels at week 0, and the results are consistent with previously published findings. For instance, upon performing volume overload in 12-week female mice by creating a shunt between the aorta and vena cava (aorto-caval shunt; ACS), Toischer et al. (2010) demonstrated no significant changes in β-MHC

expression 24-hours post-surgery, despite of a significant elevation in end-systolic and diastolic dimensions.

By week 3, a respective 1.64-fold ($p = 0.2$) and 1.56-fold ($p = 0.3385$) increase in α-MHC transcript levels are recorded within heterozygous and homozygous KO mice. The results, however, demonstrate inter-sample variation in α-MHC levels, with expression ranging from 0.17 to 0.96, thereby not making the increase significant at week 3. Opposingly, heterozygous KO of STX1A induced a significant 3.54-fold ($p = 0.0008$) increase in β-MHC transcript levels at week 3, while homozygous KO improved transcript levels by a factor of 4.50-fold ($p < 0.0001$). The elevation in β-MHC expression is further reflected in the β/α ratios, demonstrating significantly greater values at week 3 within heterozygous KO mice (1.64 ± 0.2; $p = 0.0215$) and homozygous KO mice (2.41 ± 0.5; $p < 0.0001$) while Cre^+ mice continued to demonstrated baseline β/α expression (0.67 ± 0.1). Significant elevation in the β-MHC isoform was also recorded by Freire et al. (2007), who observed a 4-fold increase in β-MHC levels four-weeks post-induction of ACS surgery without a significant increase in α-MHC mRNA.

By end-stage or week 6, β-MHC continued to present as the dominant isoform being transcribed within the LV free-wall post-STX1A KO. This is demonstrated within the β-MHC/α-MHC ratios, as heterozygous KO continued to induce a significant 3.1-fold increase ($p = 0.0228$) in the LV free-wall, while homozygous knockout revealed a 4.4-fold elevation ($p = 0.0002$) in comparison to Cre^+ mice. Continued significant increase in β-MHC mRNA levels were also recorded by Freire and colleagues (2007) by week-10 post-surgery and are further consistent with the current findings.

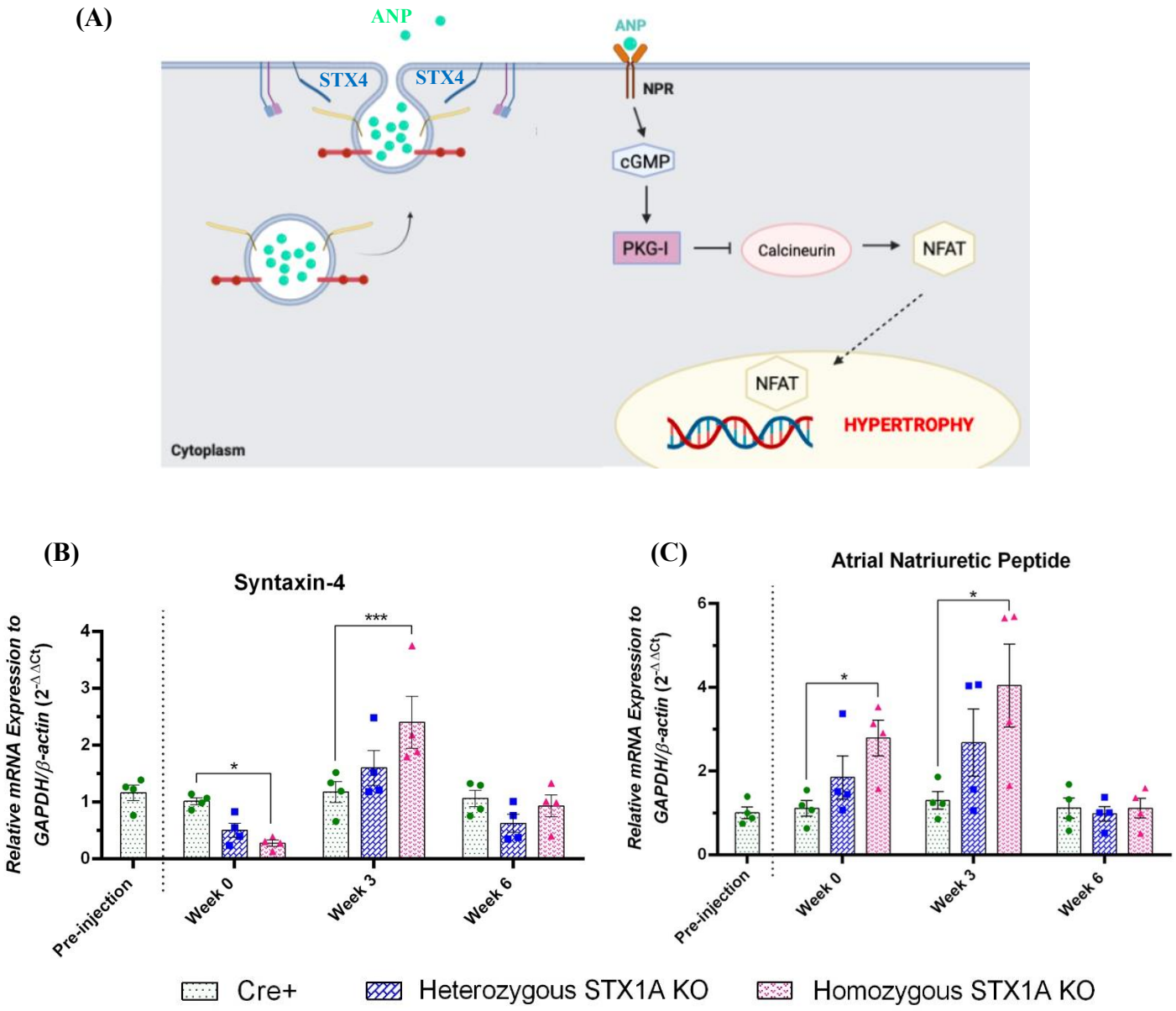

Figure 22: Schematic representation of STX4-mediated release of ANP in ventricular cardiomyocytes, and assessment of STX4 and ANP mRNA levels in Cre^{+} and STX1A KO mice. (A) ANP demonstrates a vital inhibitory role against NFAT-mediated hypertrophic gene signalling in cardiomyocytes, and secretion of ANP is dependent on STX4 expression. **(B)** Gene expression analysis reveal a significant decline in STX4 mRNA transcripts in homozygous STX1A KO mice at week 0 with a parallel increase in ANP transcripts. At week 3, a significant increase in gene transcription of STX4 and ANP are recorded, which are returned to baseline expression by week 6 in heterozygous and homozygous KO mice. All results were analyzed utilizing the $2^{-\Delta\Delta Ct}$ with a sample size of n = 4 per group, and mRNA levels were normalized to housekeeping GAPDH and β-actin. Graphed valued are represented as mean ± SEM, and a two-way ANOVA test was performed for statistical analysis ($p<0.05$ = *; $p<0.005$ = **; $p<0.0005$ = ***; $p < 0.0001$ = #). Illustration was created on www.biorender.com.

3.11 Reduction in STX4 levels and elevation in ANP transcripts upon STX1A KO

STX4 is a major SNARE protein responsible for interacting with vesicle-SNAREs VAMP-1 and VAMP-2 to induce exocytosis of ANP (Figure 22A). The secretion of ANP in the heart thereby not only functions to reduce blood pressure and volume, but also demonstrates a crucial role in inhibition against hypertrophic gene signalling (Figure 16A). Hence, to determine if KO of STX1A also altered the transcription of STX4 and ANP, RT-qPCR was performed at pre-injection states, alongside week 0, 3 and 6.

Upon heterozygous KO of STX1A, a 50.3% reduction ($p = 0.2343$) in STX4 mRNA levels were recorded which was not deemed statistically significant relative to Cre^+. This was unlike what was observed in homozygous STX1A KO, where a significant decrease of 72.8% ($p = 0.044$) was recorded. The KO-induced downregulation in STX4 levels has been demonstrated previously by Virdi (2022) and Faizan (2022) in LV free-wall samples, displaying a linear decline in STX4 transcripts across both heterozygous and homozygous KO groups in response to STX1A haploinsufficiency (Supplementary Figure 1). Alongside a reduction in STX4 levels at week 0, RT-qPCR analysis revealed a 40% upregulation in ANP levels in heterozygous KO mice ($p = 0.5713$), while a 60.2% increase ($p = 0.0324$) was recorded upon complete KO. The findings of elevated ANP levels correlate with studies pertaining ventricular-volume overload, such as the work by Su et al. (1999) who observed a 7-fold increase in ANP transcript levels 1-day post-ACS surgery in rats.

By week 3, both heterozygous and homozygous KO mice began to demonstrate recovery in STX4 levels beyond baseline expression. Specifically, heterozygous mice improved STX4 mRNA expression by a factor of 1.36-fold ($p = 0.3852$), although the levels continued to demonstrate statistical insignificance. At the same time, homozygous KO of STX1A

significantly improved STX4 transcript levels when compared to both Cre^{+} mice (2.04*x*, p = 0.0004) and heterozygous KO mice (1.50*x*, p = 0.0254). ANP levels also continued to demonstrate an increase in both heterozygous (2.06*x*, p = 0.0979) and homozygous KO mice (3.1*x*, p = 0.0003) at week 3, although significance was only reported upon complete KO of STX1A. Such significant elevation in ANP transcript levels as a response to ventricular volume overload is commonly observed, with the results coinciding with studies by Freire et al. (2007) who reported a 2.7-fold increase in ANP mRNA levels 4-weeks post-ACS in mice.

At end-stage analysis, STX4 mRNA levels returned to a baseline of 0.63 ± 0.2 (p = 0.3587) and 0.933 ± 0.2 (p = 0.9582) in heterozygous and homozygous mice respectively. Similarly, ANP levels also returned to levels comparable to Cre^{+} mice (0.98 ± 0.2, p = 0.9949) within both heterozygous and homozygous KO groups (1.1 ± 0.2, p > 0.0009) with no statistical significance, further coinciding with the return in basal function observed through conventional echocardiography and speckle-tracking strain analysis.

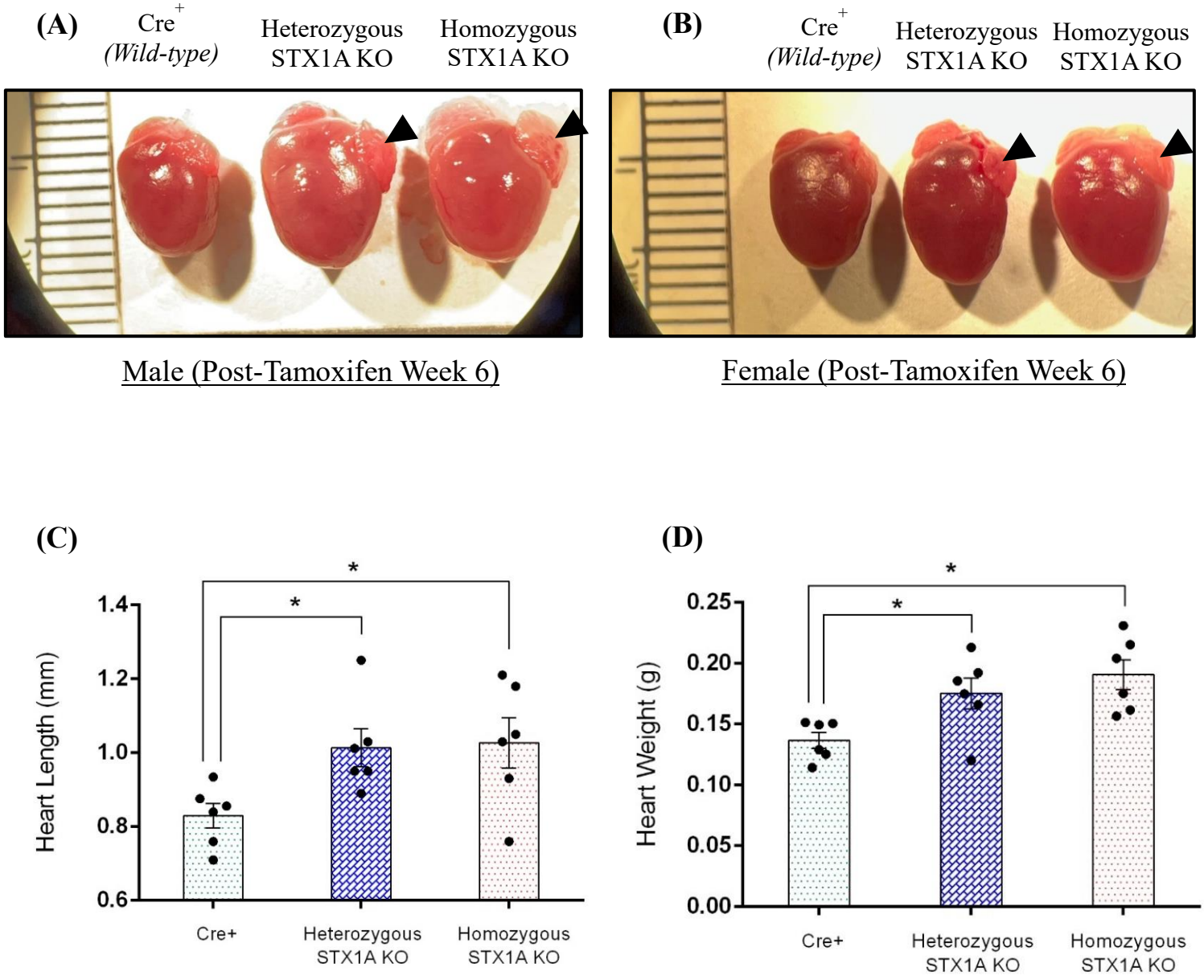

Figure 23: End-stage morphological changes in heart size and heart weight in male and female Cre^{+}, heterozygous, and homozygous STX1A KO mice. Visual observation of heart samples collected at endpoint demonstrate an enlargement in ventricular and atrial size within both **(A)** male and **(B)** female KO mice (black arrow denotes to left-atria). **(C)** Measurement from aorta to ventricular apex also revealed a significant elevation in heart length (cm) within heterozygous and homozygous STX1A KO mice at week 6. **(D)** End-stage analysis further revealed a significant elevation in heart weight (g) within STX1A KO mice relative to Cre^{+}. Values are plotted as mean SEM with a sample size of 6 mice per group, and statistical analysis was calculated *via* a one-way ANOVA test ($p < 0.05$ = *)

3.12 End-stage analysis reveals continued elongation and elevated heart weight

The end-stage results as observed through conventional echocardiography, strain analysis and RT-qPCR reveal a return in baseline contractile function by week 6 in knockout hearts. Although a return in function is noted, a persistent alteration in the heart morphology is also observed within both male and female mice (Figure 23A, B). At week 6, the heart weight is significantly elevated within heterozygous (0.19 ± 0.01g, $p = 0.023$) and homozygous KO mice (0.18 ± 0.01g, $p = 0.036$) in comparison to Cre^+ (0.14 ± 0.01g). An elevation in cardiac mass could occur as a response to improved function and venous return, and such findings are consistent with what is observed within pregnancy-induced eccentric remodelling (control heart = 126 ± 2 mg; eccentric hypertrophied heart = 178 ± 2 mg; Eghbali et al., 2005)

The continued elevation in heart weight after return in function is further supported by an alteration in the heart length as well. When measured from apex-to-base, heterozygous KO of STX1A demonstrated a significant increase in the heart length by 0.19 mm ($p = 0.043$) whereas a 0.20 mm increase was observed in homozygous KO mice ($p = 0.014$). Although histological analysis of heart-sections were only conducted at week 0, the current findings suggest continued elongation of the myocardium which was initially found at the left-ventricular apex and septum (Figure 18). Accompanying an alteration in heart weight and size, both heterozygous and homozygous KO of STX1A also induced enlargement of the left and right atria which was not observed within the Cre^+ group (Figure 23A, B).

CHAPTER 4: DISCUSSION

4.1 Results Overview

The aim of my thesis was to uncover the role of STX1A in cardiac E-C coupling utilizing an *in vivo* murine KO model. Since STX1A tightly interacts with and negatively regulates the pore-forming subunit of LTCC, it was initially proposed that cardiomyocyte-specific KO of STX1A would alleviate the inhibition, thereby increasing the inward Ca^{2+} current and contractile function of the heart. However, initial studies by Virdi (2020) revealed that homozygous KO of STX1A does not improve the contractile function, but rather induces temporary systolic dysfunction which persists for three-weeks. It is thereby suggested that KO of STX1A may disrupt normal electromechanical signal transduction, resulting in an abnormal E-C coupling event which elicits reduced contractions of the myocardium. The findings by Virdi (2020) were repeated within male and female counterparts utilizing a heterozygous and homozygous KO model, and demonstrated significant reductions in SV, EF, and CO which was consistent across both genders. Moreover, STX1A haploinsufficiency revealed complete mechanical dysfunction of the LV, alongside delays in electrical transduction at the mid and apical regions of the ventricle. The disruption in E-C coupling was further assessed through transcriptional alterations in Ca^{2+}-handling gene expression, revealing significant downregulation in LTCC, RyR2, SERCA2a, and Plb post-STX1A KO. Moreover, due to elevated volumetric overload in the LV chamber, it was also hypothesized that hypertrophic remodeling may be required to adjust to the hemodynamic load and return the heart to baseline function by week three. Upon analysis, a significant elevation in cardiomyocyte length was recorded, alongside reduced total-CSA in homozygous KO mice at week 0. Moreover, presence of interstitial and perivascular fibrosis was recorded, with significant fibrotic deposition at the mitral valve leaflet. Hypertrophic remodeling

was further assessed *via* the possibility of fetal-gene reprogramming, revealing significant elevation in β-MHC transcription at week 3 which persisted into week 6, alongside elevated ANP transcripts at week 0 and 3. End-stage morphological analysis also revealed enlargement of the heart length and weight which may be mandatory as the heart adapts to the new hemodynamic load.

4.2 Successful KO of STX1A in left-ventricular cardiomyocytes *via* Cre-recombinase

Cre-targeted KO of STX1A demonstrated significant success, eliciting a ~75% reduction in mRNA transcript levels at end-stage analysis, alongside ~74% protein KO efficiency within homozygous KO mice. Although the findings do not demonstrate complete KO of STX1A, it is important to note that Cre-recombinase is specifically driven under the α-MHC promoter which is only expressed in cardiomyocytes. Moreover, other cardiac cell types including vascular cells, endothelial cells and most specifically, fibroblasts do not express α-MHC so Cre-induced STX1A cannot take place in these cells (Shiojima et al., 1999). Although major efforts were made to ensure isolation of the left-ventricular free wall for RT-qPCR and Western blot analysis, the interventricular septum or apex could have also been included in the samples, where KO of STX1A cannot occur due to expression of fibroblasts, subendothelial and connective tissue layers (Arackal and Alsayouri, 2022). Another possibility for incomplete KO of STX1A could be due to incomplete activation of Cre by tamoxifen, as Virdi (2022) demonstrated a 90% reduction in STX1A using a different commercial source of tamoxifen. However, similar KO efficiencies utilizing the α-MHC Cre-recombinase mechanism has been reported in other studies, demonstrating a 70-80% efficacy in cardiac-specific gene knockout *via* use of tamoxifen or its isomer, 4-hydroxytamoxifen (Heinen et al., 2021; Huang et. al, 2009). Bersell et al. (2013) have

also reported Cre-mediated homologous recombination to have a ceiling effect of ~80%, and an increase in recombination efficiency requires greater doses of tamoxifen which can induce severe cardiotoxic effects.

4.3 Controlling for cardiotoxic effects caused by tamoxifen inducible-Cre

The use of tamoxifen and the inducible-Cre mechanism to drive spatio-temporal gene knockout continues to present as a challenge in assessing gene function, particularly due to the cytotoxic effects linked with the Cre-activation model. For instance, studies conducted by Bersell et al. (2013) demonstrated a significant decrease in the fractional shortening upon administration of 60 μg tamoxifen per kg of body weight over a course of three-days in mice. Moreover, although higher-level doses (i.e., 80 mg/kg over five days) have shown to be efficient in inducing total gene repression, a 60% increase in mortality can be recorded 60-days post-injection (Koitabashi et al., 2009). The primary reason for the secondary effects can be attributed to Cre-overactivation within cardiomyocytes, which has been linked to elevated DNA fragmentation, cell growth arrest, cellular apoptosis and even activation of cardioprotective signalling pathways (Bersell et al., 2013). Therefore, it is imperative to utilize a lower dose of tamoxifen when assessing gene function *via* the inducible model, alongside to control for the effects of Cre.

The initial research conducted by Virdi (2020) utilized important controls when assessing the effects of Cre, such as injection of Cre^{+} mice with peanut oil and tamoxifen at 20 mg/kg. Conclusively, no significant alterations in cardiac function were observed throughout eight-weeks of echocardiography, while homozygous STX1A KO demonstrated a significant decrease in contractile function which persisted for three-weeks (Virdi, 2020). Furthermore, although 20 mg/kg tamoxifen was shown to be sufficient in inducing protein knockdown through

immunohistochemical analysis, gene or protein repression *via* RT-qPCR and Western blotting were not conducted. It is now demonstrated in the current thesis and through the work by Virdi (2022), that utilization of tamoxifen at 40 mg/kg over a course of four-days is sufficient in inducing gene- and protein-knockdown of STX1A with unchanged expression in Cre^+ mice. To add, neither male or female Cre^+ mice demonstrated any alteration in cardiac function within the current thesis, in the findings by Virdi (2020), or by Virdi (2022), thereby denoting the effects of systolic dysfunction to be a result of STX1A haploinsufficiency – single copy of the STX1A allele was insufficient in producing the WT phenotype.

4.4 Disruption in Ca^{2+}handling causes systolic dysfunction in STX1A KO mice

Upon controlling for the effects of Cre^+, it was revealed that heterozygous and homozygous KO of STX1A elicited significant dysfunction of the left-ventricle within male and female mice. This was reported through 2-D M-mode echocardiographic analysis, revealing downregulation in the EF, SV, and CO post-tamoxifen treatment (Table 3, 4). To add, a recovery in function was recorded three-weeks post-KO in female mice, while males demonstrated a complete return in function by week 4. Due to decreased contractility of the heart, it was thereby hypothesized that an alteration in cardiac E-C coupling may occur post-STX1A KO, disrupting the intracellular Ca^{2+} dynamics and giving rise to the observed reduction in inotropic function.

A global rise in intracellular Ca^{2+} level, known as a "Ca^{2+} transient" is mandatory in inducing contractions of the myocardium. The healthy heart demonstrates a relatively short Ca^{2+} transient to ensure rapid SR Ca^{2+} release prior to reuptake for the subsequent cardiac cycle (Piacentino III et al., 2003). In patients undergoing heart failure due to dilated cardiomyopathy

however, Ca^{2+} transients can be significantly prolonged and impair the electromechanical response of the myocardium (Piacentino III et al., 2003).

Since L-type Ca^{2+} channels are the primary voltage-sensor and modulators of cardiac E-C coupling, their functional role directly impacts the Ca^{2+}-transient waveform. Upon heterozygous and homozygous KO of STX1A, it was revealed that $Ca_v1.2$ mRNA levels were significantly reduced, followed by a recovery in gene expression by week 3. Although transcript levels are not directly representative of protein expression, reduced mRNA levels can be suggestive of decreased translation to the $Ca_v1.2$ protein. In the latter case, STX1A has also shown to directly modulate post-translational modification of voltage-gated cardiac channels, which includes channel trafficking and gating properties at the membrane (Chao et al., 2011). Therefore, it is suggested that reduced expression of STX1A may disrupt the basal trafficking of $Ca_v1.2$ to the sarcolemma, reducing the number of available channels (*N*) and consequently decreasing the $Ca_v1.2$ macroscopic current. STX1A has also shown to co-localize with $Ca_v1.2$ at the plasma membrane, whereby mutations in the cysteine-residues alleviates the tight interaction with $Ca_v1.2$'s synprint motifs at cytosolic domains II and III (Atlas, 2014). The cysteine 272 and 273 residues are pivotal in interacting with $Ca_v1.2$ and forming the fusion pore, and have been proposed to form a triad structure between one cysteine per $Ca_v1.2$ channel (Atlas, Marom and Cohen, 2007). The knockout of STX1A could thereby prevent the formation of the triad fusion pore, decreasing the channel's inward current and consequently inducing an abnormality in electromechanical signalling. The cysteine-residues may also be equally important in maintaining the structural integrity of $Ca_v1.2$ at the plasma membrane *via* disulfide bond formation, and decreased expression of STX1A would de-stabilize the tridimensional structure hence reducing normal $Ca_v1.2$ function (Arien et al., 2003).

During the event of CICR, RyR2s also play the pivotal role of inducing SR Ca^{2+} release which thereby gives rise to the cell wide Ca^{2+} transient. In the failing heart however, remodelling of the t-tubular structure can result in a loss of dyadic organization between LTCC-RyR2, reducing the pattern of synchronized SR Ca^{2+} release (Zima et al., 2017). It is hence suggested that if KO of STX1A reduces $Ca_v1.2$ cell-surface expression, a parallel loss in dyadic organization could further disrupt RyR2s coordinated property of SR Ca^{2+}-release. A consequent reduction in cytosolic Ca^{2+} levels would decrease the amplitude of the Ca^{2+} transient, which would induce weaker and reduced contractions of the myocardium. To add, the failing heart also demonstrates severe disruptions in RyR2 transcriptional expression, for instance in chronically paced dogs undergoing heart failure, patients experiencing ischemic cardiomyopathy, and hypertrophic remodeling in rat myocytes (Vatner et al., 1994; Naudin et al., 1991). Moreover, pathological remodelling in isolated rat myocytes has demonstrated an enlargement of cardiomyocyte size by two-fold with a reduction in RyR2 density by 55% (Naudin et al., 1991). An increase in cellular length with corresponding decline in RyR2 transcription – as reported post-STX1A KO – can severely impair the cytosolic Ca^{2+} levels required to maintain basal contractions, which was confirmed through speckle-tracking strain analysis (Figure 8, 9).

In the failing heart, resting levels of intracellular Ca^{2+} are elevated, the amplitude of intracellular Ca^{2+} is decreased, and the duration of Ca^{2+} transient is prolonged (del Monte et. al, 2002). These effects are a direct consequence of impaired SERCA2a activity which functions to restore Ca^{2+} balance during relaxation, and is inhibited during contraction *via* allosteric binding by Plb (Akin et al., 2013). In the failing heart however, mRNA transcription of both SERCA2a and Plb are reported to be significantly reduced by 54% and 41% in human cardiomyocytes (Schwinger et al., 1995). To add, a parallel relationship between SERCA2a and RyR2

downregulation has been elucidated, with RyR2 levels decreasing by the same magnitude as SERCA2a under hypertrophic conditions (Naudin et al., 1991). These findings coincide with the current results, as heterozygous KO of STX1A elicited a 75%/66% reduction in RyR2/SERCA2a levels respectively, while homozygous KO elicited an 85%/82% reduction.

4.5 Mechanism of STX1A KO induced alterations in E-C gene transcription

4.5.1 Alterations in E-C Gene Transcription: Ca^{2+} Handling

The current study utilizes a tamoxifen-inducible Cre approach to drive spatio-temporal excision of exons 2 and 3 of the STX1A gene. The deletion of exons 2 and 3 is suggested to to form a truncated protein which may serve as an important trigger for the altered cardiac phenotype, particularly in correlation with the recent findings by Perl et al. (2022). Within their respective study, it was demonstrated that a 38-base pair deletion at exon 3 of STX4 – encoding for the regulatory N-terminus domain – induced severe depression in ventricular function within both patients and zebrafish models. Moreover, significant reductions in total Ca^{2+} flux and impaired Ca^{2+} handling was recorded with each cardiac cycle, denoting an important role of the syntaxin N-terminus in regulating Ca^{2+} homeostasis within cardiomyocytes (Perl et al., 2022).

The N-terminus plays great importance in the physiological role of syntaxins since they serve as the binding site of Munc-18. Although Munc-18 is normally recognized as an inhibitor of the SNARE mechanism, studies have demonstrated a crucial role of Munc-18 not only in supporting the stabilized SNARE complex, but also in regulating syntaxin expression (Toonen and Verhage, 2003). For instance, *null* Munc-18 expression has yielded a parallel decrease in STX1 levels, while heterozygous KO of STX4 demonstrated a 40% repression in Munc-18 levels

(Toonen and Verhage, 2003). Hence, since Munc-18 and syntaxin are expressed within a coordinated system, it can be suggested that cleavage of the N-terminus may disrupt the functional role of Munc-18 which inhibits the fusion of transport vesicles at their target sites (Toonen and Verhage, 2003). Moreover, since STX1A has shown to be important in delivering Ca^{2+} channels to the surface membrane and initiating Ca^{2+} flux (Grinstein et al., 2003), KO of its N-terminus could thereby prevent the delivery of LTCCs *(N)* to the t-tubular membrane, reducing the cytosolic Ca^{2+} flux.

A decline in inward Ca^{2+} current may have severe impact on the overall cardiac function, such as the observation of systolic dysfunction within our study. However, a much-lesser appreciated role of Ca^{2+} is its contribution to coupling excitation to the mechanism of gene transcription in cardiomyocytes (Satin, Schroder and Crump, 2011). Particularly, LTCCs demonstrate a specialized auto-regulatory property, whereby its auxiliary C-terminus domain is able to sense alterations in cytosolic Ca^{2+} levels, cleave from the protein, and translocate to the nucleus to regulate $Ca_v1.2$ gene transcription. For instance, under hypertrophic conditions – such as that suggested at week 0 in response to calcineurin-NFAT signalling – the $Ca_v1.2$ C-terminus is cleaved and interacts with the *can1ac* promoter, repressing the expression of $Ca_v1.2$ gene (Satin et al., 2011). In order to inhibit the hypertrophic response, the cardiomyocytes may sense a blockade or reduced $Ca_v1.2$ current by week 1, hence alleviating the inhibition of *can1ac* and thereby increasing $Ca_v1.2$ transcription (Satin et al., 2011).

It is suggested that due to the reduced cytosolic Ca^{2+} flux *via* LTCCs, the transcriptional demands of RyR2 may also be reduced to limit SERCA2a's functional role. In the hypertrophic heart, the reduced expression of SERCA2a can be beneficial as it uses 85-90% of the energy released *via* ATP hydrolysis to maintain the 10,000-fold Ca^{2+} gradient across the SR membrane

(Pinz et. al, 2011). If a reduction in LTCC expression occurs, RyR2 transcripts and protein expression may also be downregulated to reduce the cytosolic Ca^{2+} pool and consequently SERCA2a's activity within an already failing myocardium. Consequently, downregulation of cytosolic Ca^{2+} can impact many gene-signalling pathways, one of which includes the activation of Ca^{2+}/calmodulin kinase-II (CaMKII). CaMKII is an extremely crucial Ca^{2+} sensor and phosphatase which serves as an important regulator of basal cardiac function. One of the many roles of CaMKII includes phosphorylation of the transcription factor (TF) *cyclic-AMP response binding element* (CREB), which has shown to modulate the gene expression of RyR2 (Sleiman, Lacampagne, and Meli 2021). Therefore, it is hypothesized that due to reduced cytosolic Ca^{2+} levels induced as a result of STX1A haploinsufficiency, a reduction in CaMKII-mediated CREB activation may further reduce RyR2 transcription in response to lowered LTCC activity. CaMKII also serves as an important modulator of hypertrophic signalling by phosphorylating calcineurin and preventing NFAT translocation to the nucleus (Kreusser and Backs, 2014). Consequently, a reduction in CaMKII signalling will thereby cause nuclear NFAT translocation, hence activating hypertrophic gene signalling. Hypertrophic remodelling is linked with coordinated overexpression of the transcriptional factor *specificity protein 1* (sp1), which has demonstrated a ~85% downregulation in SERCA2a gene expression – a similar reduction to our homozygous KO model (82%) (Takizawa et al., 2003). Moreover, hypertrophic remodelling is also correlated with severe reductions in circulating thyroid hormones T3/T4, which can further reduce CaMKII activation and thereby transcription of Plb *via* the TF *thyroid response element* (TRE) (Pinz et. al, 2011).

Conclusively, it is proposed that formation of a truncated STX1A gene product, particularly *via* cleavage of the N-terminus coding region may alter intracellular Ca^{2+} dynamics

which further impacts Ca^{2+}-dependent signalling pathways. Moreover, it is suggested that no single pathway regulates the severe alteration in excitation-transcription as observed, but rather, crosstalk between numerous pathways in response to lower Ca^{2+} demands, cytosolic stress, and hypertrophic remodelling would activate certain transcription factors (i.e. CREB, sp1, TRE) to limit contractions of the myocardium. As the heart adapts to the volumetric overload *via* overexpression of ANP by week 3, inhibition of hypertrophic signalling may increase $Ca_v1.2$ gene transcription and translation, further raising levels of free-intracellular Ca^{2+} and CaMKII activity. A return in the contractile property of the heart as recorded *via* echocardiography would demand increased transcription of neighbouring Ca^{2+} handling genes (i.e. RyR2, SERCA2a, Plb) to modulate the elevated load and hence maintain Ca^{2+} homeostasis.

4.5.1 Alterations in E-C Gene Transcription: Non-functional STX1A gene/protein

Within our study, Cre's recombinase activity further ligates exons 1 with 4-10 hence forming a mutated STX1A gene. If the mutated product is unable to be translated, it can suggestively be categorized as a long non-coding RNAs (lncRNAs) due to having a length greater than 200 nucleotides (Statello et al., 2021). LncRNAs have demonstrated important roles in transcriptional and translational regulation, for instance, being able to suppress gene expression by directly interfering with the transcriptional machinery and preventing recruitment of TFs (Statello et al., 2021). Alternatively, it is suggested that if a truncated STX1A protein is translated, the possibility of endoplasmic reticulum (ER) stress can also take place. Elevated ER stress occurs as a result of improper protein folding or accumulation of a mutant product which can thereby activate the unfolded protein response (UPR). Through this mechanism, gene transcription and translation can both be modified in an attempt to re-establish homeostasis and prioritize restoration of ER function (Tsai and Weissmen, 2010). Collectively, it is hypothesized

that generation of a mutant STX1A product may also trigger a global alteration in transcriptional or translational expression of genes by either functioning as a lncRNA, or generating sufficient cytosolic stress to activate UPR signalling.

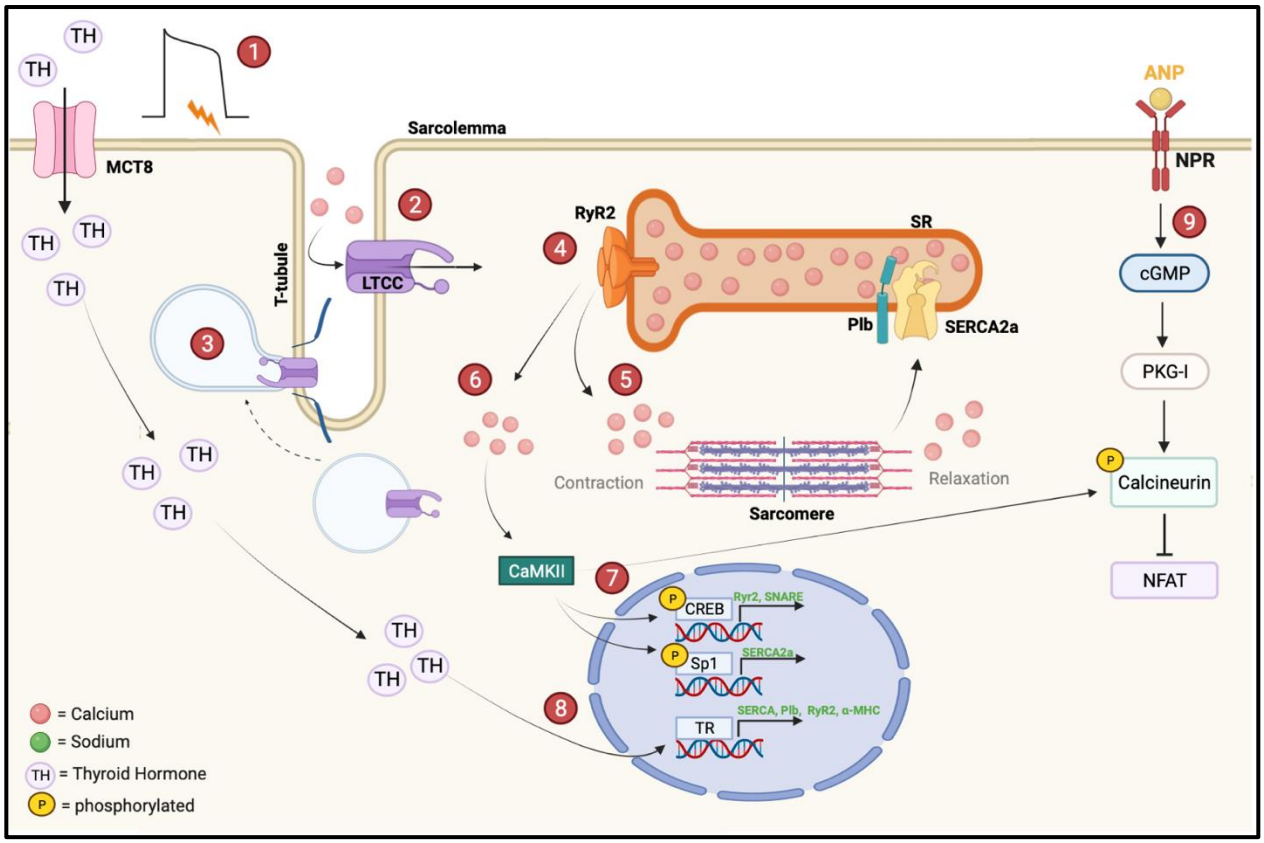

Figure 24: Suggested mechanism of STX1A mediated regulation of cardiac excitation-contraction coupling in ventricular cardiomyocytes. (1) Surface-level electrical propagation allows for activation of membrane-localized LTCCs **(2)**, but vesicular docking and fusion of LTCCs at the t-tubular membrane is dependent on basal STX1A expression *(blue)* **(3)**. Inward Ca^{2+} current mediates SR Ca^{2+} release **(4)** which induces contraction of the myocardium *via* interactions with the troponin-tropomyosin complex **(5)**. Elevated levels of cytosolic Ca^{2+} can further activate CaMKII signalling, resulting in phosphorylation of nuclear CREB and Sp1 to elevate E-C coupling and SNARE gene transcription **(7)**. At the same time, circulating levels of thyroid hormones can enter cardiomyocytes *via* the monocarboxylate transporter 8 (MCT8) and directly act on TR to maintain E-C coupling gene expression **(8)**. Continuous volume and pressure maintenance *via* ANP signalling, alongside elevated CaMKII activity also maintains NFAT in an inhibitory state, preventing nuclear translocation and hypertrophic signalling **(9)**. Illustration was created on www.biorender.com.

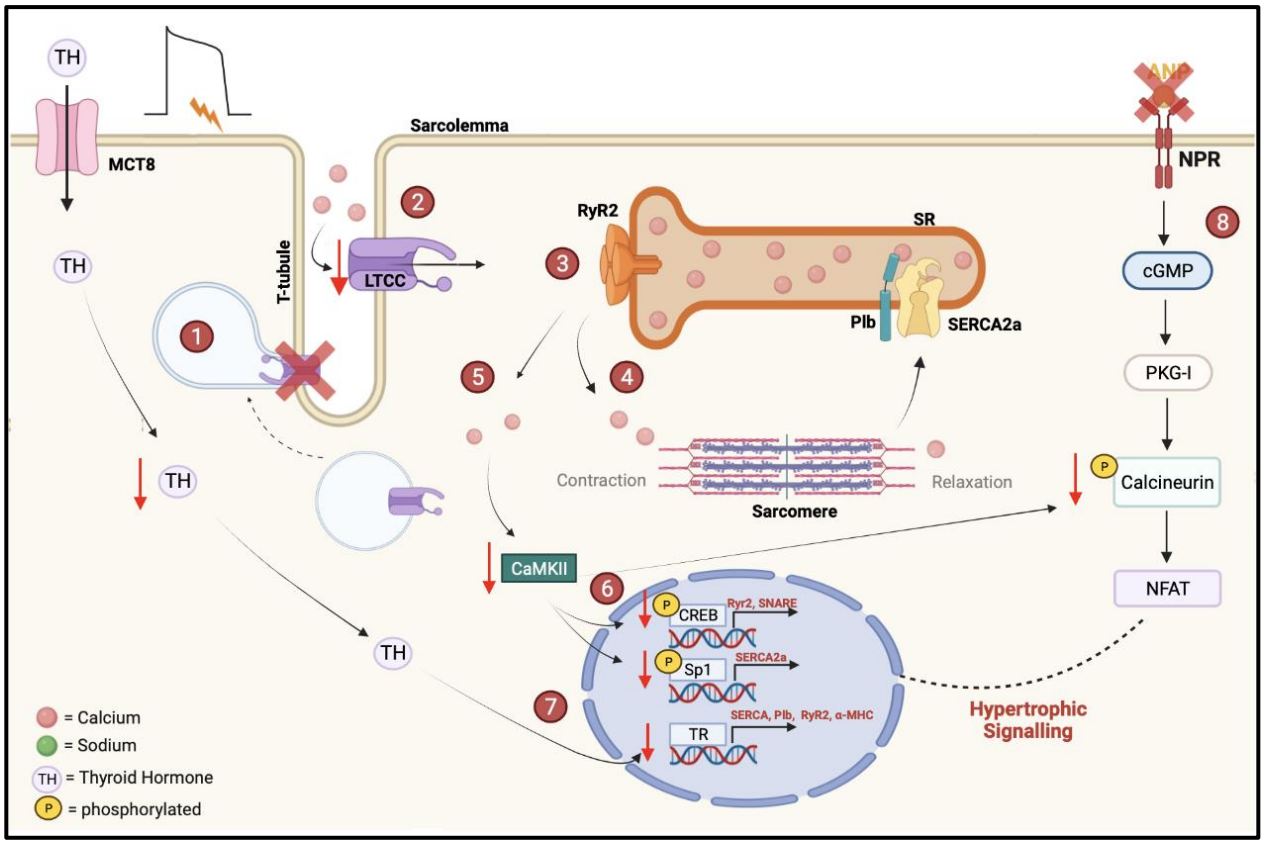

Figure 25: A proposed mechanism for STX1A knockout-induced disruption in cardiac excitation-contraction coupling. STX1A knockout reduces LTCC channel embedding at the t-tubular membrane **(1)**, consequently lowering the surface-level expression and inward Ca^{2+} current **(2).** Reduced Ca^{2+} spark event further decreases RyR2-mediated SR Ca^{2+} release **(3)**, resulting in weaker contractions of the myocardium **(4)** alongside reduced CaMKII activation **(5)**. Consequent reduction in CaMKII-mediated phosphorylation of CREB and Sp1 decreases transcriptional expression of both E-C coupling genes and SNARE proteins **(6)**, while also reducing level of calcineurin phosphorylation. A decrease in calcineurin phosphorylation coupled with ANP exocytosis due to impaired STX4 machinery allows for NFAT translocation and activation of hypertrophic gene signalling **(7)**. Hypertrophy is further associated with reduction in circulating thyroid hormone levels which prevents TR from increasing transcriptional expression of E-C coupling genes **(8)**. Illustration was created on www.biorender.com.

4.6 STX1A KO elicits electrical dyssynchrony of the left-ventricle

Speckle-tracking strain analysis was performed to assess for delays in electrical signal propagation induced by heterozygous and homozygous KO of STX1A. Upon analysis, haploinsufficiency of STX1A was shown to trigger significant delays in time required to reach peak strain within the mid and basal regions of the ventricular chambers (Figure 11, 12). It is well established that STX1A plays a major role in regulating the gating property of numerous cardiac ion-channels, including the transient outward K^+ channel ($I_{to;}$ $K_v4.2$) and human ether-à-go-go channel (hERG; $K_v11.1$) which participate in the repolarization phase of the cardiac AP (Kowalska, Nowaczyk and Nowaczyk, 2020). Under wild-type conditions, STX1A can bind to the N-terminus of $K_v4.2$ and reduce the current amplitude while accelerating the rate of recovery from deactivation (Yamakawa et al., 2011). Consequently, the quick and rapid channel kinetics of $K_v4.2$ may be tightly regulated by STX1A, giving rise to the short phase 1 of cardiac AP (Yamakawa et al., 2011). Upon heterozygous or homozygous KO of STX1A, it is suggested that reduced interaction with $K_v4.2$ may disrupt the channel's normal gating properties, preventing rapid recovery from the inactive state. Prolonged inactivation could therefore elicit a reduced I_{Kr}, preventing quick repolarization in cardiomyocytes which can prolong into the plateau phase, or phase 2 of the action potential (Mages et al., 2021). Such consequences of reduced $K_v4.2$ channel kinetics have been elucidated in mice with dilated cardiomyopathy (DCM), with an ~80% blockade in I_{to} eliciting a markedly slow phase 1, an elevated plateau phase, and prolonged action potential duration in the early-to-mid depolarization phase (Workman et al., 2012). Moreover, a decrease in $K_v4.2$ currents have also been recorded in DCM cardiomyocytes, along with a reduction in mRNA transcripts and protein expression (Mages et al., 2021). Since STX1A has also shown to modulate the transcription, channel trafficking, and insertion of $K_v4.2$ into the

plasma membrane (Yamakawa et. al, 2007), it is suggested that knockout of STX1A may impair the transcription and translation of $K_v4.2$ thereby inducing a delay in the electrical signalling cascade.

Although the mid and basal regions of the ventricle demonstrated a delay in signal propagation, the apex continued to remain synchronous in heterozygous and homozygous KO mice (Figure 11, 12). The apex is the initial site of signal transduction from the septum to the ventricle and is thereby required to undergo rapid conduction to initiate blood propulsion towards the aorta (Sengupta et al., 2006). Consequently, apex-to-base bias is apparent within the electrical propagation system, as signals initiate at the apical subendocardium and get progressively delayed as they reach the LV base (Sengupta et al., 2006). Utilization of high-resolution optical mapping has also revealed normal activation patterns of the apex in mice with DCM, while slower activation times were recorded as the signal proceeded towards the mid and basal regions of the ventricular chamber (Hall et al., 2000). A delay in electrical signal propagation can suggestively have occurred due to altered expression of connexin-43 (Cx43), which is the most abundant gap junctional channel expressed in cardiomyocytes (Michela et al., 2015). Under diseased settings such as hypertrophic cardiomyopathy, the expression of Cx43 is reduced, disrupting the maintenance of normal cardiac rhythm and electromechanical function of cardiomyocytes (Hall et al., 2004; Michela et al., 2004). Although a direct relationship between STX1A and Cx43 has not been elucidated to-date, SNARE complexes have shown to colocalize with Cx43, hence may play a vital role in their transportation to the PM (Cochrane et. al, 2013).

4.7 STX1A KO induces eccentric remodelling suggestively *via* NFAT-signalling

4.7.1 STX1A KO causes ventricular volume overload and cardiomyocyte elongation

The observation of reduced systolic function, electromechanical delays, and decrease in Ca^{2+}-handling gene expression was followed by a complete recovery in function three-weeks post-KO. To assess how the heart adapted to such elevated ventricular stress, the possibility of hypertrophic remodelling was explored. In cardiac hypertrophy, the myocyte shape and size are altered to withstand elevated pressure or volume in order to maintain basal cardiac output. Since heterozygous and homozygous KO of STX1A resulted in severe volume overload with no alterations in systolic/diastolic pressures (Virdi, 2020), the possibility of eccentric (volume overload) hypertrophy was assessed.

Hallmarks of eccentric remodelling include minimal to no increase in the ventricular wall thickness, disrupted intracellular Ca^{2+} handling, and increased length of cardiomyocytes to adapt to volume overload (Samak et al., 2016). Initially, Virdi (2020) reported no alterations in the ventricular wall thickness upon homozygous KO of STX1A which was consistent with the findings by Virdi (2022). Furthermore, the current thesis along with work by Virdi (2022) demonstrates a disruption in Ca^{2+} handling gene expression, with great emphasis on SERCA2a's downregulation which has been recognized as a severe trigger for hypertrophic remodelling. In physiological hypertrophy, levels of SERCA2a are either unchanged or elevated to account for the enhanced cardiac performance and energy utilization by the heart. Under pathological hypertrophy however, SERCA2a expression, protein function, and even Ca^{2+}-reuptake activity has shown to be reduced from 3.60 nmol/L to 1.94 nmol/L in the failing myocardium (Fragoso-Medina and Zarain-Herzberg, 2013; Sikkel et al., 2013, Pieske et al., 1995). Within the current thesis, homozygous KO of STX1A not only resulted in severe depression of SERCA2a transcript

levels, but also a higher Plb/SERCA2a ratio, implying that remaining SERCA2a is most likely inhibited by excess monomeric Plb (Sikkel et. al, 2013).

As previously suggested, a reduction in cytosolic Ca^{2+} levels and thereby CaMKII signalling could prevent phosphorylation of calcineurin, which is normally required to maintain NFAT in an inhibitory state (Kehat and Molkentin, 2010). Consequently, NFAT may be allowed to translocate to the nucleus where it can carry multiple roles, including: (1) activation of hypertrophic gene signalling, (2) induction of fetal-gene re-expression, and/or (3) coordination with MAPK proteins to induce elongation of cardiomyocytes (Kehat and Molkentin, 2010; Molkentin, 2004) The activation of calcineurin-NFAT demonstrates significant interest, as transgenic mice overexpressing calcineurin display a dramatic increase in heart size and severe ventricular dilation which was also observed post-STX1A KO (Nicol et. al, 2001). Moreover, cross-talk between NFAT and the MAPK signalling can induce eccentric hypertrophy specifically linked to pathological remodelling, for instance by decreasing the transverse cross-sectional area and elongating the cardiomyocyte shape which was specifically observed within the homozygous STX1A KO mice (Molkentin et al., 2015; Wilkins et al., 2004). Collectively, the results suggest a plausible role of the calcineurin-NFAT pathway in the hypertrophic response mediated by STX1A haploinsufficiency and should be further explored.

4.7.2 *STX1A KO causes elevated fibrosis of the LV at the mitral valve*

Another hallmark of pathological remodelling is fibrotic remodelling of the myocardium, whereby accumulation of extracellular matrix proteins within the cardiomyocyte interstitium can contribute to systolic or diastolic dysfunction (Kong, Christia and Frangogiannis, 2013). More specifically, volume overload of the ventricle, hypertrophic cardiomyopathy, and dilated

cardiomyopathy have all been linked with elevated non-collagenous matrix in the myocardium, alongside significant cardiac fibrosis (Kong, Christia and Frangogiannis, 2013). In the current analysis, both heterozygous and homozygous KO of STX1A resulted in elevated fibrosis at the left-ventricular free-wall and septum. However, only an increase in fibrosis at the mitral valve was deemed significant, demonstrating a 10.2% and 20.5% elevation in fibrotic area within heterozygous and homozygous KO mice.

Volume overload often occurs in response to mitral regurgitation or aortic regurgitation, whereby blood in the LV chamber cannot be delivered into systemic circulation. Instead, the blood is either retained in the LV chamber (aortic regurgitation) or generates sufficient pressure causing it to backflow into the left-atria (mitral regurgitation) (Muslin, 2012). Through histological analysis post-STX1A KO, increased backflow was indeed observed in the left-atria and identified by formation of an oedema and/or collection of red blood cells in the left-atria (Supplementary Figure 2). Moreover, end-stage analysis revealed an increase in the size of LA within heterozygous and homozygous KO mice, which may have overdistended to compensate for backflow and thereby maintenance of normal cardiac output (Figure 23 A, B).

As a consequence of elevated backload into the left-atria, induction of fibrosis can occur at the mitral valve due to increased mechanical stress on the papillary muscles (Morningstar et al., 2021). Support for elevated mechanical stress has been demonstrated by Imbre-Moore et al. (2021), revealing a greater than 5-fold increase in force development at the papillary muscles in patients with bileaflet prolapse. Moreover, the induction of fibrotic remodelling is suggested to occur in correlation with elevated stress particularly at the base of the ventricle (Morningstar et al., 2021). In our current study, KO of STX1A severely depressed the function of the ventricular base, which can result in blood overloading near the mitral valve and consequent regurgitation

into the LA. This is further supported by observation of blood coagulation in the LA, which may serve as a trigger for fibrosis induction at the mitral valve. Although a clear mechanism of stress-invoked fibrosis is not established to-date, it is suggested that mechanically-induced cell membrane deformation may trigger the release of cytokines, ions, or ATP which may impact all cell types in the affected areas of the mitral valve (i.e. cardiomyocytes, fibroblasts, inflammatory cells, and endothelial cells) (Heidt et al., 2014). Consequent release of proinflammatory and profibrotic markers by the respective cells may further act locally to induce collagen insertion, and thereby remodelling at the mitral valve (Morningstar et al., 2021).

4.7.3 STX1A KO causes activation of pathological fetal-gene reprogramming

For over 20 years, it has been well appreciated that a major hallmark of hypertrophic remodelling within rodents and patients is an increase in the expression of β-MHC with a parallel decrease in α-MHC (Barry, Davidson and Townsend, 2008). Due to each isoform having distinct enzymatic activities, the ratio of the two enzymes can greatly influence the overall cardiac function. In pathological remodelling, upregulation of β-MHC decreases the enzymatic velocity which consequently reduces the contractile rate in adjustment to elevated workload (Barry, Davidson and Townsend, 2008). Reversion of hypertrophy is recorded by an increase in α-MHC and subsequent decrease in β-MHC as observed in patients with DCM (Barry, Davidson and Townsend, 2008).

Within the current study, myosin isoform expression was assessed by taking the transcriptional ratio of β-MHC to α-MHC post STX1A-KO. At week 0, the ratio of β-MHC/α-MHC remained low within both KO groups, suggesting α-MHC as the primary isoform

expressed within the transgenic heart. Although a general shift towards the β-isoform does take place in pathological hypertrophy, expression of the α-MHC can advocate a beneficial effect in preserving heart function under stress-induced conditions. Through assessment on isolated rat myocyte fragments, Herron and McDonald (2008) demonstrated that cardiomyocytes which only expressed 12% of the total α-MHC generated a 52% greater power output than those expressing the β-MHC isoform. The findings have also been observed in rabbits which have a very similar MHC profile to humans (Gupta, 2007). Particularly, in rabbits with dilated cardiomyopathy, transgenic replacement of β-MHC with 40% α-MHC allowed for sustained return in heart function under stress conditions (James et al., 2005).

By week 3, a significant increase in β-MHC/α-MHC was observed within both heterozygous and homozygous KO mice, thereby appointing β-MHC as the predominant isoform. As suggested, activation of the calcineurin-NFAT pathway can result in hypertrophic response of the myocardium, whereby translocation of NFAT3 can increase the expression of a discrete set of genes including β-MHC (Molkentin et al., 1998). Accompanying the increase in β-MHC expression, it is suggested that activation of other fetal pathways may also occur at week 3, such as those involved in anti-apoptosis, cardioprotection and fatty acid oxidation. The collective return to a fetal metabolic gene profile could therefore serve as a key protective mechanism in STX1A KO hearts, and aid in the recovery of systolic function as observed at week 3 (Taegtmeyer, Sen and Vela, 2013).

The reversal of myosin isoform and return in α-MHC expression after cardiac stress has been elucidated within the diseased model. However, the reversal does not happen abruptly but rather as a slow progressive transition. For instance, in rats experiencing pressure-overload *via* aortic banding, activation of fetal-gene programming resulted in immediate induction of β-MHC

with simultaneous suppression of α-MHC (Gupta and Zak, 1992). After load removal and regression of hypertrophic remodelling, the α-MHC returned to normal levels immediately while β-MHC levels recovered very slowly and remained elevated even 7-weeks post-debanding (Gupta and Zak, 1992). These findings directly coincide with the current analysis, as although α-MHC expression returns to baseline by week 6, β-MHC continues to remain significantly higher and as the predominant isoform (Figure 21).

4.7.4 STX1A KO upregulates ANP expression to inhibit hypertrophic signalling?

Alongside a switch in myosin isoform expression, an important hallmark of fetal reprogramming is the expression of ANP within the ventricle which is primarily produced, stored, and secreted within the atria (Kessler-Icekson, 2002; Benvenuti et al., 1997). During elevated stress, ANP expression in the ventricle can demonstrate a dual role as a circulating hormone to lower pressure and volume-overload, and an autocrine/paracrine factor to inhibit cardiomyocyte hypertrophy *via* cyclic-GMP signalling (Tokudome, 2005). More specifically, the binding of ANP to its type 1 guanylase receptor (NPRA) activates intrinsic guanylase activity, significantly increasing the levels of cGMP (Airhart et al., 2003). Elevated cGMP results in phosphorylation and thereby activation of cGMP dependent protein-kinase (PGK-I), which maintains calcineurin in an inhibitory state thereby preventing NFAT translocation (Airhart et al., 2003; Gupta, 2007). Collectively, ANP plays an important role in inhibition against hypertrophic signalling, and it is well-established that release of ANP is regulated by the t-SNARE protein STX4. Therefore, the relationship between STX4 and ANP was also assessed as a possible trigger for hypertrophic remodelling.

Intriguingly, both heterozygous and homozygous KO of STX1A elicited a decline in the transcriptional expression of STX4 while a significant increase in ANP levels were recorded. The increase in ANP transcription could be a cardioprotective response from the myocardium in an attempt to lower the volumetric overload observed post-STX1A KO. However, a parallel decline in STX4 and VAMP expression as observed by Faizan (2022) (Supplementary Figure 1) would prevent the granular exocytosis of ANP, thereby inhibiting its ability to function as a diuretic hormone, alongside prevent NFAT translocation to the nucleus.

4.8 STX1A KO induces global reduction in SNARE expression

Within the current thesis alongside findings by Virdi (2022) and Faizan (2022), a reoccurring theme noted upon knockout of STX1A is decreased transcription of the total SNARE machinery. For instance, work by Faizan (2022) revealed reductions in transcriptional expression of the STX1A (STX1A/VAMP-2/SNAP-25) and STX4 complexes (STX4/VAMP-2/3/SNAP-23) upon haploinsufficiency of STX1A alone.

The SNARE-mediated fusion event involves membrane-associated SNAP-25 to interact with STX1A and VAMP-2 to create a stable, ternary core complex with 1:1:1 stoichiometry (Vardar et al., 2016). Consequently, any disruptions in the stoichiometric relationship impairs the functional role of its constituents, rendering them unusable within SNARE-mediated fusion. To add, the importance of STX1A within the stoichiometric relationship has been elucidated extensively, whereby its deletion in flies has yielded complete inhibition of neurotransmission accompanied by cell lethality (Vardar et al., 2016). Moreover, it has been demonstrated that loss of STX1 impairs the process of vesicular docking, priming and fusion, thereby making its role central within the SNARE machinery (Vardar et al., 2016). It is hence proposed that within our model, haploinsufficiency of STX1A may prevent the formation of a stabilized SNARE

complex, rendering the function and transcriptional expression of SNARE constituents to be significantly reduced. Moreover, since the process of SNARE-mediated exocytosis – particularly zippering of vesicles at a target membrane – serves as a large-energy barrier (Zhang, 2017), the hypertrophic heart experiencing systolic dysfunction will limit excess forms of energy expenditure; one of which may include reduced transcriptional and/or translational demands of the SNARE machinery. Consequently, channel-trafficking such as that of LTCCs to the t-tubular membrane could be reduced, hence giving rise to the lowered Ca^{2+} current and decreased CaMKII signalling as previously suggested. A reduction in CaMKII-mediated phosphorylation of nuclear CREB can also directly impair the transcriptional expression of the SNARE machinery, as CREB has shown to directly modulate SNARE transcription. Within a study involving RNA-sequencing analysis of genes activated by CREB within the rat cortex, it was revealed that out of all vesicle dynamic genes, VAMP2-5, SNAP-25, and STX1A were highly expressed under CREB control (Pardo et al., 2017). Although the studies were limited to the rat cortex, tight transcriptional regulation of SNARE genes *via* CREB may suggestively also be reduced within the heart in response to decreased CaMKII activity and should be further explored.

Additional factors which may impact the global downregulation in SNARE machinery surround the altered cytosolic Ca^{2+} levels upon STX1A KO. In our cardiomyocyte model which presents severe depression in contractility, the cardiomyocyte cannot allow excess efflux of Ca^{2+} as it will further depress the contractile strength of the myocardium. At the same time, the SNARE fusion machinery is reliant on Ca^{2+} efflux *via* membrane-localized voltage-gated Ca^{2+} channels which bind to synaptotagmin's C2A and C2B domains (Lai et al., 2014). In such

scenario, restricted efflux of Ca^{2+} could further inhibit the functional role and demand of the SNARE machinery as a whole, possibly lowering their transcriptional demands as observed.

Lastly, although a parallel relationship between STX1A and Munc-18 is established, it has also been shown that expression levels of STX4 and Munc-18 are tightly related, whereby knockdown of either constituent reduces the expression of the other protein within Madin-Darby canine kidney cells (Baumert et al., 2013). Therefore, it is plausible that a downregulation in STX4 as a parallel consequence of Munc-18 may further reduce the functional demand of its SNARE constituents VAMP-3/SNAP-23, hence reducing transcriptional activity of the entire SNARE complex. As the heart adapts to the volumetric overload and undergoes hypertrophic signalling, elevated cytosolic Ca^{2+} levels may increase the demand for: (1) synaptotagmin activity to mediate vesicular fusion, (2) LTCC channel-trafficking to the t-tubular membrane, and (3) increase in CaMKII signalling, which could collectively elevate CREB-mediated SNARE transcription hence demonstrating their return by week 3.

4.9 Sustained alteration in cardiac morphology at end-stage analysis

By week 6 or end-stage analysis, both male and female hearts demonstrate continued increase in heart weight alongside enlargement of atria and ventricles (Figure 23). It is well-established that patients with DCM do not demonstrate complete recovery in cardiac structure post-DCM, but rather, myocardial reversal remodelling is limited to 25-70% of patients (Tayal and Prasad, 2017). The elevated atrial and ventricular size may therefore remain sustained as the heart adapts to the new hemodynamic load to maintain both systolic and diastolic function. Conclusively, it is suggested that myocardial remission may occur at end-stage as opposed to myocardial recovery, since although normalization of myocardial and LV geometric changes takes place, it is uncertain if the heart is free from future failure events (Tayal and Prasad, 2017).

CHAPTER 5: CONCLUSION AND FUTURE REMARKS

5.1 Conclusion

In our study, the role of STX1A was explored utilizing an *in vivo* cardiomyocyte-specific KO model, demonstrating severe depression in cardiac dysfunction within male and female mice post-KO in all myocytes of the heart. Moreover, the KO elicited global reduction in ventricular contractility, accompanied by electrical delays which dispersed throughout the mid and basal regions of the myocardium. A delay between ventricular depolarization and contraction hint at the possibility of excitation-contraction uncoupling induced by STX1A haploinsufficiency, resulting in reduced inotropic force of the heart. Consequent volume overloading of the ventricle triggered a mechanism for myocardial remodelling – suggestively through calcineurin-NFAT signalling – which resulted in elevated cardiomyocyte length, decreased total CSA, and increased fibrotic deposition particularly at the mitral valve. Accompanying the respective markers, elevation in β-MHC and ANP transcription within the left-ventricle are suggested to activate the mechanism of fetal-gene reprogramming in order to reduce volume-overload induced stress on the myocardium. Collectively, the results suggest an important role of STX1A in regulating the electromechanical function of the intact murine heart, whereby KO disrupts the contractile mechanism and suggestively induces eccentric remodelling to adapt to the transient volumetric overload.

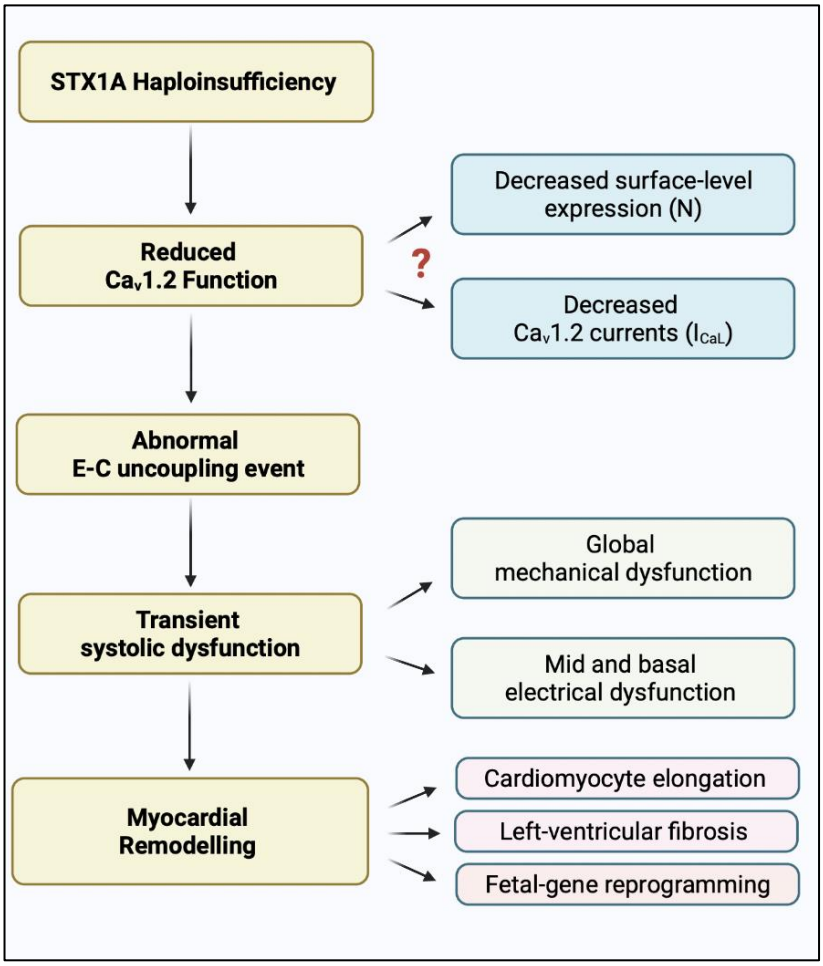

Figure 26: Summarized representation of phenotype induced by STX1A haploinsufficiency, alongside responses activated to maintain normal cardiac function. Illustration was created on www.biorender.com.

5.2 Future Research Projects

5.2.1 E-C Coupling Protein Expression and Channel Activity

Within the current study, a heavy emphasis was placed on understanding alterations in intracellular Ca^{2+} dynamics through changes in gene expression. However, it is well-established that levels of steady-state mRNA cannot be assumed as predictors of protein content, particularly since only a ~40% change in protein expression can be explained at the transcriptional level (de Sousa Abreu et al., 2009). Consequently, severe differences may arise between rates of mRNA processing, translation, post-translational modifications, and the rate at which proteins are synthesized and degraded (Schmidt et al., 1999). This is often observed within the failing myocardium, for instance in patients with heart failure demonstrating significantly reduced RyR2, SERCA2a, and Plb mRNA levels, yet the functional role of RyR2 is retained (Schmidt et al., 1999). Therefore, it is suggested that the protein expression of each Ca^{2+}-handling gene studied should be assessed *via* Western blotting to confirm if reduced gene expression further translates to protein expression. Intriguingly however, it has also been reported that severe depression at the transcriptional level is not always representative of protein expression within failing hearts. For instance, Schwinger et al. (1995) reported a significant decrease in SERCA2a and Plb mRNA expression within DCM hearts, no alteration in protein expression, yet significant reduction in ATPase activity. Therefore, if protein expression studies do not correlate with transcript levels, it is suggested that individual channel activity – particularly SERCA2a since it is a major mediator of hypertrophic remodelling – may also be assessed, for instance through fractionation and separation of the SR followed by spectrophotometric analysis for rates of NADH oxidation (Schwinger et al., 1995).

5.2.2 Ca^{2+} Imaging and Optical Mapping

The severe reduction in contractility observed post-STX1A KO directly appoints to the possibility of altered intracellular Ca^{2+} dynamics which can be best assessed *via* whole-cell Ca^{2+} transient measurements. As suggested in correlation with DCM hearts, KO of STX1A may impair the cytosolic Ca^{2+} balance thereby resulting in reduced SR Ca^{2+} release (lower amplitude) and prolonged duration of Ca^{2+} transient. In order to perform such assessments, a specialized Langendorff-retrograde perfusion system is utilized to isolate viable adult cardiomyocytes, loaded with a fluorescent Ca^{2+}-dye, and a fluorescent-imaging system is utilized to measure the absorbance/emission spectra of the dye. Initial efforts were made to perform Ca^{2+}-transient assessments at the beginning of the Master's study, and there was success in isolating viable adult cardiomyocytes. However, since alterations in Ca^{2+} handling was not demonstrated through RT-qPCR or Western blotting, the rationale for conducting Ca^{2+} imaging was not justified at such early stage. Since it is now demonstrated that Ca^{2+} handling gene expression is severely depressed, Ca^{2+}-imaging should be revisited to confirm alterations in intracellular dynamics as a consequence of STX1A haploinsufficiency.

Another approach that can be highly beneficial in assessing the altered electromechanical function observed post-KO is whole-heart optical mapping. Unlike Ca^{2+} imaging on isolated myocytes, whole-heart optical mapping allows for assessment of calcium transients with simultaneous recordings of action potentials (O'Shea et al., 2020). Hence, through use of fluorescent dyes, optical mapping can directly image the electrical function of the heart at a very high spatio-temporal resolution (O'Shea et al., 2020). Consequent disruptions in whole-heart dynamics can thereby aid in detection of disturbances in the electrical signal propagation,

generation of arrhythmias, and confirm the disruption in electromechanical function as suggested post-STX1A KO. Moreover, if conduction block is observed between the mid and basal regions of the heart, the findings would coincide with the speckle-tracking results and thereby highlight the importance of basal STX1A expression in electromechanical conduction.

5.2.3 Confirming the Activation of Fetal-gene Reprogramming

The pilot study demonstrates an important property of the heart in adjusting to hemodynamic volume overload *via* morphological remodelling in order to sustain basal cardiac output. However, due to limitations in sample size for histological analysis (n = 2 per group) and use of female mice only, it is imperative to repeat the findings in a larger cohort and incorporate male counterparts as well. Upon conformation of cardiac remodelling within a larger study group, experiments should be carried out to further elucidate the phenomena of fetal-gene reprogramming as a result of STX1A KO. Firstly, the switch in α-MHC to β-MHC isoform should be confirmed through Western blotting, and use of monoclonal antibodies have shown to be highly beneficial in revealing a clear switch in myosin isoform under failing conditions (Miyata et al., 2000). Furthermore, the current findings demonstrate significant elevation in β-MHC transcription at end-stage analysis, thereby questioning the timepoint where the heart reverts back to the α-MHC isoform. By increasing the length of the study (i.e., current 6-weeks to 12-weeks), we can not only determine the time-point of reversal to α-MHC, but also determine if KO of STX1A demonstrates any long-term cardiac and physiological effects in the adult mice. In the absence of future events of heart failure events, we can thereby conclude that the heart undergoes myocardial recovery and not remission upon STX1A KO.

Alongside myosin-switch, another factor that needs to be further clarified is the elevation in ANP levels observed post-KO. Normally, the formation of ANP occurs within cardiomyocytes under chamber distention, whereby larger peptide precursors (pre-pro ANP) are cleaved into the active form of ANP (pro-ANP) (Klabunde, 2019). In our current analysis, the KO of STX1A revealed significant elevation in the transcription of ANP in the LV free-wall at week 0 and week 3, however it does not demonstrate which form of ANP is being transcribed, translated, or secreted into circulation. To address this, pro-ANP levels should specifically be assessed utilizing an enzyme-linked immunoabsorbant assay (ELISA). More specifically, LV primary cardiomyocytes can be isolated and cultured in endothelin to induce ANP release *via* mechanical stretch (Ferlito et al., 2010), and the serum can be collected to quantify levels of pro-ANP.

5.2.4 Assessing CaMKII Activity and NFAT-signalling

It was suggested that upon knockout of STX1A, a reduction in vesicular transportation and thereby expression of LTCCs would reduce cytosolic Ca^{2+} flux, which further decreases the activity of CaMKII. To thereby uncover the cellular mechanism associated with STX1A KO induced excitation transcriptional downregulation, it is imperative to perform an assessment for CaMKII activity. Traditional methods including immunocytochemistry and Western blotting can indeed be applied to understand CaMKII activity initially, however the results are highly restricted to snapshot measurements (Despa et al., 2014). Rather, the Hayashi group developed a fluorescence energy-based transfer (FRET) biosensor known as Camui which functions as an excellent assessor of CaMKII activation *via* endogenous Ca^{2+} (Despa et al., 2014). Camui is a full-length kinase linked with yellow fluorescent protein (YFP) and cyan fluorescent protein (CFP) on the regulatory and catalytic site of the kinase respectively and hence, ratios of

YFP/CFP fluorescence can dictate levels of CaMKII activity (Despa et al., 2014). Elevated CaMKII activity can thereby be represented by reduced YFP/CFP ratios *via* confocal microscopy, while reduced CaMKII activity is represented by elevated YFP/CFP ratios. Therefore, it is proposed that utilization of the FRET-Camui mechanism will allow for a direct readout of the active conformation of the kinase and hypothesized to demonstrate elevated YFP/CFP ratios as a consequence of reduced free-cytosolic Ca^{2+} levels post-STX1A KO.

The activation of NFAT was also suggested to occur in response to downregulated CaMKII signalling and ANP secretion. To further assess this claim, Western blotting should be conducted to initially confirm the downregulation of STX4, VAMP-3 and SNAP-23, which collectively mediate ANP exocytosis. However, since it has also been elucidated that STX1A demonstrates a role in ANP secretion within both atrial and ventricular myocytes (Natividad, 2014), its haploinsufficiency may alone prevent appropriate ANP exocytosis. To consequently assess whether the calcineurin-NFAT pathway is upregulated in response to STX1A KO, Western blotting for calcineurin and dephosphorylated form of NFAT should be conducted progressively into the end-stages as the heart returns to basal function (Molkentin, 2004).

References

Ahlijanian, M. K., Westenbroek, R. E., amd Catterall, W. A. (1990). Subunit structure and localization of dihydropyridine-sensitive calcium channels in mammalian brain, spinal cord, and retina. *Neuron*, *4*(6), 819-832.

Aird, W. C. Discovery of the cardiovascular system: from Galen to William Harvey., 118-29 (2011).

Airhart, N., Yang, Y. F., Roberts, C. T., and Silberbach, M. (2003). Atrial natriuretic peptide induces natriuretic peptide receptor-cGMP-dependent protein kinase interaction. *Journal of Biological Chemistry*, *278*(40), 38693-38698.

Akin, B. L., Hurley, T. D., Chen, Z., and Jones, L. R. (2013). The structural basis for phospholamban inhibition of the calcium pump in sarcoplasmic reticulum. *Journal of Biological Chemistry*, *288*(42), 30181-30191.

Alvarez, O., Gonzalez, C., and Latorre, R. (2002). Counting channels: a tutorial guide on ion channel fluctuation analysis. *Advances in physiology education*, *26*(4), 327-341.

Andrews, T. G., Lindsey, M. L., Lange, R. A., and Aune, G. J. (2014). Cardiac assessment in pediatric mice: strain analysis as a diagnostic measurement. *Echocardiography*, *31*(3), 375-384.

Arackal, A., and Alsayouri, K. (2019). Histology, heart.

Aranega, A. E., de la Rosa, A. J., and Franco, D. (2012). Cardiac conduction system anomalies and sudden cardiac death: insights from murine models. *Frontiers in physiology*, *3*, 211.

Arien, H., Wiser, O., Arkin, I. T., Leonov, H., and Atlas, D. Syntaxin 1A modulates the voltage-gated L-type calcium channel ($Ca_V1.2$) in a cooperative manner. *Journal of Biological Chemistry.* 278, 29231–39 (2003).

Atlas, D. (2014). Voltage-gated calcium channels function as Ca^{2+}-activated signaling receptors. *Trends in biochemical sciences*, *39*(2), 45-52.

Barry, S. P., Davidson, S. M., and Townsend, P. A. (2008). Molecular regulation of cardiac hypertrophy. *The international journal of biochemistry & cell biology*, *40*(10), 2023-2039.

Baumert, M., Maycox, P. R., Navone, F., De Camilli, P., and Jahn, R. Synaptobrevin: an integral membrane protein of 18,000 daltons present in small synaptic vesicles of rat brain. *EMBO J, 8*(10), 379-384.

Becker, J. B., Prendergast, B. J., and Liang, J. W. (2016). Female rats are not more variable than male rats: a meta-analysis of neuroscience studies. *Biology of sex differences*, *7*(1), 1-7.

Beery, A. K. (2018). Inclusion of females does not increase variability in rodent research studies. *Current opinion in behavioral sciences*, *23*, 143-149.

Bennett, M. K., Calakos, N., and Scheller, R. H. Syntaxin: a synaptic protein implicated in Science. 1992, *10*, 257-255

Bennett MK, Garcia-Arraras JE, Elferink LA, Peterson K, Fleming AM, Hazuka CD, Scheller RH: The syntaxin family of vesicular transport receptors. Cell. 1993, *74:* 863-873.

Benvenuti, L. A., Aiello, V. D., de Lourdes Higuchi, M., and Palomino, S. A. P. (1997). Immunohistochemical expression of atrial natriuretic peptide (ANP) in the conducting system and internodal atrial myocardium of human hearts. *Acta histochemica*, *99*(2), 187-193.

Bers, D. M. Cardiac excitation–contraction coupling. *Nature* 415,198–205 (2002).

Bersell, K., Choudhury, S., Mollova, M., Polizzotti, B. D., Ganapathy, B., Walsh, S., ... and Kühn, B. (2013). Moderate and high amounts of tamoxifen in αMHC-MerCreMer mice induce a DNA damage response, leading to heart failure and death. *Disease models & mechanisms*, *6*(6), 1459-1469.

Block, M. R., Glick, B. S., Wilcox, C. A., Wieland, F. T., and Rothman, J. E. (1988). Purification of an N-ethylmaleimide-sensitive protein catalyzing vesicular transport. *Proceedings of the national academy of sciences*, *85*(21), 7852-7856.

Bock, J. B., and Scheller, R. H. (1999). SNARE proteins mediate lipid bilayer fusion. *Proceedings of the National Academy of Sciences*, *96*(22), 12227-12229.

Bowen, R. (2018). Atrial Natriuretic Hormone. *VIVO Pathophysiology*

Burgess, R. W., Deitcher, D. L., and Schwarz, T. L. (1997). The synaptic protein syntaxin1 is required for cellularization of Drosophila embryos. *The Journal of cell biology*, *138*(4), 861-875.

Bezprozvanny, I., Scheller, R. H., and Tsien, R. W. (1995). Functional impact of syntaxin on gating of N-type and Q-type calcium channels. *Nature*, *378*(6557), 623-626.

Chao, C. C., Mihic, A., Tsushima, R. G., and Gaisano, H. Y. (2011). SNARE protein regulation of cardiac potassium channels and atrial natriuretic factor secretion. *Journal of molecular and cellular cardiology*, *50*(3), 401-407.

Chen, X., Piacentino III, V., Furukawa, S., Goldman, B., Margulies, K. B., and Houser, S. R. (2002). L-type Ca^{2+} channel density and regulation are altered in failing human ventricular myocytes and recover after support with mechanical assist devices. *Circulation research*, *91*(6), 517-524.

Cheng, H., and Lederer, W. J. (2008). Calcium sparks. *Physiological reviews*, *88*(4), 1491-1545.

Christoffels, V. M., and Moorman, A. F. (2009). Development of the cardiac conduction system: why are some regions of the heart more arrhythmogenic than others?. *Circulation: Arrhythmia and electrophysiology*, *2*(2), 195-207.

Chu, P. Y., Joshi, M. S., Horlock, D., Kiriazis, H., and Kaye, D. M. (2019). CXCR4 antagonism reduces cardiac fibrosis and improves cardiac performance in dilated cardiomyopathy. *Frontiers in Pharmacology*, *10*, 117.

Cochrane, K., Su, V., and Lau, A. F. (2013). The connexin43-interacting protein, CIP85, mediates the internalization of connexin43 from the plasma membrane. *Cell Communication & Adhesion*, *20*(3-4), 53-66.

Coelho-Filho, O. R., Shah, R. V., Mitchell, R., Neilan, T. G., Moreno Jr, H., Simonson, B., and Jerosch-Herold, M. (2013). Quantification of cardiomyocyte hypertrophy by cardiac magnetic resonance: implications for early cardiac remodeling. *Circulation*, *128*(11), 1225-1233.

Cohen, R., Marom, M., and Atlas, D. (2007). Depolarization-evoked secretion requires two vicinal transmembrane cysteines of syntaxin 1A. *PLoS one*, *2*(12), e1273.

del Monte, F., Harding, S. E., Dec, G. W., Gwathmey, J. K., and Hajjar, R. J. (2002). Targeting phospholamban by gene transfer in human heart failure. *Circulation*, *105*(8), 904-907.

de Sousa Abreu, R., Penalva, L. O., Marcotte, E. M., and Vogel, C. (2009). Global signatures of protein and mRNA expression levels. *Molecular BioSystems*, *5*(12), 1512-1526.

Despa, S., Shui, B., Bossuyt, J., Lang, D., Kotlikoff, M. I., & Bers, D. M. (2014). Junctional cleft [Ca2+] i measurements using novel cleft-targeted Ca2+ sensors. *Circulation research*, *115*(3), 339-347.

Dos Santos, P. B., Simões, R. P., da L Goulart, C., Roscani, M. G., Marinho, R. S., Camargo, P. F., ... and Borghi-Silva, A. (2021). Eccentric left ventricular hypertrophy and left and right cardiac function in chronic heart failure with or without coexisting COPD: Impact on exercise performance. *International Journal of Chronic Obstructive Pulmonary Disease*, *16*, 203.

Dirkx, E., da Costa Martins, P. A., and De Windt, L. J. (2013). Regulation of fetal gene expression in heart failure. *Biochimica et Biophysica Acta (BBA)-Molecular Basis of Disease*, *1832*(12), 2414-2424.

Draper, M. and Hodge, A. (1949). Studies on muscle with the electon microscope. *Australian Journal of Experimental Biology and Medical Science.* 27, 465–504.

Dulubova, I., Khvotchev, M., Liu, S., Huryeva, I., Südhof, T. C., and Rizo, J. (2007). Munc18-1 binds directly to the neuronal SNARE complex. *Proceedings of the National Academy of Sciences*, *104*(8), 2697-2702.

Eghbali, M., Deva, R., Alioua, A., Minosyan, T. Y., Ruan, H., Wang, Y., ... and Stefani, E. (2005). Molecular and functional signature of heart hypertrophy during pregnancy. *Circulation research*, *96*(11), 1208-1216.

Faizan, M. (2022). Determining compensatory changes in the mRNA expressions of SNARE and excitation-contraction coupling proteins in heart-specific syntaxin-1A knockout mice. York University.

Ferlito, M., Fulton, W. B., Zauher, M. A., Marbán, E., Steenbergen, C., and Lowenstein, C. J. (2010). VAMP-1, VAMP-2, and syntaxin-4 regulate ANP release from cardiac myocytes. *Journal of molecular and cellular cardiology*, *49*(5), 791-800.

Fragoso-Medina, J., and Zarain-Herzberg, A. (2014). SERCA2a: its role in the development of heart failure and as a potential therapeutic target. *Research Reports in Clinical Cardiology*, *5*, 43-55.

Freire, G., Ocampo, C., Ilbawi, N., Griffin, A. J., and Gupta, M. (2007). Overt expression of AP-1 reduces alpha myosin heavy chain expression and contributes to heart failure from chronic volume overload. *Journal of molecular and cellular cardiology*, *43*(4), 465-478.

Friel, D. (2004). Interplay between ER Ca^{2+} uptake and release fluxes in neurons and its impact on $[Ca^{2+}]$ dynamics. Biological research, 37(4), 665-674.

Goda, Y. (1997). SNAREs and regulated vesicle exocytosis. *Proceedings of the National Academy of Sciences*, *94*(3), 769-772.

Goonasekera, S. A., Hammer, K., Auger-Messier, M., Bodi, I., Chen, X., Zhang, H., ... and Molkentin, J. D. (2012). Decreased cardiac L-type Ca^{2+} channel activity induces hypertrophy and heart failure in mice. *The Journal of clinical investigation*, *122*(1), 280-290.

Guo, A., Zhang, X., Iyer, V. R., Chen, B., Zhang, C., Kutschke, W. J., ... and Song, L. S. (2014). Overexpression of junctophilin-2 does not enhance baseline function but attenuates heart failure development after cardiac stress. *Proceedings of the National Academy of Sciences*, *111*(33), 12240-12245.

Gupta, M. P. (2007). Factors controlling cardiac myosin-isoform shift during hypertrophy and heart failure. *Journal of molecular and cellular cardiology*, *43*(4), 388-403.

Gupta, M., and Zak, R. (1992). Reversibility of load-induced changes in myosin heavy chain gene expression. *American Journal of Physiology-Regulatory, Integrative and Comparative Physiology*, *262*(3), R346-R349.

Gustavsson, M., Verardi, R., Mullen, D. G., Mote, K. R., Traaseth, N. J., Gopinath, T., and Veglia, G. (2013). Allosteric regulation of SERCA by phosphorylation-mediated conformational shift of phospholamban. *Proceedings of the National Academy of Sciences*, *110*(43), 17338-17343.

Hajar, R. Coronary heart disease: From mummies to 21st century. *journal of the Gulf Heart Association* 18

Hall, D. G., Morley, G. E., Vaidya, D., Ard, M., Kimball, T. R., Witt, S. A., and Colbert, M. C. (2000). Early onset heart failure in transgenic mice with dilated cardiomyopathy. *Pediatric research*, *48*(1), 36-42.

Han, J., Pluhackova, K., and Böckmann, R. A. (2017). The multifaceted role of SNARE proteins in membrane fusion. *Frontiers in physiology*, *8*, 5.

Hänggi, E., Grundschober, A. F., Leuthold, S., Meier, P. J., and St-Pierre, M. V. (2006). Functional analysis of the extracellular cysteine residues in the human organic anion transporting polypeptide, OATP2B1.17.

Hayashi, D., Kudoh, S., Shiojima, I., Zou, Y., Harada, K., Shimoyama, M., ... and Komuro, I. (2004). Atrial natriuretic peptide inhibits cardiomyocyte hypertrophy through mitogen-activated protein kinase phosphatase-1. *Biochemical and biophysical research communications*, *322*(1), 310-319.

Heidt, T., Courties, G., Dutta, P., Sager, H. B., Sebas, M., Iwamoto, Y., ... and Nahrendorf, M. (2014). Differential contribution of monocytes to heart macrophages in steady-state and after myocardial infarction. *Circulation research*, *115*(2), 284-295.

Heinen, A., Gödecke, S., Flögel, U., Miklos, D., Bottermann, K., Spychala, A., and Gödecke, A. (2021). 4-hydroxytamoxifen does not deteriorate cardiac function in cardiomyocyte-specific MerCreMer transgenic mice. *Basic research in cardiology*, *116*(1), 1-14.

Herron, T. J., and McDonald, K. S. (2002). Small amounts of α-myosin heavy chain isoform expression significantly increase power output of rat cardiac myocyte fragments. *Circulation research*, *90*(11), 1150-1152.

Hill, A. V. (1949). The abrupt transition from rest to activity in muscle. *Proceedings of the Royal Society B: Biological Sciences.*. 136, 399–420.

Hong, T., and Shaw, R. M. (2017). Cardiac T-tubule microanatomy and function. *Physiological reviews*, *97*(1), 227-252.

Huang, J., Min Lu, M., Cheng, L., Yuan, L. J., Zhu, X., Stout, A. L., ... and Parmacek, M. S. (2009). Myocardin is required for cardiomyocyte survival and maintenance of heart function. *Proceedings of the National Academy of Sciences*, *106*(44), 18734-18739.

Imbrie-Moore, A. M., Paulsen, M. J., Zhu, Y., Wang, H., Lucian, H. J., Farry, J. M., ... and Woo, Y. J. (2021). A novel cross-species model of Barlow's disease to biomechanically analyze repair techniques in an ex vivo left heart simulator. *The Journal of Thoracic and Cardiovascular Surgery*, *161*(5), 1776-1783.

Issa, Z. F., Miller, J. M., and Zipes, D. P. (2009). *Clinical arrhythmology and electrophysiology: a companion to Braunwald's heart disease*. Elsevier Health Sciences.

Iwase, M., Bishop, S. P., Uechi, M., Vatner, D. E., Shannon, R. P., Kudej, R. K., ... and Vatner, S. F. (1996). Adverse effects of chronic endogenous sympathetic drive induced by cardiac Gsα overexpression. *Circulation research*, *78*(4), 517-524.

James, J., L., Krenz, M., Quatman, C., Jones, F., Klevitsky, R., ... and Robbins, J. (2005). Forced expression of α-myosin heavy chain in the rabbit ventricle results in cardioprotection under cardiomyopathic conditions. *Circulation*, *111*(18), 2339-2346.

Kehat, I., and Molkentin, J. D. (2010). Molecular pathways underlying cardiac remodeling during pathophysiological stimulation. *Circulation*, *122*(25), 2727-2735.

Kessler-Icekson, G., Barhum, Y., Schaper, J., Schaper, W., Kaganovsky, E., and Brand, T. (2002). ANP expression in the hypertensive heart. *Experimental & Clinical Cardiology*, *7*(2-3), 80.

Klabunde, R. (2019). Electrocardiogram (EKG, ECG). *Cardiovascular Physiology Concepts.*

Klabunde, R. (2019). Natriuretic Peptides and Neprilysin Inhibitors. *Cardiovascular Physiology Concepts.*

Kloepper, T. H., Kienle, C. N., and Fasshauer, D. (2007). An elaborate classification of SNARE proteins sheds light on the conservation of the eukaryotic endomembrane system. *Mol. Biol. Cell.* 18, 3463–3471. doi: 10.1091/mbc.E07-03-019.

Koitabashi, N., Bedja, D., Zaiman, A. L., Pinto, Y. M., Zhang, M., Gabrielson, K. L., ... and Kass, D. A. (2009). Avoidance of transient cardiomyopathy in cardiomyocyte-targeted tamoxifen-induced MerCreMer gene deletion models. *Circulation research*, *105*(1), 12-15.

Kong, P., Christia, P., and Frangogiannis, N. G. (2014). The pathogenesis of cardiac fibrosis. *Cellular and molecular life sciences*, *71*(4), 549-574.

Kopecky, B. J., Liang, R., and Bao, J. (2014). T-type calcium channel blockers as neuroprotective agents. *Pflügers Archiv-European Journal of Physiology*, *466*(4), 757-765.

Kowalska, M., Nowaczyk, J., and Nowaczyk, A. (2020). KV11. 1, NaV1. 5, and CaV1. 2 Transporter Proteins as Antitarget for Drug Cardiotoxicity. *International Journal of Molecular Sciences*, *21*(21), 8099.

Krenz, M., and Robbins, J. (2004). Impact of beta-myosin heavy chain expression on cardiac function during stress. *Journal of the American College of Cardiology*, *44*(12), 2390-2397.

Kreusser, M. M., and Backs, J. (2014). Integrated mechanisms of CaMKII-dependent ventricular remodeling. *Frontiers in pharmacology*, *5*, 36.

Lai, Y., Lou, X., Wang, C., Xia, T., and Tong, J. (2014). Synaptotagmin 1 and Ca^{2+} drive trans SNARE zippering. *Scientific reports*, *4*(1), 1-8.

Lalande, S., and Johnson, B. D. (2008). Diastolic dysfunction: a link between hypertension and heart failure. *Drugs of today (Barcelona, Spain: 1998)*, *44*(7), 503.

Li, S., Nguyen, N. U. N., Xiao, F., Menendez-Montes, I., Nakada, Y., Tan, W. L. W., ... and Sadek, H. A. (2020). Mechanism of eccentric cardiomyocyte hypertrophy secondary to severe mitral regurgitation. *Circulation*, *141*(22), 1787-1799.

Li, Q., Yao, Y., Shi, S., Zhou, M., Zhou, Y., Wang, M., ... and Tu, X. (2020). Inhibition of miR-21 alleviated cardiac perivascular fibrosis via repressing EndMT in T1DM. *Journal of cellular and molecular medicine*, *24*(1), 910-920.

Lindsey, M. L., Kassiri, Z., Virag, J. A., de Castro Brás, L. E., and Scherrer-Crosbie, M. (2018). Guidelines for measuring cardiac physiology in mice. *American Journal of Physiology-Heart and Circulatory Physiology*, *314*(4), H733-H752.

Lipscombe, D., Helton, T. D., and Xu, W. (2004). L-type calcium channels: the low down. *Journal of neurophysiology*, *92*(5), 2633-2641.

Lipskaia, L., Chemaly, E. R., Hadri, L., Lompre, A. M., and Hajjar, R. J. (2010). Sarcoplasmic reticulum Ca^{2+} ATPase as a therapeutic target for heart failure. *Expert opinion on biological therapy*, *10*(1), 29-41.

Low, L. A., Bauer, L. C., and Klaunberg, B. A. (2016). Comparing the effects of isoflurane and alpha chloralose upon mouse physiology. *PloS one*, *11*(5), e0154936.

Lyons, G. E., Schiaffino, S., Sassoon, D., Barton, P., and Buckingham, M. (1990). Developmental regulation of myosin gene expression in mouse cardiac muscle. *The Journal of cell biology*, *111*(6), 2427-2436.

Mages, C., Gampp, H., Syren, P., Rahm, A. K., André, F., Frey, N., ... and Thomas, D. (2021). Electrical Ventricular Remodeling in Dilated Cardiomyopathy. *Cells*, *10*(10), 2767.

Moss, R. L., Razumova, M., and Fitzsimons, D. P. (2004). Myosin crossbridge activation of cardiac thin filaments: implications for myocardial function in health and disease. *Circulation research*, *94*(10), 1290-1300.

Michela, P., Velia, V., Aldo, P., and Ada, P. (2015). Role of connexin 43 in cardiovascular diseases. *European journal of pharmacology*, *768*, 71-76.

Miller JB, Teal SB, Stockdale FE. Evolutionarily conserved sequences of striated muscle myosin heavy chain isoforms: epitope mapping by cDNA expression. J Biol Chem.1989; *264*:13122

Miyata, S., Minobe, W., Bristow, M. R., and Leinwand, L. A. (2000). Myosin heavy chain isoform expression in the failing and nonfailing human heart. *Circulation research*, *86*(4), 386-390.

Muslin (2012). The Pathophysiology of Heart Failure. *Muscle: Fundamental Biology and Mechanisms of Disease*. Chapter. (1), 523-535.

Molkentin, J. D., Lu, J. R., Antos, C. L., Markham, B., Richardson, J., Robbins, J., ... and Olson, E. N. (1998). A calcineurin-dependent transcriptional pathway for cardiac hypertrophy. *Cell*, *93*(2), 215-228.

Molkentin, J. D. (2004). Calcineurin–NFAT signaling regulates the cardiac hypertrophic response in coordination with the MAPKs. *Cardiovascular research*, *63*(3), 467-475.

Morningstar, J. E., Gensemer, C., Moore, R., Fulmer, D., Beck, T. C., Wang, C., ... and Norris, R. A. (2021). Mitral valve prolapse induces regionalized myocardial fibrosis. *Journal of the American Heart Association*, *10*(24), e022332.

Natividad, N. (2014). Role of SNARE Proteins in Natriuretic Peptide Secretion by the Heart.

Naudin, V., Oliviero, P., Rannou, F., Sainte Beuve, C., and Charlemagne, D. (1991). The density of ryanodine receptors decreases with pressure overload-induced rat cardiac hypertrophy. *FEBS letters*, *285*(1), 135-138.

Nauta, J. F., Hummel, Y. M., Tromp, J., Ouwerkerk, W., van der Meer, P., Jin, X., ... and Voors, A. A. (2020). Concentric vs. eccentric remodelling in heart failure with reduced ejection fraction: clinical characteristics, pathophysiology and response to treatment. *European journal of heart failure*, *22*(7), 1147-1155.

Nicol, R. L., Frey, N., Pearson, G., Cobb, M., Richardson, J., and Olson, E. N. (2001). Activated MEK5 induces serial assembly of sarcomeres and eccentric cardiac hypertrophy. *The EMBO journal*, *20*(11), 2757-2767.

Ohler, A., Weisser-Thomas, J., Piacentino, V., Houser, S. R., Tomaselli, G. F., and O'Rourke, B. (2009). Two-photon laser scanning microscopy of the transverse-axial tubule system in ventricular cardiomyocytes from failing and non-failing human hearts. *Cardiology research and practice*, *2009*.

O'Shea, C., Kabir, S. N., Holmes, A. P., Lei, M., Fabritz, L., Rajpoot, K., and Pavlovic, D. (2020). Cardiac optical mapping–State-of-the-art and future challenges. *The international journal of biochemistry & cell biology*, *126*, 105804.

Pardo, L., Valor, L. M., Eraso-Pichot, A., Barco, A., Golbano, A., Hardingham, G. E., ... & Galea, E. (2017). CREB regulates distinct adaptive transcriptional programs in astrocytes and neurons. *Scientific reports*, *7*(1), 6390.

Park, D. S., and Fishman, G. I. (2011). The cardiac conduction system. *Circulation*, *123*(8), 904-915.

Parks, R. J., and Howlett, S. E. (2013). Sex differences in mechanisms of cardiac excitation–contraction coupling. *Pflügers Archiv-European Journal of Physiology*, *465*, 747-763.

Peng, Y., Popovic, Z. B., Sopko, N., Drinko, J., Zhang, Z., Thomas, J. D., and Penn, M. S. (2009). Speckle tracking echocardiography in the assessment of mouse models of cardiac dysfunction. *American Journal of Physiology-Heart and Circulatory Physiology*, *297*(2), H811-H820.

Pérez-Riera, A. R., de Abreu, L. C., Barbosa-Barros, R., Nikus, K. C., and Baranchuk, A. (2016). R-peak time: An electrocardiographic parameter with multiple clinical applications. *Annals of Noninvasive Electrocardiology*, *21*(1), 10-19.

Periasamy, M., and Kalyanasundaram, A. (2007). SERCA pump isoforms: their role in calcium transport and disease. *Muscle & Nerve: Official Journal of the American Association of Electrodiagnostic Medicine*, *35*(4), 430-442.

Perl, E., Ravisankar, P., Beerens, M. E., Mulahasanovic, L., Smallwood, K., Sasso, M. B., ... and Waxman, J. S. (2022). Stx4 is required to regulate cardiomyocyte Ca2+ handling during vertebrate cardiac development. *Human Genetics and Genomics Advances*, *3*(3), 100115.

Peters, C. G., Miller, D. F., and Giovannucci, D. R. (2006). Identification, localization and interaction of SNARE proteins in atrial cardiac myocytes. *Journal of molecular and cellular cardiology*, *40*(3), 361-374.

Piacentino III, V., Weber, C. R., Chen, X., Weisser-Thomas, J., Margulies, K. B., Bers, D. M., and Houser, S. R. (2003). Cellular basis of abnormal calcium transients of failing human ventricular myocytes. *Circulation research*, *92*(6), 651-658.

Pieske, B., Kretschmann, B., Meyer, M., Holubarsch, C., Weirich, J., Posival, H., ... and Hasenfuss, G. (1995). Alterations in intracellular calcium handling associated with the inverse force-frequency relation in human dilated cardiomyopathy. *Circulation*, *92*(5), 1169-1178.

Pinz, I., Tian, R., Belke, D., Swanson, E., Dillmann, W., and Ingwall, J. S. (2011). Compromised myocardial energetics in hypertrophied mouse hearts diminish the beneficial effect of overexpressing SERCA2a. *Journal of Biological Chemistry*, *286*(12), 10163-10168.

Popoli, M. p65-Synaptotagmin: a docking-fusion protein in synaptic vesicle exocytosis? 8 (1993).

Poulet, C., Sanchez-Alonso, J., Swiatlowska, P., Mouy, F., Lucarelli, C., Alvarez-Laviada, A., ... and Gorelik, J. (2021). Junctophilin-2 tethers T-tubules and recruits functional L-type calcium channels to lipid rafts in adult cardiomyocytes. *Cardiovascular research*, *117*(1), 149-161.

Pott, C., Eckardt, L., and I Goldhaber, J. (2011). Triple threat: the Na^+/Ca^{2+} exchanger in the pathophysiology of cardiac arrhythmia, ischemia and heart failure. *Current drug targets*, *12*(5), 737-747.

Ram, R., Mickelsen, D. M., Theodoropoulos, C., and Blaxall, B. C. (2011). New approaches in small animal echocardiography: imaging the sounds of silence. *American Journal of Physiology-Heart and Circulatory Physiology*, *301*(5), H1765-H1780.

Ramirez, F. D., Motazedian, P., Jung, R. G., Di Santo, P., MacDonald, Z., Simard, T., ... and Hibbert, B. (2017). Sex bias is increasingly prevalent in preclinical cardiovascular research: implications for translational medicine and health equity for women: a systematic assessment of leading cardiovascular journals over a 10-year period. *Circulation*, *135*(6), 625-626.

Rao, X., Huang, X., Zhou, Z., and Lin, X. (2013). An improvement of the 2ˆ (–delta delta CT) method for quantitative real-time polymerase chain reaction data analysis. *Biostatistics, bioinformatics and biomathematics*, *3*(3), 71.

Rea, D., Coppola, C., Barbieri, A., Monti, M. G., Misso, G., Palma, G., ... and Arra, C. (2016). Strain analysis in the assessment of a mouse model of cardiotoxicity due to chemotherapy: sample for preclinical research. *in vivo*, *30*(3), 279-290.

Rich, T. L., and Langer, G. A. (1975). A comparison of excitation-contraction coupling in heart and skeletal muscle: An examination of "calcium-induced calcium release". *Journal of Molecular and Cellular Cardiology*, *7*(10), 747-765.

Ringer, S. (1883). A further contribution regarding the influence of the different constituents of the blood on the contraction of the heart. *The Journal of physiology*, *4*(1), 29.

Roger, V. L., Go, A. S., Lloyd-Jones, D. M., Adams, R. J., Berry, J. D., Brown, T. M., and Wylie-Rosett, J. (2011). Heart disease and stroke statistics—2011 update: a report from the American Heart Association. *Circulation*, *123*(4), e18-e209.

Rivello, H. G., Meckert, P. C., Vigliano, C., Favaloro, R., and Laguens, R. P. (2001). Cardiac myocyte nuclear size and ploidy status decrease after mechanical support. *Cardiovascular Pathology*, *10*(2), 53-57.

Ruska, E. and Kroll, M. (1931). Z Tech. *Phys* 12, 389.

Russo, I., Micotti, E., Fumagalli, F., Magnoli, M., Ristagno, G., Latini, R., and Staszewsky, L. (2019). A novel echocardiographic method closely agrees with cardiac magnetic resonance in the assessment of left ventricular function in infarcted mice. *Scientific reports*, *9*(1), 1-10.

Sajman, J., Trus, M., Atlas, D., and Sherman, E. (2017). The L-type voltage-gated calcium channel co-localizes with syntaxin 1A in nano-clusters at the plasma membrane. *Scientific reports*, *7*(1), 1-11.

Salazar, N. C., Chen, J., and Rockman, H. A. (2007). Cardiac GPCRs: GPCR signaling in healthy and failing hearts. *Biochimica et Biophysica Acta (BBA)-Biomembranes*, *1768*(4), 1006-1018.

Samak, M., Fatullayev, J., Sabashnikov, A., Zeriouh, M., Schmack, B., Farag, M., ... and Weymann, A. (2016). Cardiac hypertrophy: an introduction to molecular and cellular basis. *Medical science monitor basic research*, *22*, 75.

Sandow, A. (1952). Excitation-contraction coupling in muscular response. *The Yale journal of biology and medicine*, *25*(3), 176.

Sano, T., Takayama, N., and Shimamoto, T. (1959). Directional difference of conduction velocity in the cardiac ventricular syncytium studied by microelectrodes. *Circulation Research*, *7*(2), 262-267.

Satin, J., Schroder, E. A., & Crump, S. M. (2011). L-type calcium channel auto-regulation of transcription. *Cell calcium*, *49*(5), 306-313.
, J., Schroder, E. A., and Crump, S. M. (2011). L-type calcium channel auto-regulation of transcription. *Cell calcium*, *49*(5), 306-313.

Schmidt, U., Hajjar, R. J., Kim, C. S., Lebeche, D., Doye, A. A., and Gwathmey, J. K. (1999). Human heart failure: cAMP stimulation of SR Ca2+-ATPase activity and phosphorylation level of phospholamban. *American Journal of Physiology-Heart and Circulatory Physiology*, *277*(2), H474-H480.

Schnelle, M., Catibog, N., Zhang, M., Nabeebaccus, A. A., Anderson, G., Richards, D. A., ... and Shah, A. M. (2018). Echocardiographic evaluation of diastolic function in mouse models of heart disease. *Journal of molecular and cellular cardiology*, *114*, 20-28.

Schwertz, D. W., Beck, J. M., Kowalski, J. M., and Ross, J. D. (2004). Sex differences in the response of rat heart ventricle to calcium. *Biological research for nursing*, *5*(4), 286-298.

Schwinger, R. H., Böhm, M., Schmidt, U., Karczewski, P., Bavendiek, U., Flesch, M., ... and Erdmann, E. (1995). Unchanged protein levels of SERCA II and phospholamban but reduced Ca2+ uptake and Ca2+-ATPase activity of cardiac sarcoplasmic reticulum from dilated cardiomyopathy patients compared with patients with nonfailing hearts. *Circulation*, *92*(11), 3220-3228.

Schulze, K. L., and Bellen, H. J. (1996). Drosophila syntaxin is required for cell viability and may function in membrane formation and stabilization. *Genetics*, *144*(4), 1713-1724.

Sciarretta, S., and Sadoshima, J. (2010). New insights into the molecular phenotype of eccentric hypertrophy. *Journal of molecular and cellular cardiology*, *49*(2), 153.

Sengupta, P. P., Khandheria, B. K., Korinek, J., Wang, J., Jahangir, A., Seward, J. B., and Belohlavek, M. (2006). Apex-to-base dispersion in regional timing of left ventricular shortening and lengthening. *Journal of the American College of Cardiology*, *47*(1), 163-172.

Shaw, R. M., and Colecraft, H. M. (2013). L-type calcium channel targeting and local signalling in cardiac myocytes. *Cardiovascular research*, *98*(2), 177-186.

Shimizu, I., and Minamino, T. (2016). Physiological and pathological cardiac hypertrophy. *Journal of molecular and cellular cardiology*, *97*, 245-262.

Shimizu, I., Minamino, T., Toko, H., Okada, S., Ikeda, H., Yasuda, N., ... and Komuro, I. (2010). Excessive cardiac insulin signaling exacerbates systolic dysfunction induced by pressure overload in rodents. *The Journal of clinical investigation*, *120*(5), 1506-1514.

Shiojima, I., Aikawa, M., Suzuki, J. I., Yazaki, Y., and Nagai, R. (1999). Embryonic smooth muscle myosin heavy chain SMemb is expressed in pressure-overloaded cardiac fibroblasts. *Japanese heart journal*, *40*(6), 803-818.

Sikkel, M. B., Hayward, C., MacLeod, K. T., Harding, S. E., and Lyon, A. R. (2014). SERCA2a gene therapy in heart failure: an anti-arrhythmic positive inotrope. *British journal of pharmacology*, *171*(1), 38-54.

Sleiman, Y., Lacampagne, A., and Meli, A. C. (2021). “Ryanopathies” and RyR2 dysfunctions: can we further decipher them using in vitro human disease models?. *Cell Death & Disease*, *12*(11), 1041.

Smith, F. G., Sato, T., Varille, V. A., and Robillard, J. E. (1989). Atrial natriuretic factor during fetal and postnatal life: a review. *Journal of developmental physiology*, *12*(2), 55-62.

Spinale, F. G., Crawford Jr, F. A., Hewett, K. W., and Carabello, B. A. (1991). Ventricular failure and cellular remodeling with chronic supraventricular tachycardia. *The Journal of Thoracic and Cardiovascular Surgery*, *102*(6), 874-882.

Statello, L., Guo, C. J., Chen, L. L., and Huarte, M. (2021). Gene regulation by long non-coding RNAs and its biological functions. *Nature reviews Molecular cell biology*, *22*(2), 96-118.

Su, X., Brower, G., Janicki, J. S., Chen, Y. F., Oparil, S., and Dell'Italia, L. J. (1999). Differential expression of natriuretic peptides and their receptors in volume overload cardiac hypertrophy in the rat. *Journal of molecular and cellular cardiology*, *31*(10), 1927-1936.

Taegtmeyer, H., Sen, S., and Vela, D. (2010). Return to the fetal gene program: a suggested metabolic link to gene expression in the heart. *Annals of the New York Academy of Sciences*, *1188*(1), 191-198.

Takizawa, T., Arai, M., Tomaru, K., Koitabashi, N., Baker, D. L., Periasamy, M., and Kurabayashi, M. (2003). Transcription factor Sp1 regulates SERCA2 gene expression in pressure-overloaded hearts: a study using in vivo direct gene transfer into living myocardium. *Journal of molecular and cellular cardiology*, *35*(7), 777-783.

Tarnow, P., Schöneberg, T., Krude, H., Grüters, A., and Biebermann, H. Mutationally induced disulfide bond formation within the third extracellular loop causes melanocortin 4 receptor inactivation in patients with obesity

Tayal, U., and Prasad, S. K. (2017). Myocardial remodelling and recovery in dilated cardiomyopathy. *JRSM Cardiovascular Disease*, *6*, 2048004017734476.

Teng, F. Y. H., Wang, Y., and Tang, B. L. (2001). The syntaxins. *Genome biology*, *2*(11), 1-7.

Toft-Bertelsen, T. L., Ziomkiewicz, I., Houy, S., Pinheiro, P. S., and Sørensen, J. B. Regulation of Ca^{2+} channels by SNAP-25 via recruitment of syntaxin-1 from plasma membrane clusters.

Toischer, K., Rokita, A. G., Unsöld, B., Zhu, W., Kararigas, G., Sossalla, S., ... and Hasenfuss, G. (2010). Differential cardiac remodeling in preload versus afterload. *Circulation*, *122*(10), 993-1003.

Tokudome, T., Horio, T., Kishimoto, I., Soeki, T., Mori, K., Kawano, Y., ... and Kangawa, K. (2005). Calcineurin–nuclear factor of activated T cells pathway–dependent cardiac remodeling in mice deficient in guanylyl cyclase a, a receptor for atrial and brain natriuretic peptides. *Circulation*, *111*(23), 3095-3104.

Toonen, R. F., and Verhage, M. (2003). Vesicle trafficking: pleasure and pain from SM genes. *Trends in cell biology*, *13*(4), 177-186.

Trimble, W. S., Cowan, D. M., and Scheller, R. H. (1988). VAMP-1: a synaptic vesicle-associated integral membrane protein. *Proceedings of the National Academy of Sciences*, *85*(12), 4538-4542.

Trus, M., Wiser, O., Goodnough, M. . and Atlas, D. The transmembrane domain of syntaxin 1A negatively regulates voltage-sensitive Ca^{2+} channels. *Neuroscience* 104, 599–607 (2001).

Tsai, Y. C., and Weissman, A. M. (2010). The unfolded protein response, degradation from the endoplasmic reticulum, and cancer. *Genes & cancer*, *1*(7), 764-778.

Tsao, C. W., Aday, A. W., Almarzooq, Z. I., Alonso, A., Beaton, A. Z., Bittencourt, M. S., ... and American Heart Association Council on Epidemiology and Prevention Statistics Committee and Stroke Statistics Subcommittee. (2022). Heart disease and stroke statistics—2022 update: a report from the American Heart Association. *Circulation*, *145*(8), e153-e639.

Vardar, G., Chang, S., Arancillo, M., Wu, Y. J., Trimbuch, T., and Rosenmund, C. (2016). Distinct functions of syntaxin-1 in neuronal maintenance, synaptic vesicle docking, and fusion in mouse neurons. *Journal of Neuroscience*, *36*(30), 7911-7924.

Vatner, D. E., Sato, N., Kiuchi, K., Shannon, R. P., and Vatner, S. F. (1994). Decrease in myocardial ryanodine receptors and altered excitation-contraction coupling early in the development of heart failure. *Circulation*, *90*(3), 1423-1430.

Vinhas, M., Araújo, A. C., Ribeiro, S., Rosário, L. B., and Belo, J. A. (2013). Transthoracic echocardiography reference values in juvenile and adult 129/Sv mice. *Cardiovascular ultrasound*, *11*(1), 1-10.

Virdi, A. S. (2022). Assessing the Role of Syntaxin 1A in Excitation-Contraction Coupling in the Adult Mouse Heart. York University.

Virdi, M. S. (2019). Characterizing the Role of Syntaxin 1A in the Heart. York University.

Walsh-Wilkinson, E., Arsenault, M., and Couet, J. (2021). Segmental analysis by speckle-tracking echocardiography of the left ventricle response to isoproterenol in male and female mice. *PeerJ*, *9*, e11085.

Weeks, K. L., and McMullen, J. R. (2011). The athlete's heart vs. the failing heart: can signaling explain the two distinct outcomes?. *Physiology*, *26*(2), 97-105.

Weidman, P. J., Melançon, P., Block, M. R., and Rothman, J. E. (1989). Binding of an N-ethylmaleimide-sensitive fusion protein to Golgi membranes requires both a soluble protein (s) and an integral membrane receptor. *The Journal of cell biology*, *108*(5), 1589-1596.

Weiss, N., Hameed, S., Fernández-Fernández, J. M., Fablet, K., Karmazinova, M., Poillot, C., ... and De Waard, M. (2012). A Cav3. 2/syntaxin-1A signaling complex controls T-type channel activity and low-threshold exocytosis. *Journal of Biological Chemistry*, *287*(4), 2810-2818.

Wilkins, B. J., Dai, Y. S., Bueno, O. F., Parsons, S. A., Xu, J., Plank, D. M., ... and Molkentin, J. D. (2004). Calcineurin/NFAT coupling participates in pathological, but not physiological, cardiac hypertrophy. *Circulation research*, *94*(1), 110-118.

Wiser, O., Bennett, M. K. and Atlas, D. Functional interaction of syntaxin and SNAP-25 with voltage-sensitive L-and N-type Ca^{2+} channels. *The EMBO J.* 15, (1996)

Woods, R. L. (2004). Cardioprotective functions of atrial natriuretic peptide and B-type natriuretic peptide: a brief review. *Clinical and Experimental Pharmacology and Physiology*, *31*(11), 791-794.

Workman, A. J., Marshall, G. E., Rankin, A. C., Smith, G. L., and Dempster, J. (2012). Transient outward K+ current reduction prolongs action potentials and promotes afterdepolarisations: a dynamic-clamp study in human and rabbit cardiac atrial myocytes. *The Journal of physiology*, *590*(17), 4289-4305.

Wu, J., Bu, L., Gong, H., Jiang, G., Li, L., Ma, H., ... and Zou, Y. (2010). Effects of heart rate and anesthetic timing on high-resolution echocardiographic assessment under isoflurane anesthesia in mice. *Journal of Ultrasound in Medicine*, *29*(12), 1771-1778.

Wu, J., You, J., Wang, X., Wang, S., Huang, J., Xie, Q., ... and Zou, Y. (2020). Left ventricular response in the transition from hypertrophy to failure recapitulates distinct roles of Akt, β-arrestin-2, and CaMKII in mice with aortic regurgitation. *Annals of translational medicine*, *8*(5).

Yamakawa, T., Saith, S., Li, Y., Gao, X., Gaisano, H. Y., and Tsushima, R. G. (2007). Interaction of syntaxin 1A with the N-terminus of Kv4. 2 modulates channel surface expression and gating. *Biochemistry*, *46*(38), 10942-10949.

Ytrehus, K., Hulot, J. S., Perrino, C., Schiattarella, G. G., and Madonna, R. (2018). Perivascular fibrosis and the microvasculature of the heart. Still hidden secrets of pathophysiology?. *Vascular Pharmacology*, *107*, 78-83.

Zhang, D. Y., and Anderson, A. S. (2014). The sympathetic nervous system and heart failure. *Cardiology clinics*, *32*(1), 33-45.

Zhou, P., and Pu, W. T. (2016). Recounting cardiac cellular composition. *Circulation research*, *118*(3), 368-370.

Zima, A. V., Bovo, E., Mazurek, S. R., Rochira, J. A., Li, W., and Terentyev, D. (2014). Ca handling during excitation–contraction coupling in heart failure. *Pflügers Archiv-European Journal of Physiology*, *466*(6), 1129-1137.

SUPPLEMENTARY FIGURES

(A)

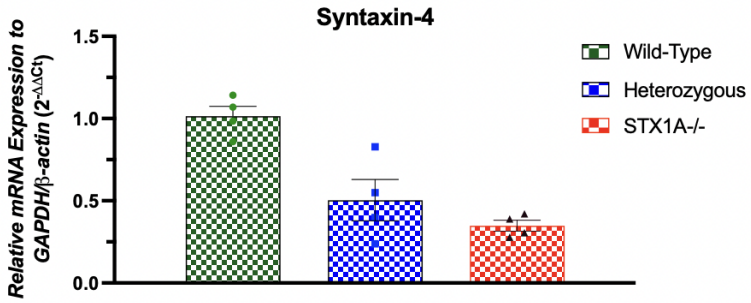

(B)

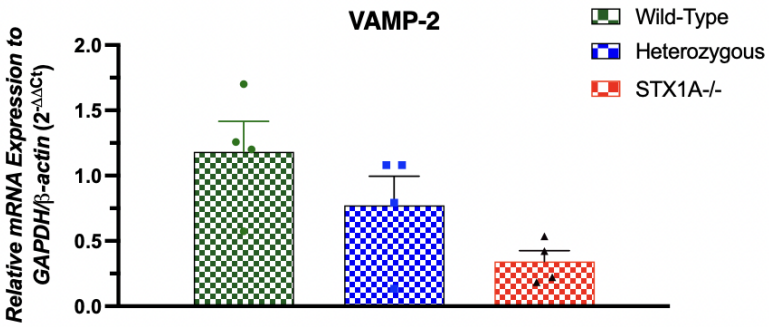

(C)

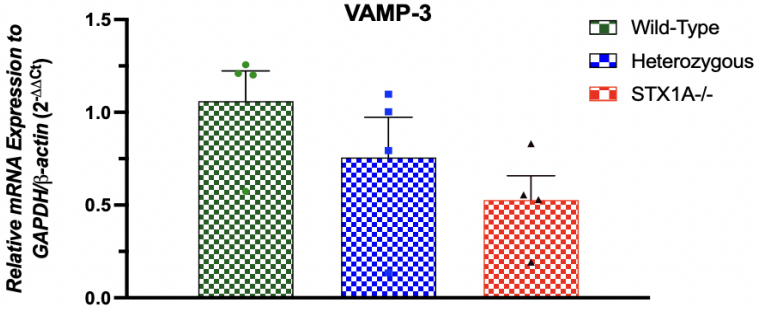

Supplementary Figure 1: RT-qPCR on STX1A KO mice for STX4, VAMP-2, and VAMP-3 at week 0. Post-tamoxifen treatment, **(A)** STX4, **(B)** VAMP-2, and **(C)** VAMP-3 transcript levels are downregulated in heterozygous (Heterozygous) and homozygous KO mice (STX1A-/-) while expression is retained within Cre^{+} mice (Wild-Type). *Graphs were received with permission from Faizan (2022).*

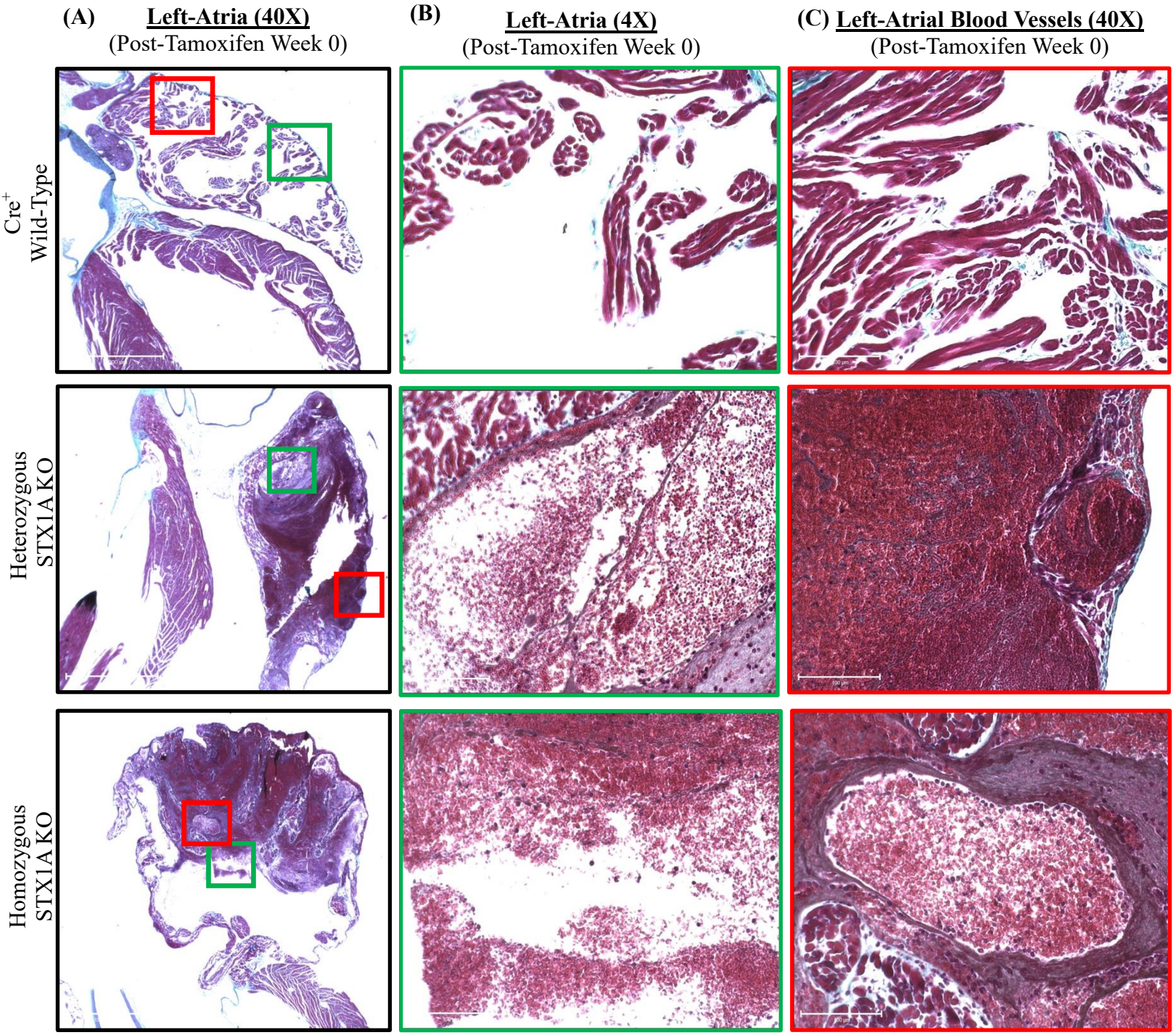

Supplementary Figure 2: Development of oedema within the left-atria post-STX1A KO. **(A, B)** Presence of red blood cells within the left-atria is suggestive of mitral valve-regurgitation in heterozygous and homozygous STX1A KO mice. **(C)** Blood vessels filled with red-blood cells in STX1A KO mice can be further suggestive of oedema formation within pulmonary circulation (n = 1).